РОССИЙСКИЙ ГОСУДАРСТВЕННЫЙ ПЕДАГОГИЧЕСКИЙ УНИВЕРСИТЕТ им. А. И. ГЕРЦЕНА
HERZEN STATE PEDAGOGICAL UNIVERSITY of RUSSIA

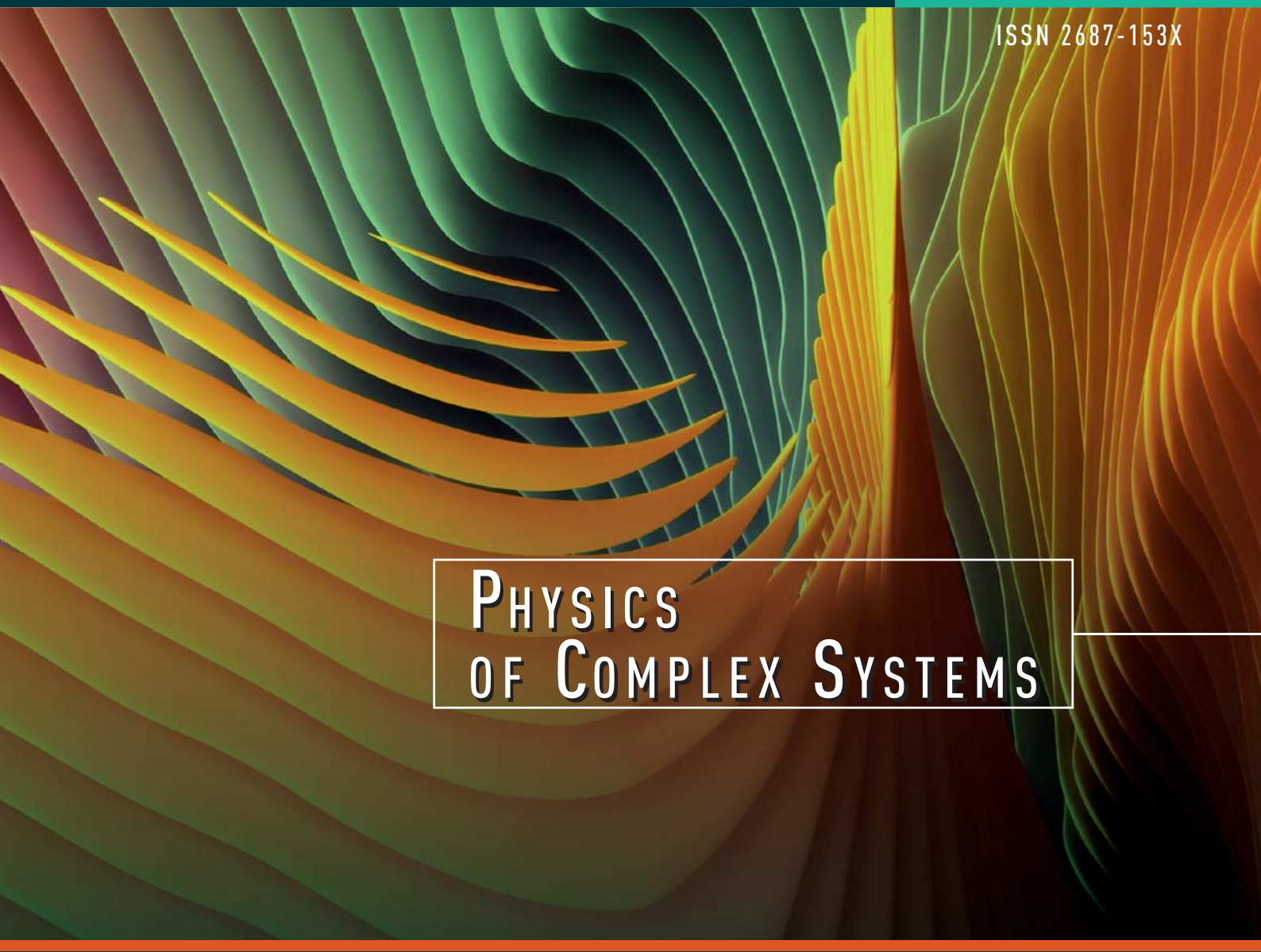

ISSN 2687-153X

Physics of Complex Systems

Т. 4 № 4 2023

Vol. 4 No. 4 2023

Herzen State Pedagogical University of Russia

ISSN 2687-153X (online)
physcomsys.ru
https://www.doi.org/10.33910/2687-153X-2023-4-4
2023. Vol. 4, no. 4

PHYSICS OF COMPLEX SYSTEMS

Mass Media Registration Certificate El No. FS77-77889, issued by Roskomnadzor on 10 February 2020
Peer-reviewed journal
Open Access
Published since 2020
4 issues per year

Publishing house of Herzen State Pedagogical University of Russia
48 Moika Emb., Saint Petersburg 191186, Russia
E-mail: izdat@herzen.spb.ru
Phone: +7 (812) 312-17-41

Data size 6,72 Mbyte
Published at 08.12.2023

Editors of the English text *M. V. Bumakova, I. A. Nagovitsyna*
Corrector *E. V. Novoseltseva*
Cover design by *O. V. Rudneva*
Layout by *A. M. Khodan, L. N. Kliuchanskaya*

CONTENTS

Condensed Matter Physics.
Theory of condensed matter

UDC 539.3

EDN HRTBPL
https://www.doi.org/10.33910/2687-153X-2023-4-4-149-156

A comparison of interatomic interaction potentials in modeling elastic properties of pseudo-graphene crystals

M. A. Rozhkov✉[1], N. D. Abramenko[1], A. M. Smirnov[1], A. L. Kolesnikova[2], A. E. Romanov[1]

[1] ITMO University, 49 Kronverksky Ave., Saint Petersburg 197101, Russia
[2] Institute for Problems in Mechanical Engineering of the Russian Academy of Sciences, 61 Bolshoi Ave., V. O., Saint Petersburg 199178, Russia

Authors
Mikhail A. Rozhkov, ORCID: 0000-0001-7350-0717, e-mail: MARozhkov@itmo.ru
Nikita D. Abramenko, ORCID: 0009-0003-8538-5113, e-mail: NDAbramenko@itmo.ru
Andrei M. Smirnov, ORCID: 0000-0002-7962-6481, e-mail: andrei.smirnov@niuitmo.ru
Anna L. Kolesnikova, ORCID: 0000-0003-4116-4821, e-mail: anna.kolesnikova.physics@gmail.com
Alexey E. Romanov, ORCID: 0000-0003-3738-408X, e-mail: alexey.romanov@niuitmo.ru

For citation: Rozhkov, M. A., Abramenko, N. D., Smirnov, A. M., Kolesnikova, A. L., Romanov, A. E. (2023) A comparison of interatomic interaction potentials in modeling elastic properties of pseudo-graphene crystals. *Physics of Complex Systems*, 4 (4), 149–156. https://www.doi.org/10.33910/2687-153X-2023-4-4-149-156 EDN HRTBPL

Received 13 June 2023; reviewed 29 August 2023; accepted 29 August 2023.

Funding: The work was supported by the Russian Science Foundation (grant No 19-19-00617).

Abstract. In this work, we simulate mechanical properties of pseudo-graphene crystals G5-7v1, G5-6-7v2, G4-8v1, G5-6-8v2, G5-6-8v4, G5-8v1, which include dense networks of wedge disclinations of alternate signs. The crystals were studied using the molecular dynamics method. The paper compares the values of elastic properties of graphene and pseudo-graphene obtained through AIREBO, Tersoff, and LCBOP interatomic interaction potentials. It shows that the application of these potentials in modeling pseudo-graphene crystals is limited. The study concludes that it is necessary to update the existing potentials of interatomic interaction in allotropes of carbon or create a new one.

Keywords: molecular dynamics, pseudo-graphene, elastic properties, disclination, defect structure

Introduction

Graphene is a two-dimensional carbon crystal with a variety of promising properties: high conductivity (Novoselov et al. 2005), thermal conductivity (Chen et al. 2010), and a unique set of mechanical properties (Lee et al. 2008). Its successful synthesis (Novoselov et al. 2004) attracted great attention and marked an active growth of interest in the study of two-dimensional crystals.

In graphene, just as in three-dimensional crystals, one can observe crystal lattice defects (Hao et al. 2011; Wei et al. 2012). Among them are two-dimensional (pores and inclusions), one-dimensional (interfaces without misorientation and grain boundaries), and point-like (vacancies, interstitial atoms and impurity atoms, dislocations and disclinations) defects (Romanov et al. 2015; 2018). It is important to study the effects of such defects to predict the properties of graphene samples and to control their characteristics. For example, an interface in graphene can increase its thermal (Jafri et al. 2010) or electrical conductivity (Bagri et al. 2011).

A wide range of research works focuses on two-dimensional carbon crystals, different from graphene (Baughman et al. 1987; Enyashin, Ivanovskii 2011; Gong et al. 2020; Terrones et al. 2000).

They have a high density of carbon atomic rings with defects organized periodically. These crystals are commonly referred to as 'graphene allotropes' (Wang et al. 2015; Zhuo et al. 2020), 'carbon allotropes' (Deb et al. 2020; Zhang et al. 2015), 'pseudo-graphenes' (Abramenko et al. 2020), etc. The majority of these materials are yet to be synthesized (with the exception of biphenylene (Fan et al. 2021) — the only synthesized pseudo-graphene crystal (PGC) so far). However, it is important to predict the properties of such materials to improve the modelling methods and algorithms to a further degree of precision. We hope that in the near future predicted property values of a non-synthesized material will be as close to the actual ones as possible. In addition, the predictions can be used as a roadmap for researchers who aim to synthesize such crystals as, thanks to the prediction algorithms, lots of material suggestions have proven to be unstable (Xie et al. 2020), and, thus, crystals were impossible to synthesize.

The properties of carbon-based materials can be studied theoretically using various methods: atomistic modeling, density functional theory, analytical calculation, etc. One of the most popular calculation methods is molecular dynamics. It is a fast prediction method that allows calculating simple and complex properties on a high-scale crystal lattice. The molecular dynamics method uses a special approximation function — interatomic potential. It displays the dependency of potential energy between each pair of atoms on the distance between the atoms. The function serves as a physical basis of molecular dynamics and each material requires a new function. Given that this function is an approximation, the approaches to its description vary. For example, for calculations on graphene we could use Tersoff, AIREBO, LCBOP (Los, Fasolino 2003; Stuart et al. 2000; Tersoff 1988) and other styles of interatomic potentials.

In this article, we provide a comparison between the three mentioned above interatomic potentials used in molecular dynamics calculations to study the mechanical properties of several PGCs. Our goal is to find out whether the interatomic potentials designed for graphene are applicable to PGCs. We start with the description of the modeling technique and materials models in Section 2. In Section 3, we analyze the mechanical properties of several PGCs using molecular dynamics. In Section 4, we discuss the obtained results and compare the potentials.

Modeling technique and materials

The method of molecular dynamics is effective for in-depth investigation of elastic deformation in graphene crystals and pseudo-graphenes. We used the LAMMPS software package to obtain the elastic properties of the studied crystals and made a comparison between the three potentials of interatomic interaction: AIREBO, Tersoff, and LCBOP. AIREBO and LCBOP potentials were developed for the simulation of carbon systems and successfully tested for the simulation of graphene (Baimova et al. 2014; Hansen-Dörr et al. 2019). The Tersoff potential used in this work was developed for modeling silicon carbide. It also showed good results when modeling two-dimensional allotropes of carbon (Shirazi et al. 2019; Winczewski et al. 2018). In our work, the simulation was performed at room temperature and with periodic boundary conditions applied to the boundaries of the system. Energy minimization was carried out using the Polak-Ribière conjugate gradient algorithm (Polak, Ribiere 1969). To obtain the elastic constants in the simulation, a deformation of 0.5% was applied. We visualized the obtained numerical results with the OVITO software package.

To interpret the obtained data, it is necessary to convert the tensor of elastic constants into elastic moduli, such as Young's modulus and Poisson's ratio. Hooke's law for a two-dimensional anisotropic body has the following format:

$$\begin{bmatrix} \sigma_{xx} \\ \sigma_{yy} \\ \sigma_{xy} \end{bmatrix} = \begin{bmatrix} C_{11} & C_{12} & 0 \\ C_{12} & C_{22} & 0 \\ 0 & 0 & C_{66} \end{bmatrix} \begin{bmatrix} \varepsilon_{xx} \\ \varepsilon_{yy} \\ 2\varepsilon_{xy} \end{bmatrix}, \quad (1)$$

where σ_{ij} and ε_{ij} are components of stress and strain, correspondingly; C_{ij} are components of the matrix of elastic constants.

For the matrix of elastic constants, components C_{12} and C_{21} obey the condition $C_{12} = C_{21}$, while components C_{16}, C_{26}, C_{61}, and C_{62} are equal to zero due to the symmetry properties of a two-dimensioal crystal. The labeling of elastic constants corresponds to the labeling of three-dimensional bodies, i. e., index '1' corresponds to the x-direction, '2' to the y-direction, and '6' to the xy-component. Thus, there are 4 independent components — C_{11}, C_{22}, C_{12}, and C_{66}. The conventional elastic moduli of the material are calculated by the following formulas:

 https://www.doi.org/10.33910/2687-153X-2023-4-4-149-156

$$\nu_{12} = \frac{C_{12}}{C_{22}}\ ; \nu_{21} = \frac{C_{12}}{C_{11}}\ ; E_1 = \frac{C_{11}C_{22} - C_{12}^2}{C_{22}}\ ; E_2 = \frac{C_{11}C_{22} - C_{12}^2}{C_{11}}\ ; G = C_{66}\ , \tag{2}$$

where E_i is Young's modulus corresponding to the i-direction; ν_{ij} is Poisson's ratio for the longitudinal direction i and the transverse direction j, G is a shear modulus.

For the case of a two-dimensional isotropic crystal, the following conditions are satisfied: $C_{11} = C_{22}$, $C_{12} = C_{21}$, $C_{66} = (C_{11} - C_{12})/2$. Thus, there are only two independent components: C_{11} and C_{12}. The elastic properties of the material are calculated by the following formulas:

$$\nu = \frac{C_{12}}{C_{11}}\ ; E = \frac{C_{11}^2 - C_{12}^2}{C_{11}}\ ; G = \frac{E\left(1+\nu\right)}{2}\ . \tag{3}$$

The obtained results for the mechanical properties of graphene and pseudo-graphene crystals are expressed in GPa, similarly to three-dimensional materials. The transition from N/m to Pa is made taking into account the 'thickness' of the two-dimensional crystal, which was taken to be 3.4 Å (Maitra et al. 2012).

In this work, we consider a graphene crystal and a number of low-energy pseudo-graphenes: G5-7v1, G5-6-7v2, G4-8v1, G5-6-8v2, G5-6-8v4, G5-8v1. The nomenclature of these crystals corresponds to the carbon rings that make up this crystal. It is known that graphene consists of hexagonal six-member atomic rings. In the presence of defects in graphene, rings with symmetry different from six-member are formed. Thus, pseudo-graphene G5-7v1 consists of only five- and seven-membered atomic rings. See the review (Abramenko et al. 2020) for more detailed information on the nomenclature. Pseudo-graphenes are the lowest energy 'allotropes' of graphene (Romanov et al. 2018). The crystals under study are shown in Fig. 1. When modeling these two-dimensional crystals, an approximation was used in which the crystal has a flat shape, i. e., they do not bend.

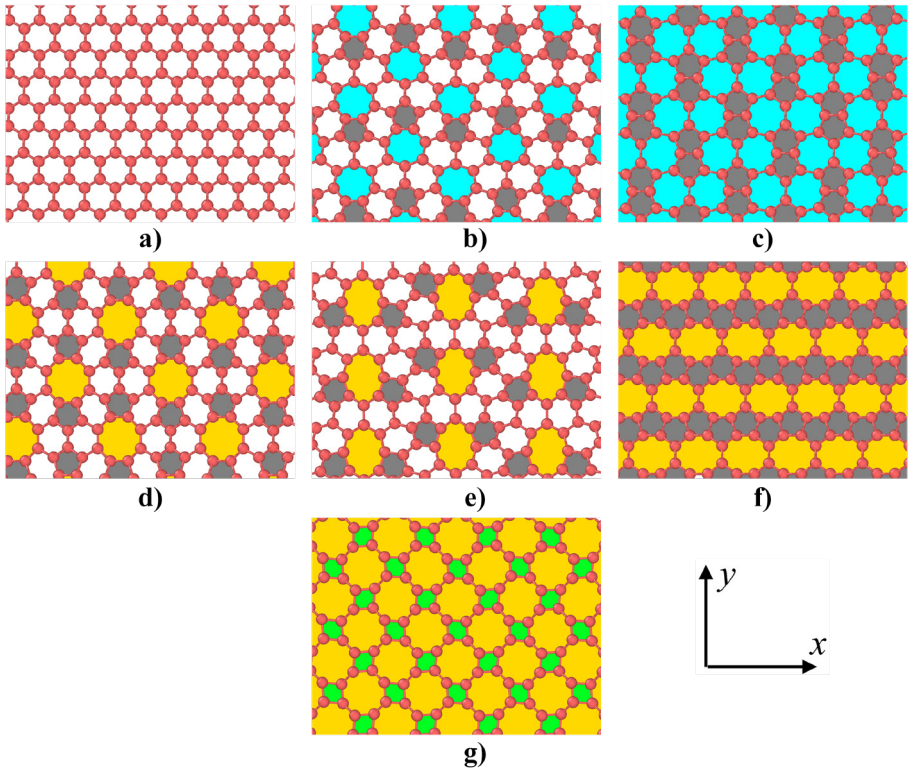

Fig. 1. Structure and primitive lattice of graphene (a) and pseudo-graphenes G5-7v1 (b), G5-6-7v2 (c), G5-6-8v2 (d), G5-6-8v4 (e), G5-8v1 (f) and G4-8v1 (g). The colors indicate defective carbon atomic rings: 7-unit rings — blue, 5-unit rings— gray, 8-unit rings—yellow, 4-unit rings—green

Results of molecular dynamics calculations

Tables 1–3 present a comparison of elastic properties of the studied PGCs and graphene, calculated using the AIREBO, Tersoff, and LCBOP potentials.

Table 1. Elastic constants for graphene and pseudo-graphene crystals calculated via molecular dynamics using AIREBO interatomic potential

	Graphene	**G5-6-7v2**	**G5-7v1**	**G4-8v1**	**G5-6-8v2**	**G5-6-8v4**	**G5-8v1**
C_{11}, GPa	952.4	**1016.03**	**1016.5**	598.2	**1040.3**	923.31	**1195.98**
C_{22}, GPa	952	**950.85**	**1010.7**	596.3	**970.89**	864.64	928.13
C_{12}, GPa	336	180.8	129.2	445	116.61	201.29	**45.78**
C_{66}, GPa	297.5	456.45	391.4	453.5	328.68	414.68	211.34
E_1, GPa	833.81	**981.65**	**999.98**	**266.11**	**1026.29**	876.45	**1193.72**
E_2, GPa	833.46	**918.68**	**994.28**	**265.27**	**957.82**	820.76	926.38
ν_{12}	0.353	0.190	0.128	**0.746**	0.120	0.233	**0.049**
ν_{21}	0.353	0.178	0.127	**0.744**	0.112	0.218	**0.038**
G, GPa	297.5	456.45	391.4	453.5	328.68	414.68	211.34

Table 2. Elastic constants for graphene and pseudo-graphene crystals calculated via molecular dynamics using Tersoff interatomic potential

	Graphene	**G5-6-7v2**	**G5-7v1**	**G4-8v1**	**G5-6-8v2**	**G5-6-8v4**	**G5-8v1**
C_{11}, GPa	1050.2	881.2	762.9	734.7	815.29	798.27	726.65
C_{22}, GPa	1050.2	914.1	808.5	734.7	798.81	827.28	724.97
C_{12}, GPa	**68.7**	133.4	221.1	146.69	179.95	163.63	247.16
C_{66}, GPa	490.8	393.6	376.5	**14.92**	327.87	306.53	229.43
E_1, GPa	1045.71	861.73	702.44	705.41	774.75	765.91	642.39
E_2, GPa	1045.71	893.91	744.42	705.41	759.09	793.74	640.91
ν_{12}	**0.065**	0.146	0.273	0.200	0.225	0.198	0.341
ν_{21}	**0.065**	0.151	0.290	0.200	0.221	0.205	0.340
G, GPa	490.8	393.6	376.5	**14.92**	327.87	306.53	229.43

Table 3. Elastic constants for graphene and pseudo-graphene crystals calculated via molecular dynamics using LCBOP interatomic potential

	Graphene	**G5-6-7v2**	**G5-7v1**	**G4-8v1**	**G5-6-8v2**	**G5-6-8v4**	**G5-8v1**
C_{11}, GPa	976.2	958.8	835.2	513.99	933.86	883.71	**1017.86**
C_{22}, GPa	976.3	900.4	854.2	514.69	870.97	827.76	765.06
C_{12}, GPa	216.4	154.9	230.2	367.14	134.63	168.54	159.63
C_{66}, GPa	379.9	378.2	333.7	571.24	297.31	357.51	212.48
E_1, GPa	928.23	**932.15**	773.16	**252.10**	913.05	849.39	**984.55**
E_2, GPa	928.33	875.38	790.75	**252.44**	851.56	795.62	740.03
ν_{12}	0.222	0.172	0.269	**0.713**	0.155	0.204	0.209
ν_{21}	0.222	0.162	0.276	**0.714**	0.144	0.191	0.157
G, GPa	379.9	378.2	333.7	571.24	297.31	357.51	212.48

https://www.doi.org/10.33910/2687-153X-2023-4-4-149-156

Discussion

As can be seen from the results presented in Table 1, the AIREBO potential shows the values for graphene that are comparable with the experimental (Lee et al. 2008) and simulation data obtained using density functional theory (Wei et al. 2009). This potential is quite often used in various studies of graphene and has proven to be effective (Akhunova et al. 2022; Kochnev et al. 2014). However, if graphene is taken as an ideal crystal, then pseudo-graphenes will be graphene crystals with a dense distribution of disclination defects. Thus, it can be assumed that the mechanical performance may be degraded. This is supported by DFT calculations (Fthenakis et al. 2015; Pereira et al. 2016; Sun et al. 2016): the elastic properties of graphene and pseudo-graphenes were compared, and a decrease in the value of Young's modulus for pseudo-graphenes compared to defect-free graphene was observed. This can be considered as one of the criteria to support the fact that the potential of interatomic interaction gives incorrect data for the selected material. One can observe this pattern for almost all pseudo-graphene crystals, excluding only PGC G5-8v1 and G4-8v1. However, for the G4-8v1 crystal, not only underestimated values of Young's modulus were found, but also the formally calculated values of Poisson's ratio greater than 0.5 were observed, which has no physical meaning. This indicates the low suitability of the AIREBO potential for studying the mechanical properties of pseudo-graphenes, despite the fact that it can be used to model the structure of the undeformed crystals (Kolesnikova et al. 2020; Romanov et al. 2018; Rozhkov et al. 2018).

The Tersoff potential is poorly suited for describing the elastic properties of graphene (Lebedeva et al. 2019), but it is often used to study various two-dimensional carbon allotropes (Shirazi et al. 2019; Winczewski et al. 2018). We can observe the same picture in our research (see Table 2), where almost all the results for pseudo-graphenes have acceptable values, with the exception of G4-8v1 PGC. In G4-8v1, an anomalously small value for C_{66} constant is observed. This indicates that the potential is unsuitable for studying this material. It may be necessary to carry out additional refinements in the parameters of the potential, which would make it possible to produce a correct description of the behavior of atoms in the crystal lattice of PGC G4-8v1.

For the results obtained using the LCBOP potential, we can see that it is well suited for studying graphene and for studying parts of pseudo-graphenes. For G5-6-7v2 and G5-8v1, we can see slightly overestimated values when compared with the values for defect-free graphene.

We can take DFT calculations for graphene from (Pereira et al. 2016) as a baseline, where Young's modulus E = 960 GPa. Young's modulus, calculated with Tersoff, is equal to E_1 = 1046 GPa. This value, calculated with AIREBO, is equal to 833 GPa, and with LCBOP to 928 GPa. Comparing to DFT, the deviation for all potentials is more than 10%. This relates not only to Young's modulus, but to other elastic constants as well.

For PGC G4-8v1, all three potentials display unsatisfactory results for elastic constants. The AIREBO and LCBOP potentials result in Poisson's ratio of about 0.7 (this is again unphysical) and Young's modulus of less than 300 GPa. In addition, for all considered potentials, one can notice a very wide scatter when comparing the values of Poisson's ratio with each other, both for PGCs and graphene. This can be justified by the fact that one cannot make a direct comparison between pseudo-graphene and graphene, since they have a completely different crystal structure with a different order of symmetry. The difference in symmetry is true for most PGCs.

The results obtained for elastic constants show that all the crystals studied in this article meet the Born stability criterion (Haastrup et al. 2018). The stability of the studied crystals is also supported by our DFT calculations (Abramenko, Rozhkov 2021) and prior research (Pereira et al. 2016; Sun et al. 2016).

The MD calculations of elastic constants that we have performed on graphene display a wide deviation in comparison not only to DFT, but also to the calculations themselves — elastic constants evaluated with the use of one interatomic potential differ a lot to ones calculated with the use of another interatomic potential.

Current works focusing on modeling elastic properties for defect-free graphene still exhibit strong differences in the reported values. See (Lebedeva et al. 2019) for an in-depth analysis of the scatter in Young's modulus and Poisson's ratio obtained using different potentials. Thus, Young's modulus is reported to be from 800 to 1200 GPa, while Poisson's ratio for graphene can vary from 0.15 to 0.22.

Conclusions

Calculated elastic constant values for pseudo-graphene crystal (PGC) with the use of molecular dynamics differ significantly in comparison with the values calculated with density functional theory (DFT). Even for graphene with the results much closer to DFT calculations, molecular dynamics values vary in an overly wide spectrum.

As of now, it is difficult to make a precise enough prediction of properties of pseudo-graphene crystals as no similarities on predicted values have been found between several interatomic potentials used in calculations. Thus, we cannot use interatomic potentials designed for graphene to calculate the properties of pseudo-graphene.

Among the studied potentials, the LCBOP and Tersoff potentials can be used with limitations to study certain PGCs. However, their results for G4-8v1 PGC and other pseudo-graphene crystals indicate the need to upgrade the obtained potentials or to develop a new interatomic interaction potential adapted for the study of two-dimensional allotropes of carbon.

Conflict of Interest

The authors declare that there is no conflict of interest, either existing or potential.

Author Contributions

All the authors discussed the final work and took part in writing the article.

References

Abramenko, N. D., Rozhkov, M. A. (2021) Lattice design for non-carbon two-dimensional allotropic modifications. *Reviews on Advanced Materials and Technologies*, 3 (4), 19–23. https://doi.org/10.17586/2687-0568-2021-3-4-19-23 (In English)

Abramenko, N. D., Rozhkov, M. A., Kolesnikova, A. L., Romanov, A. E. (2020) Structure and properties of pseudo-graphenes. Review. *Reviews on Advanced Materials and Technologies*, 2 (4), 9–26. https://doi.org/10.17586/2687-0568-2020-2-4-9-26 (In English)

Akhunova, A. K., Galiakhmetova, L. K., Baimova, J. A. (2022) The effects of dislocation dipoles on the failure strength of wrinkled graphene from atomistic simulation. *Applied Sciences*, 13 (1), article 9. https://doi.org/10.3390/app13010009 (In English)

Bagri, A., Kim, S.-P., Ruoff, R. S., Shenoy, V. B. (2011) Thermal transport across twin grain boundaries in polycrystalline graphene from nonequilibrium molecular dynamics simulations. *Nano Letters*, 11 (9), 3917–3921. https://doi.org/10.1021/nl202118d (In English)

Baimova, J. A., Liu, B., Zhou, K. (2014). Folding and crumpling of graphene under biaxial compression. *Letters on Materials*, 4 (2), 96–99. https://doi.org/10.22226/2410-3535-2014-2-96-99 (In English)

Baughman, R. H., Eckhardt, H., Kertesz, M. (1987) Structure-property predictions for new planar forms of carbon: Layered phases containing sp^2 and sp atoms. *Journal of Chemical Physics*, 87 (11), 6687–6699. https://doi.org/10.1063/1.453405 (In English)

Chen, S., Moore, A. L., Cai, W. et al. (2010) Raman measurements of thermal transport in suspended monolayer graphene of variable sizes in vacuum and gaseous environments. *ACS Nano*, 5 (1), 321–328. https://doi.org/10.1021/nn102915x (In English)

Deb, J., Paul, D., Sarkar, U. (2020) Pentagraphyne: A new carbon allotrope with superior electronic and optical property. *Journal of Materials Chemistry C*, 8 (45), 16143–16150. https://doi.org/10.1039/d0tc04245e (In English)

Enyashin, A. N., Ivanovskii, A. L. (2011) Graphene allotropes. *Physica Status Solidi (b)*, 248 (8), 1879–1883. https://doi.org/10.1002/pssb.201046583 (In English)

Fan, Q., Yan, L., Tripp, M. W. et al. (2021) Biphenylene network: A nonbenzenoid carbon allotrope. *Science*, 372 (6544), 852–856. https://doi.org/10.1126/science.abg4509 (In English)

Fthenakis, Z. G., Lathiotakis, N. N. (2015) Graphene allotropes under extreme uniaxial strain: An ab initio theoretical study. *Physical Chemistry Chemical Physics*, 17 (25), 16418–16427. https://doi.org/10.1039/c5cp02412a (In English)

Gong, Z., Shi, X., Li, J. et al. (2020) Theoretical prediction of low-energy stone-wales graphene with an intrinsic type-III Dirac cone. *Physical Review B*, 101 (15), article 155427. https://doi.org/10.1103/physrevb.101.155427 (In English)

Haastrup, S., Strange, M., Pandey, M. et al. (2018) The computational 2D materials database: High-throughput modeling and discovery of atomically thin crystals. *2D Materials*, 5 (4), article 042002. http://doi.org/10.1088/2053-1583/Aacfc1 (In English)

Hansen-Dörr, A. C., Wilkens, L., Croy, A. et al. (2019) Combined molecular dynamics and phase-field modelling of crack propagation in defective graphene. *Computational Materials Science*, 163, 117–126. https://doi.org/10.1016/j.commatsci.2019.03.028 (In English)

Hao, F., Fang, D., Xu, Z. (2011) Mechanical and thermal transport properties of graphene with defects. *Applied Physics Letters*, 99 (4), article 041901. https://doi.org/10.1063/1.3615290 (In English)

Jafri, S. H. M., Carva, K., Widenkvist, E. et al. (2010) Conductivity engineering of graphene by defect formation. *Journal of Physics D: Applied Physics*, 43 (4), article 045404. https://doi.org/10.1088/0022-3727/43/4/045404 (In English)

Kochnev, A. S., Ovid'ko, I. A., Semenov, B. N. (2014) Tensile strength of graphene containing 5-8-5 defects. *Reviews on Advanced Materials Science*, 37 (1/2), 105–110. (In English)

Kolesnikova, A. L., Rozhkov, M. A., Abramenko, N. D., Romanov, A. E. (2020) On mesoscopic description of interfaces in graphene. *Physics of Complex Systems*, 1 (4), 129–134. https://doi.org/10.33910/2687-153X-2020-1-4-129-134 (In English)

Lebedeva, I. V., Minkin, A. S., Popov, A. M., Knizhnik, A. A. (2019) Elastic constants of graphene: Comparison of empirical potentials and DFT calculations. *Physica E: Low-dimensional Systems and Nanostructures*, 108, 326–338. https://doi.org/10.1016/j.physe.2018.11.025 (In English)

Lee, C., Wei, X., Kysar, J. W., Hone, J. (2008) Measurement of the elastic properties and intrinsic strength of monolayer graphene. *Science*, 321 (5887), 385–388. https://doi.org/10.1126/science.1157996 (In English)

Los, J. H., Fasolino, A. (2003) Intrinsic long-range bond-order potential for carbon: Performance in Monte Carlo simulations of graphitization. *Physical Review B*, 68 (2), article 024107. https://doi.org/10.1103/physrevb.68.024107 (In English)

Maitra, U., Matte, H. S. S. R., Kumar, P., Rao, C. N. R. (2012) Strategies for the synthesis of graphene, graphene nanoribbons, nanoscrolls and related materials. *CHIMIA*, 66 (12), 941–948. https://doi.org/10.2533/chimia.2012.941 (In English)

Novoselov, K. S., Geim, A. K., Morozov, S. V. et al. (2004) Electric field effect in atomically thin carbon films. *Science*, 306 (5696), 666–669. https://doi.org/10.1126/science.1102896 (In English)

Novoselov, K. S., Geim, A. K., Morozov, S. V. et al. (2005) Two-dimensional gas of massless Dirac fermions in graphene. *Nature*, 438 (7065), 197–200. https://doi.org/10.1038/nature04233 (In English)

Pereira, L. F. C., Mortazavi, B., Makaremi, M., Rabczuk, T. (2016) Anisotropic thermal conductivity and mechanical properties of phagraphene: A molecular dynamics study. *RSC Advances*, 6 (63), 57773–57779. https://doi.org/10.1039/c6ra05082d (In English)

Polak, E., Ribiere, G. (1969) Note sur la convergence de méthodes de directions conjuguées. *Revue Française D'informatique et de Recherche Opérationnelle. Série Rouge*, 3 (16), 35–43. https://doi.org/10.1051/m2an/196903r100351 (In English)

Romanov, A. E., Kolesnikova, A. L., Orlova, T. S. et al. (2015) Non-equilibrium grain boundaries with excess energy in graphene. *Carbon*, 81 (1), 223–231. https://doi.org/10.1016/j.carbon.2014.09.053 (In English)

Romanov, A. E., Rozhkov, M. A., Kolesnikova, A. L. (2018) Disclinations in polycrystalline graphene and pseudo-graphenes. Review. *Letters on Materials*, 8 (4), 384–400. https://doi.org/10.22226/2410-3535-2018-4-384-400 (In English)

Rozhkov, M. A., Kolesnikova, A. L., Yasnikov, I. S., Romanov, A. E. (2018) Disclination ensembles in graphene. *Low Temperature Physics*, 44 (9), 918–924. https://doi.org/10.1063/1.5052677 (In English)

Shirazi, A. H. N. (2019) Molecular dynamics investigation of mechanical properties of single-layer phagraphene. *Frontiers of Structural and Civil Engineering*, 13 (2), 495–503. https://doi.org/10.1007/s11709-018-0492-4 (In English)

Stuart, S. J., Tutein, A. B., Harrison, J. A. (2000) A reactive potential for hydrocarbons with intermolecular interactions. *The Journal of Chemical Physics*, 112 (14), 6472–6486. https://doi.org/10.1063/1.481208 (In English)

Sun, H., Mukherjee, S., Singh, C. V. (2016) Mechanical properties of monolayer penta-graphene and phagraphene: A first-principles study. *Physical Chemistry Chemical Physics*, 18 (38), 26736–26742. https://doi.org/10.1039/c6cp04595b (In English)

Terrones, H., Terrones, M., Hernández, E. et al. (2000) New metallic allotropes of planar and tubular carbon. *Physical Review Letters*, 84 (8), 1716–1719. https://doi.org/10.1103/physrevlett.84.1716 (In English)

Tersoff, J. (1988) Empirical interatomic potential for silicon with improved elastic properties. *Physical Review B*, 38 (14), 9902–9905. https://doi.org/10.1103/PhysRevB.38.9902 (In English)

Wang, Z., Zhou, X.-F., Zhang, X. et al. (2015) Phagraphene: A low-energy graphene allotrope composed of 5–6–7 carbon rings with distorted Dirac cones. *Nano Letters*, 15 (9), 6182–6186. https://doi.org/10.1021/acs.nanolett.5b02512 (In English)

Wei, X., Fragneaud, B., Marianetti, C. A., Kysar, J. W. (2009) Nonlinear elastic behavior of graphene: Ab initio calculations to continuum description. *Physical Review B*, 80 (20), article 205407. http://doi.org/10.1103/PhysRevB.80.205407 (In English)

Wei, Y., Wu, J., Yin, H. et al. (2012) The nature of strength enhancement and weakening by pentagon–heptagon defects in graphene. *Nature Materials*, 11 (9), 759–763. https://doi.org/10.1038/nmat3370 (In English)

Winczewski, S., Shaheen, M. Y., Rybicki, J. (2018) Interatomic potential suitable for the modeling of penta-graphene: Molecular statics/molecular dynamics studies. *Carbon*, 126, 165–175. https://doi.org/10.1016/j.carbon.2017.10.002 (In English)

Xie, Q., Wang, L., Li, J. et al. (2020) General principles to high-throughput constructing two-dimensional carbon allotropes. *Chinese Physics B.*, 29 (3), article 037306. https://doi.org/10.1088/1674-1056/ab6c4b (In English)

Zhang, S., Zhou, J., Wang, Q. et al. (2015) Penta-graphene: A new carbon allotrope. *Proceedings of the National Academy of Sciences*, 112 (8), 2372–2377. https://doi.org/10.1073/pnas.1416591112 (In English)

Zhuo, Z., Wu, X., Yang, J. (2020) Me-graphene: A graphene allotrope with near zero Poisson's ratio, sizeable band gap, and high carrier mobility. *Nanoscale*, 12 (37), 19359–19366. https://doi.org/10.1039/d0nr03869e (In English)

Condensed Matter Physics. Dielectrics

UDC 537.9

EDN BQEZSV
https://www.doi.org/10.33910/2687-153X-2023-4-4-157-160

Influence of temperature conditions on thermostimulated depolarization of polyvinylidene fluoride films

E. A. Volgina[1], M. E. Merkulova✉[1], D. E. Temnov[1]

[1] Herzen State Pedagogical University of Russia, 48 Moika Emb., Saint Petersburg 191186, Russia

Authors

Elena A. Volgina, ORCID: 0000-0002-1536-5841, e-mail: Volgina.elena.1999@mail.ru

Maria E. Merkulova, e-mail: mashahf@icloud.com

Dmitry E. Temnov, ORCID: 0000-0002-9560-4346, e-mail: detem@yandex.ru

For citation: Volgina, E. A., Merkulova, M. E., Temnov, D. E. (2023) Influence of temperature conditions on thermostimulated depolarization of polyvinylidene fluoride films. *Physics of Complex Systems*, 4 (4), 157–160. https://www.doi.org/10.33910/2687-153X-2023-4-4-157-160 EDN BQEZSV

Received 11 September 2023; reviewed 6 October 2023; accepted 6 October 2023.

Funding: This study was supported by the Ministry of Education of the Russian Federation as part of the state-commissioned assignment (project No VRFY-2023-0005).

Abstract. The article investigates how the polarization temperature in the corona discharge field and pre-annealing modes of polyvinylidene fluoride copolymer films with tetrafluoroethylene effect thermally stimulated depolarization currents. The parameters of electrically active defects responsible for relaxation processes, the amount of charge (Q) released during depolarization and the value of the piezoelectric module d_{33} were determined for samples with different polarization temperatures. The article discusses the best temperature conditions for creating a piezoelectric state in polyvinylidene fluoride films.

Keywords: polyvinylidene fluoride, thermal activation spectroscopy, thermostimulated depolarization, corona discharge, electrically active defects

Introduction

Today, numerous fields of science and technology use a wide variety of devices. Many of them include dielectric materials made of polymer films. One of the promising materials in the field of electroactive polymers is polyvinylidene fluoride (PVDF) and its copolymer. PVDF is a piezoelectric polymer with unique properties lacking in traditional inorganic piezoelectrics, such as quartz or barium. The advantages of this material are high temperature stability during operation in the air, high rigidity at low temperatures, high mechanical strength, good electrical insulation, chemical and radiation resistance, and low flammability. These properties of polyvinylidene fluoride make the material suitable for use in various applications.

As of today, PVDF is the only polymer material with high piezoelectric properties. However, the technology of manufacturing piezoelectric elements from PVDF presents a few difficulties because high electric fields and elevated temperatures must be used in the polarization process (Shakirzyanov et al. 2016).

The paper investigates how polarization and pre-annealing temperatures impact the properties of PVDF-based piezoelectric elements during their manufacture. The paper also discusses optimal temperature parameters for polarization and pre-annealing of PVDF films.

Materials and methods

The study investigated F-2ME polyvinylidene fluoride (PVDF) films with a thickness of 20 microns and an orientation extraction coefficient of 3.5. The degree of crystallinity of the studied samples was approximately 55%, and the crystalline phase consisted mainly of the polar β-phase.

To create a piezoelectric state in the studied samples, polarization was applied in the corona discharge field at an elevated temperature ranging from 45 to 65 °C. The polarization time in the corona discharge field was 10 minutes, and the polarizing field was E = 1.2 MV/cm. During the polarization, the isometric state of the PVDF films under study was ensured.

The samples studied in the work were divided into three groups:

1) Without pre-annealing;
2) With pre-annealing at a temperature of 90°C in a free state for three hours;
3) With pre-annealing at a temperature of 90°C in an isometric state for three hours.

To study electrical relaxation in polymer materials, the method of thermally stimulated depolarization was used at the TSC II (France). The piezoelectric module d_{33} was determined using the YE2730A d_{33} Meter (USA).

Results

Fig. 1 shows TSD curves of PVDF samples that were pre-polarized at different Tp temperatures. It can be seen from the results that the maximum of the film depolarization current shifts to the high-temperature region with an increase in the polarization temperature of the samples.

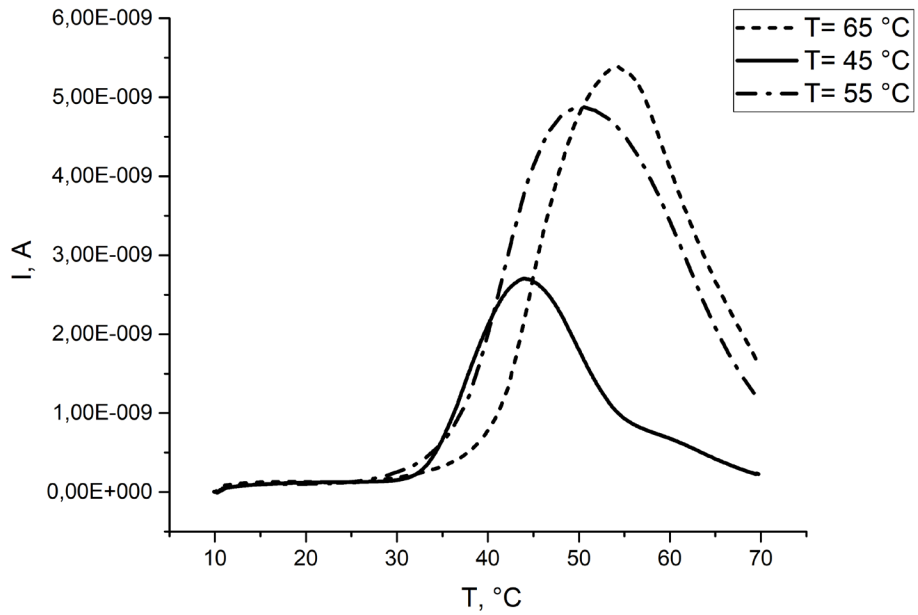

Fig. 1. TSD curves of PVDF samples with different polarization temperature Tp

According to (Butenko et al. 2008), the relaxation peak in this temperature region is associated with dipole relaxation in the crystalline phase or in regions intermediate between the crystalline and amorphous phases. The shift of the peak towards higher temperatures with an increase in the polarization temperature can be explained by the formation of more perfect and thermally more stable crystallites.

The activation energies of electrically active defects (EAD) responsible for this relaxation process were determined by the Garlick–Gibson method (Gorokhovatsky 1981) and are shown in Table 1.

 https://www.doi.org/10.33910/2687-153X-2023-4-4-157-160

Table 1. Activation energies of EAD (Ea), the amount of charge released during depolarization (Q) and the value of the piezoelectric module d_{33} for different polarization temperatures of Tp samples

T_p, °C	E_a, eV	Q, C	d_{33}, pC/N
45	0.65 ± 0.02	$(9.37 \pm 0.01) \times 10^{-7}$	26 ± 1
55	0.76 ± 0.02	$(9.54 \pm 0.01) \times 10^{-7}$	30 ± 1
65	0.81 ± 0.02	$(9.72 \pm 0.01) \times 10^{-7}$	32 ± 1

As the polarization temperature increases, the area under the graph also increases and, consequently, the total number of relaxers that participate in the polarization process increases.

Thus, with an increase in the polarization temperature of PVDF films in the isometric state, the activation energy of electrically active defects and their number increases resulting in larger and more stable crystallites.

The mechanical relaxation of PVDF (Gorokhovatsky et al. 2020) developing in the same temperature region allows us to conclude that the electrical and mechanical properties of this material are closely interrelated. Mechanical stresses arising during heating can contribute to the formation of thermally stable crystalline regions in the polymer. This is confirmed by a slight increase in the piezoelectric module d_{33} of the studied samples observed with an increase in the polarization temperature with all other conditions being equal (Table 1).

From the above results, the optimal polarization temperature is Tp = 65°C. A further increase in temperature leads to numerous electrical breakdowns of the sample.

Figure 2 shows the results of thermally stimulated depolarization of samples with different heat treatments carried out before the polarization.

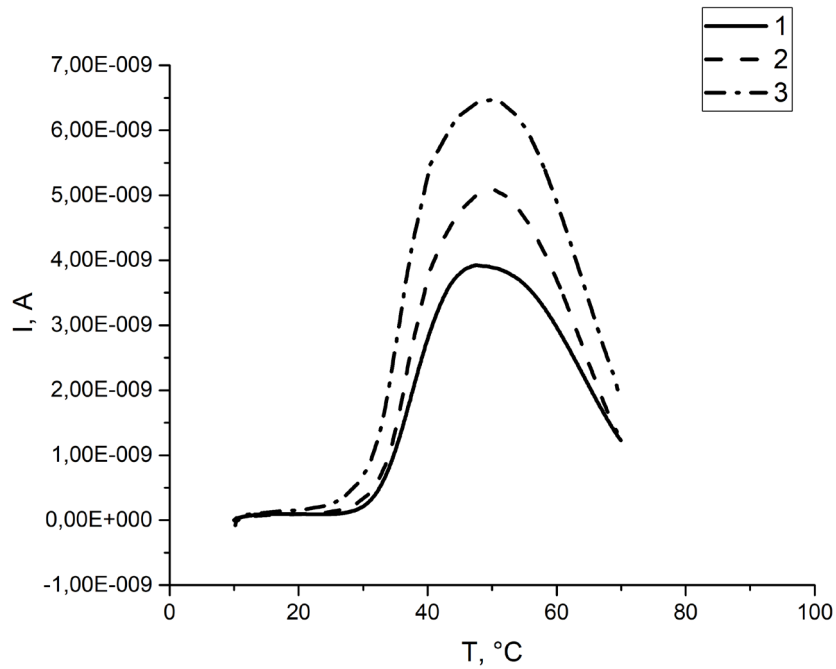

Fig. 2. TSD curves for PVDF samples polarized at Tp = 65° C with various preliminary temperature treatments: 1—without pre–annealing; 2—with pre-annealing in a non-isometric (free) state; 3—with pre-annealing in an isometric state

The position of the TSD peak does not depend on the conditions of heat treatment, however, the largest area under the curve is observed when isometric annealing is performed.

The obtained results show a pattern: PVDF samples pre-annealed in an isometric state have the largest area under the curve. This indicates that mechanical relaxation and polarization of PVDF are strongly interconnected.

Consequently, an increase in the time spent by the PVDF film in a mechanically stressed state (more than 3 hours for sample 3 and10 minutes for sample 1) leads to an increase in the number of crystallites involved in the polarization of samples.

Conclusions

The study of polarization and pre-annealing temperature regimes in PVDF films allows us to conclude that the retention of samples in an isometric state at an elevated temperature contributes to the improvement of their piezoelectric properties. This can be explained by the formation of more perfect crystallites during such annealing.

Preliminary annealing of samples in the isometric state at T = 90°C for 3 hours, followed by polarization at a temperature of Tp = 65°C in the corona discharge field, is the best temperature regime for creating a piezoelectric state in PVDF films.

Conflict of Interest

The authors declare that there is no conflict of interest, either existing or potential.

Author Contributions

All the authors discussed the final work and took part in writing the article.

References

Butenko, A. F., Fedosov, S. N., Sergeeva, A. E. (2008) Components of depolarization currents in polyvinylidene fluoride caused by relaxation of homo- and heterocharge. *Photoelectronics*, 17, 108–112. (In English)

Gorokhovatsky, Yu. A. (1981) *Osnovy termodepolyarizatsionnogo analiza [Fundamentals of thermodepolarization analysis]*. Moscow: Nauka Publ., 176 p. (In Russian)

Gorokhovatsky, Yu. A., Temnov, D. E., Sotova, Yu. I. (2020) Rheological parameters' effect on the electret properties of polyvinylidene fluoride. *St. Petersburg State Polytechnical University Journal—Physics and Mathematics*, 13 (4), 39–46. https://doi.org/10.18721/JPM.13403 (In English)

Shakirzyanov, R. I., Astakhov, V. A., Morchenko, A. T. et al. (2016) Elektrofizicheskie svojstva PVDF i sistem na ego osnove [Electrophysical properties of PVDF and systems based on it]. In: *Elektromagnitnoe pole i materialy (Fundamental'nye fizicheskie issledovaniya) [Electromagnetic Field and Materials (Fundamental physical research)]*. Moscow: Infra-M Publ., pp. 343–358. (In Russian)

Condensed Matter Physics.
Theory of condensed matter

UDC 538.9

EDN MYYBEC
https://www.doi.org/10.33910/2687-153X-2023-4-4-161-175

Complex non-exponential form of damped vibrations in uniaxially oriented polymeric materials with one mechanical degree of freedom

D. S. Vavilov[1], O. B. Prishchepenok✉[1], P. P. Rymkevich[1]

[1] Military Space Academy named after A. F. Mozhaysky, 13 Zhdanovskaya Emb., Saint Petersburg 197198, Russia

Authors

Dmitry S. Vavilov, ORCID: 0000-0002-0137-152X, e-mail: londr@yandex.ru

Olga B. Prishchepenok, ORCID: 0000-0002-1030-2489, e-mail: illada793@gmail.com

Pavel P. Rymkevich, ORCID: 0000-0002-9362-0561, e-mail: romallaa@yandex.ru

For citation: Vavilov, D. S., Prishchepenok, O. B., Rymkevich, P. P. (2023) Complex non-exponential form of damped vibrations in uniaxially oriented polymeric materials with one mechanical degree of freedom. *Physics of Complex Systems*, 4 (4), 161–175. https://www.doi.org/10.33910/2687-153X-2023-4-4-161-175 EDN MYYBEC

Received 11 September 2023; reviewed 6 October 2023; accepted 6 October 2023.

Funding: The study did not receive any external funding.

Abstract. In the present paper the relaxation properties of uniaxially oriented polymer threads are investigated. Vibrational relaxation in mechanical system with one degree of freedom is analyzed. This system consists of a heavy weight suspended on a light thread made of a uniaxially oriented polymer material.
The authors experimentally confirmed the existence of beats for a number of polymer materials (polycapromide, SVM, Terlon, Armos, etc.) at a certain static load level below the glass transition temperature. A physical explanation is given for the existence of the second vibration mode.
On the one hand, elastic oscillations occur in the system, on the other hand, according to the barrier model, oscillations of the occupation numbers of energy levels take place. Thus, another vibration mode arises, associated with highly elastic deformation, since highly elastic deformation is determined by the occupation numbers of the corresponding states. At close frequencies the beat effect is observed.

Keywords: uniaxially oriented polymeric materials, longitudinal low amplitude oscillations, highly elastic deformation, constitutive equation, beats

Introduction

The authors studied the elastic-relaxation properties of uniaxially oriented polymer threads in the dynamic mode of deformation. A theoretical explanation of the beat's occurrence is proposed.

In the second half of the last century the effects of occurrence of vibrational relaxation in some systems were discovered. For instance, the phenomenon of the occurrence of current oscillations in a homogeneous multi-valley semiconductor placed in a strong electric field was discovered—the Gunn effect (Gunn 1963). In chemistry, it is the Belousov-Zhabotinsky reaction (Belousov 1982; Zhabotinskii 1974)—a class of chemical reactions occurring in an oscillatory mode, in which some reaction parameters (color, concentration of components, temperature, etc.) change periodically, forming a complex spatio-temporal structure of the reaction medium. In the present article vibrational relaxation in a mechanical system with one degree of freedom is analyzed. This system consists of a heavy weight suspended on a light thread made of a uniaxially oriented polymer material below the glass transition temperature.

Previously, in (Romanova et al. 2000; 2005; 2007b; Rymkevich et al. 2014) for a number of studied polymer threads (SVM, lavsan, terlon, etc.), it was found that in a certain range of mechanical stresses

(or levels of static deformation) a complex non-exponential form of damped oscillations or beats schematically presented in Fig. 1 is observed, which is difficult to explain using the traditional description.

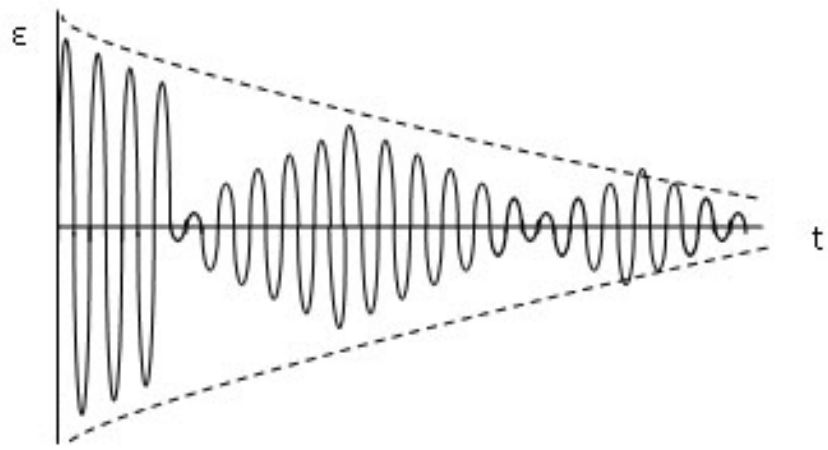

Fig. 1. Beatings (Amplitude-Modulated Free Oscillations)

The deformation curve in Fig. 1 can be represented at least as the result of the addition of two vibration modes. The question is why the second mode of oscillations appears in a mechanical system that formally has one degree of freedom. There are at least two explanations for this phenomenon. The first one is that the material under consideration obeys non-linear differential equations. The second one is that there are "hidden" degrees of freedom in the system. The authors adhere to the second explanation, because nonlinear equations should be linearized when studying low-amplitude oscillations. From the point of view of mechanics, the method of integral transformations based on the Boltzmann-Volterra equations when describing the mechanical properties of highly oriented polymers is often used (Gorshkov et al. 2004; Makarov et al. 2015; Romanova et al. 2007a; Stalevich et al. 2005). The authors of this article had previously shown that the fact of the presence of beats requires the existence of an oscillatory relaxation core, which, in principle, does not contradict the laws of mechanics (Rabotnov 1988), but requires additional explanations. Various rheological models of uniaxially oriented polymeric materials were considered in (Gorshkov et al. 2015; Rymkevich et al. 2021). In particular, a rheological model of polymer filament with hidden degrees of freedom was proposed in (Gorshkov et al. 2023). The described model consists not only of a spring and a damper, but also of a spiral visco-elastic element connected in series to them (Fig. 2).

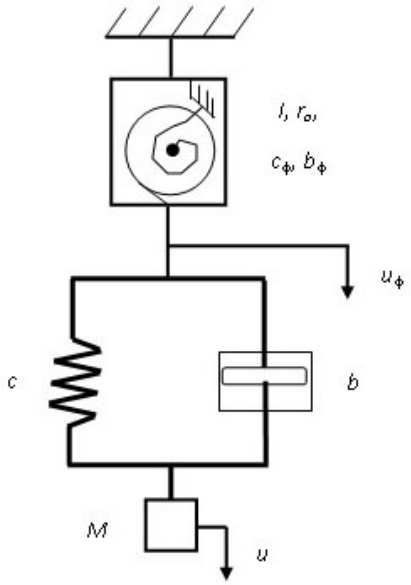

Fig. 2. Structural rheological model of a polymer thread with a spiral visco-elastic element

 https://www.doi.org/10.33910/2687-153X-2023-4-4-161-175

This mechanical model is a system with two degrees of freedom. One degree of freedom corresponds to translational motion u, the other one to rotational (rotary) motion φ. Rotational motion (rotational degree of freedom) is a hidden from the "macro-observer" form of motion. The transformation of the rotational motion of the ball into translational movement ensures the occurrence of an oscillatory beating mode. This rheological model can sufficiently describe the experimental results but does not provide any physical explanation. The authors propose to consider the complex and diverse supramolecular structure of oriented polymer materials as a set of different groups of macromolecules (clusters) in one of the possible stable states, separated by energy barriers (Gorshkov et al. 2013; Romanova 2007b).

As it was shown in (Rymkevich 2018), regardless of the conformational models considered, all allowed highly elastic (conformational) states differ from each other only in the heights and widths of the energy barriers between them. Therefore, the following assumptions for describing oriented polymer materials are accepted:

(a) polymer macromolecules contain groups of molecules in different stable states separated by energy barriers;

(b) the elastic part of the deformation obeys Hooke's law

$$x = \frac{\sigma}{E_0},$$

where E_0 is the true elastic modulus.

Here and further, we assume that the total deformation of a polymer material can be represented as the sum of two terms—elastic (x) and highly elastic (ε_{he}), i. e.:

$$\varepsilon = x + \varepsilon_{he}.$$

Groups of macromolecules that can change their conformations during deformation will be called active conformational elements (ACE). We present active conformational elements with two stable energy states in the form of a model depicted in Fig. 3.

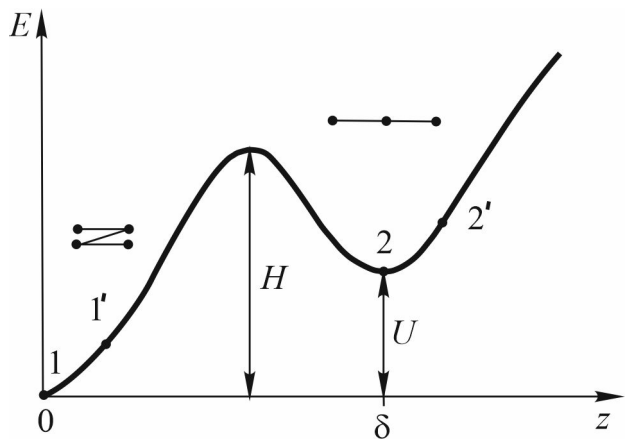

Fig. 3. Energy diagram of ACE as a function of cluster size for two stable states

In the energy diagram (Fig. 3), these two stable states with energies $E_1 = 0$ and $E_2 = U$ are respectively separated by a potential barrier of height $H > 0$. We will call state 1 "conditionally collapsed", and state 2—"conditionally expanded". In general case the value of the energy gap can be either greater or less than zero and depends on the type of conformational states. During the transition from state 1 to state 2, the geometry of the ACE changes, which is accompanied by absolute deformation $\delta > 0$. And the third assumption:

(c) all ACEs are fully described by three numerical characteristics: barrier height H, energy difference U and deformation quantum δ.

An attempt was proposed in (Golovina et al. 2022) to explain the observed complex amplitude modulation using a two-stable state theory within the framework of the assumptions proposed above. But such a theory leads to a nonlinear differential equation, which does not allow us to give a complete explanation of the indicated phenomenon of amplitude modulation within the framework of the observed frequencies. Therefore, the authors propose to consider a theory with three stable states.

Constitutive equation for the three-level model

Let us consider a model with three stable energy states (Fig. 4).

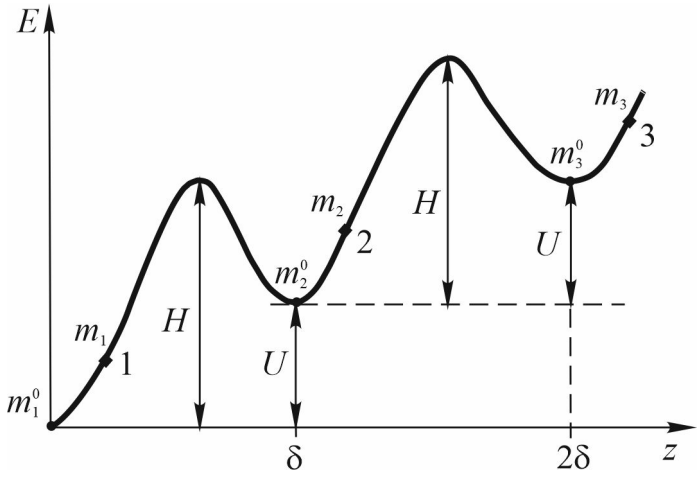

Fig. 4. Energy diagram of ACE as a function of cluster size for three stable states

A forced orientation of macromolecules takes place in the amorphous layers of a highly oriented polymer material under external load. Then, according to the barrier theory, groups (clusters) of macromolecules move from one stable state to another. It should be noted that in the absence of load (elastic deformation), the stable states are points with the number of clusters per unit length m_1^0, m_2^0 and m_3^0. The loaded state becomes stable under external load (points 1, 2 and 3 with occupation numbers m_1^0, m_2^0 and m_3^0)—Fig. 4. And according to the barrier theory, we can write a balance equation for these numbers:

$$\begin{cases} \dfrac{dm_1}{dt} = -m_1 W_{\rightarrow} + m_2 W_{\leftarrow} \\ \dfrac{dm_2}{dt} = -m_2 (W_{\rightarrow} + W_{\leftarrow}) + m_1 W_{\rightarrow} + m_3 W_{\leftarrow} \\ \dfrac{dm_3}{dt} = -m_3 W_{\leftarrow} + m_2 W_{\rightarrow} \end{cases} \quad (1)$$

The state of an ideal highly oriented polymer material, consisting only of clusters of one type with an elastic modulus E_0, is characterized by the barrier height H (corresponding to the necessary energy reserve for another rotation of a chain link), the energy gap width U (corresponding to the difference in energies of two neighboring stable states), the quantum deformation value δ and parameter $\bar{\gamma}$—the so-called structure-sensitive element, depending on the type of material (Romanova et al. 2005; Rymkevich 2018). In practice, *U* mostly takes negative values. We will measure all quantities H and U in kelvins as is customary in molecular physics.

In system of equations (1), the change in the number of clusters in the N stable state will be determined by the number of clusters moving from this state to the right (see Fig. 4) with probability $W_{\rightarrow}$ per second, and the number of clusters moving from this state to the left with probability $W_{\leftarrow}$ per second.

 https://www.doi.org/10.33910/2687-153X-2023-4-4-161-175

Let us assume that this system of clusters obeys Boltzmann statistics, according to which the probability of a transition from state 1 to state 2 (and similarly the probability from state 2 to state 1) is determined by the heights of the energy barriers H_{12} and H_{21}, respectively:

$$P_{12} = P_0 \cdot \exp(-H_{12}/T),$$

$$P_{21} = P_0 \cdot \exp(-H_{21}/T).$$

The number of transitions per second (fraction) is denoted as:

$$W_{\rightarrow} = \nu_0 \cdot \exp(-H_{\rightarrow}/T),$$

$$W_{\leftarrow} = \nu_0 \cdot \exp(-H_{\leftarrow}/T),$$

where ν_0 is the frequency of approach to the barrier per second.

During the deformation of material, the height of the barrier in the direction of orientation decreases by the value proportional to the square of the mechanical elastic stress (for example, rotation of Kuhn segment from one stable state to another). Therefore, the value $H_{\rightarrow}$ is assumed to be equal to:

$$H_{\rightarrow} = H - \bar{\gamma} x^2,$$

where x stands for the value of elastic deformation ($x = \sigma/E_0$).

As can be seen from Fig. 4, $H_{\leftarrow} = H - U + \bar{\gamma} x^2$.

As is customary in thermodynamics, it is more convenient to use the reduced energy values. Thus, we introduce the following notation: $H^* = H/T$, $U^* = U/T$, $\gamma = \bar{\gamma}/T$ and $\exp(U^*) = A$. Here are the possible variants: $A < 1$ (if a more stable state is a more oriented one—which is the most common in practice), $A \approx 1$ (if the energies of these states are approximately the same), and $A > 1$ (in the opposite case). Therefore:

$$W_{\rightarrow} = \nu_0 \cdot \exp(-H^*_{\rightarrow}) = \nu_0 \cdot \exp(-H_{\rightarrow}/T) = \nu_0 \cdot \exp(-H/T + \gamma x^2) =$$
$$= \nu_0 \cdot \exp(-H^*) \cdot \exp(\gamma x^2) = \frac{1}{\tau_0} \exp(-H^*) \cdot \exp(\gamma x^2),$$

$$W_{\leftarrow} = \nu_0 \cdot \exp(-H^*_{\leftarrow}) = \nu_0 \cdot \exp(-H_{\leftarrow}/T) = \nu_0 \cdot \exp(-H/T + U/T - \gamma x^2) =$$
$$= \nu_0 \cdot \exp(-H^*) \cdot \exp(U^*) \cdot \exp(-\gamma x^2) = \frac{1}{\tau_0} \exp(-H^*) \cdot \exp(U^*) \cdot \exp(-\gamma x^2).$$

Most polymer materials that are oriented (deformed) in this way differ only in barrier heights, deformation quantum and number of clusters. That is why it is convenient to introduce the characteristic relaxation time. In system (1), it is expedient to switch to dimensionless time $\tau = t/\tau_\partial$, where $\tau_\partial = \tau_0 \cdot \exp(H^*)$ is the relaxation time, $\tau_0 = 1/\nu_0$ is the material constant characterizing the average transition time with barrier height $H \to 0$. Then after introducing the new notation a more compact representation is obtained:

$$R_+ = W_{\rightarrow} \cdot \tau_\partial = \frac{1}{\tau_0} \exp(-H^*) \cdot \exp(\gamma x^2) \cdot \tau_0 \cdot \exp(H^*) = \exp(\gamma x^2), \quad (2)$$

$$R_- = W_{\leftarrow} \cdot \tau_\partial = \frac{1}{\tau_0} \exp(-H^*) \cdot \exp(U^*) \cdot \exp(-\gamma x^2) \cdot \tau_0 \cdot \exp(H^*) =$$
$$= \exp(U^*) \cdot \exp(-\gamma x^2) = A \cdot \exp(-\gamma x^2). \quad (3)$$

Further we will take into account that $R_+ \cdot R_- = A$.

We denote the derivative of a certain value X with respect to a dimensionless parameter τ as $\overset{o}{X} = \frac{d}{d\tau}$. Taking into consideration the introduced notation when switching to dimensionless time, we obtain a system of equations (4) equivalent to system (1):

$$\begin{cases} \overset{o}{m}_1 = -m_1 R_+ + m_2 R_- \\ \overset{o}{m}_2 = -m_2 (R_+ + R_-) + m_1 R_+ + m_3 R_- \\ \overset{o}{m}_3 = -m_3 R_- + m_2 R_+ \ . \end{cases} \tag{4}$$

Taking into account the normalization condition (law of conservation of the cluster number):

$$m_0 = m_1 + m_2 + m_3 . \tag{5}$$

Here m_0 is the total number of clusters per length of the given polymeric sample.

The magnitude of the highly elastic part of the deformation can be represented as the difference between the total ε and elastic deformation x:

$$\varepsilon_{he} = \varepsilon - x = \delta\left[m_2 - m_2^0 \right] + 2\delta\left[m_3 - m_3^0 \right] = \delta(m_2 + 2m_3) - \Delta_0 , \tag{6}$$

where $\Delta_0 = \delta(m_2^0 + 2m_3^0)$ is the initial deformation.

Let us express m_1 from the normalization condition (5) and substitute it into (4), thereby eliminating m_1^0 from the system of equations:

$$\begin{cases} \overset{o}{m}_2 = -m_2 (R_+ + R_-) + (m_0 - m_2 - m_3) R_+ + m_3 R_- = -m_3 (R_+ - R_-) + m_0 R_+ - m_2 (2R_+ + R_-) \\ \overset{o}{m}_3 = -m_3 R_- + m_2 R_+ . \end{cases} \tag{7}$$

Let us write down the first derivatives of R_+ and R_+:

$$\overset{o}{R}_+ = R_+ \cdot 2\gamma x \overset{o}{x} = R_+ \alpha \text{ , where } \alpha = 2\gamma x \overset{o}{x} \tag{8}$$

$$\overset{o}{R}_- = -R_- \alpha . \tag{9}$$

Let us write the first derivative of the highly elastic part of the deformation with respect to the parameter τ:

$$\begin{aligned} \overset{o}{\varepsilon}_{he} &= \delta\left[\overset{o}{m}_2 + 2\overset{o}{m}_3 \right] = \delta\left[\left\{ m_0 R_+ - m_2 (2R_+ + R_-) - m_3 (R_+ - R_-) \right\} + 2m_2 R_+ - 2m_3 R_- \right] = \\ &= \delta\left[m_0 R_+ - m_3 (R_+ + R_-) - m_2 R_- \right]. \end{aligned} \tag{10}$$

Let us write the second derivative of the highly elastic part of the deformation with respect to the parameter τ:

$$\overset{oo}{\varepsilon}_{he} = \delta\left\{ -\left[\overset{o}{m}_3 (R_+ + R_-) + \overset{o}{m}_2 R_- \right] + \alpha\left[m_0 R_+ - m_3 (R_+ - R_-) + m_2 R_- \right] \right\}. \tag{11}$$

After substituting $\overset{o}{m}_2$ and $\overset{o}{m}_3$ from system of equations (7) and performing algebraic transformation we obtain

$$\overset{oo}{\varepsilon}_{he} = \delta\left\{ \alpha\left[m_0 R_+ - m_3 (R_+ - R_-) + m_2 R_- \right] - \left[m_0 A - m_2 (A + R_-^2 - R_+^2) - m_3 \cdot 2A \right] \right\}. \tag{12}$$

 https://www.doi.org/10.33910/2687-153X-2023-4-4-161-175

In expressions (6) and (10) we select the terms with unknown values and obtain a system of equations with these two unknowns:

$$\begin{cases} \delta(m_2+2m_3)=\varepsilon_{he}+\Delta_0 \\ \delta\left[m_2R_-+m_3(R_++R_-)\right]=\delta m_0R_+-\overset{\mathbf{o}}{\varepsilon}_{he}. \end{cases} \tag{13}$$

Solving system (13), we obtain expressions for m_2 and m_3.

Finally, by means of algebraic transformations and substituting expressions for m_2 and m_3, we obtain the following second-order differential equation:

$$\begin{gathered} \overset{\mathbf{oo}}{\varepsilon}_{he}+\overset{\mathbf{o}}{\varepsilon}_{he}\left[R_+-R_--\frac{\alpha(R_++R_-)}{R_+-R_-}\right]+\varepsilon_{he}\left[R_+^2+R_-^2+A+\frac{2A\alpha}{R_+-R_-}\right]- \\ -\delta m_0(2R_+^2+A)+\Delta_0(R_+^2+R_-^2+A)+\alpha\delta m_0\cdot 2A-\frac{\alpha\Delta_0\cdot 2A}{R_+-R_-}=0. \end{gathered} \tag{14}$$

Since equation (14) is a differential equation of the second order in time, the solution of this equation in certain cases leads to an oscillatory relaxation mode. Thus, even in a system with one external degree of freedom, when the sample is periodically loaded with a certain frequency, interaction between this external and natural frequency is possible. This fact is supported by experiments on the study of low-amplitude longitudinal vibrations on highly oriented polymer threads in (Gorshkov 2004; Stalevich et al. 2005).

Separation of the static and dynamic parts of highly elastic deformation in the basic constitutive equation

Let us present equation (14) in the following form:

$$\begin{gathered} (R_+-R_-)\overset{\mathbf{oo}}{\varepsilon}_{he}+\overset{\mathbf{o}}{\varepsilon}_{he}\left[(R_+-R_-)^2-\alpha(R_++R_-)\right]+ \\ +\varepsilon_{he}\left[(R_+^2+R_-^2)(R_+-R_-)+A(R_+-R_-)+2A\alpha\right]= \\ =\delta m_0(2R_+^2+A)(R_+-R_-)-\Delta_0(R_+^2+R_-^2+A)(R_+-R_-)- \\ -2\delta m_0\alpha A(R_+-R_-)+2A\alpha\Delta_0. \end{gathered} \tag{15}$$

In the sequel, we will separate the static and dynamic components of this equation. Let us separate the static and dynamic components from the highly elastic part of deformation:

$$\varepsilon_{he}=(\varepsilon^0-x^0)+(\theta-y)=\varepsilon_{he}^0+\mu,$$

where ε^0, x^0, ε_{he}^0 are static components of full, elastic and highly elastic deformation; let us denote the dynamic part of highly elastic deformation as $\mu=(\theta-y)$.

Taking into account that $x=x^0+y$, expressions for R_+ and R_- take the form:

$$R_+=\exp(\gamma x^2)=\exp\left[\gamma(x^0+y)^2\right]=(1+2\gamma x^0y)\cdot\exp\left[\gamma(x^0)^2\right],$$

$$R_-=A\cdot\exp(-\gamma x^2)=A\cdot\exp\left[-\gamma(x^0+y)^2\right]=(1-2\gamma x^0y)\cdot A\cdot\exp\left[-\gamma(x^0)^2\right].$$

Let us introduce the notation: $R_+^0=\exp\left[\gamma(x^0)^2\right]$; $R_-^0=A\cdot\exp\left[-\gamma(x^0)^2\right]$;

$$\nu=2\gamma x^0y;\ \alpha=2\gamma x\overset{\mathbf{o}}{x}=2\gamma x\overset{\mathbf{o}}{y}=\overset{\mathbf{o}}{\nu}.$$

Now let us transform the factors at $\overset{oo}{\varepsilon}_{he}$, $\overset{o}{\varepsilon}_{he}$ and ε_{he} in equation (15). Firstly, the factor at $\overset{oo}{\varepsilon}_{he}$:

$$\begin{aligned}(R_+ - R_-) &= R_+^0 \cdot (1 + 2\gamma x^0 y) - R_-^0 \cdot (1 - 2\gamma x^0 y) = \\ &= R_+^0 \cdot (1+\nu) - R_-^0 \cdot (1-\nu) = (R_+^0 - R_-^0) + \nu(R_+^0 + R_-^0).\end{aligned} \tag{16}$$

Secondly, we transform the factor at $\overset{o}{\varepsilon}_{he}$ (here and below we will neglect the terms containing ν^2 and $\nu \cdot \overset{o}{\nu}$ because of a higher order of smallness):

$$\begin{aligned}&(R_+ - R_-)^2 - \alpha(R_+ + R_-) = (R_+^0 - R_-^0)^2 + 2\left((R_+^0)^2 - (R_-^0)^2\right)\nu - \alpha(R_+^0(1+\nu) + \\ &+ R_-^0(1-\nu)) = (R_+^0 - R_-^0)^2 + 2\left((R_+^0)^2 - (R_-^0)^2\right)\nu - (R_+ + R_-)\cdot\overset{o}{\nu}.\end{aligned} \tag{17}$$

Thirdly, we transform the factor at ε_{he}:

$$\begin{aligned}&(R_+^2 + R_-^2)(R_+ - R_-) + A(R_+ - R_-) + 2A\alpha = \\ &= \left[(R_+^0)^2(1+\nu)^2 + (R_-^0)^2(1-\nu)^2\right]\cdot\left[(R_+^0 - R_-^0) + \nu(R_+^0 + R_-^0)\right] + \\ &+ A\cdot\left[(R_+^0 - R_-^0) + \nu(R_+^0 + R_-^0)\right] + 2A\overset{o}{\nu} = \\ &= \left[\left((R_+^0)^2 + (R_-^0)^2\right) + 2\left((R_+^0)^2 - (R_-^0)^2\right)\nu\right]\cdot\left[(R_+^0 - R_-^0) + \nu(R_+^0 + R_-^0)\right] + \\ &+ A\cdot\left[(R_+^0 - R_-^0) + \nu(R_+^0 + R_-^0)\right] + 2A\overset{o}{\nu} = \left((R_+^0)^2 + (R_-^0)^2\right)(R_+^0 - R_-^0) + \\ &+ \nu\left[2\left((R_+^0)^2 - (R_-^0)^2\right)(R_+^0 - R_-^0) + (R_+^0 + R_-^0)\left((R_+^0)^2 + (R_-^0)^2\right)\right] + \\ &+ A\cdot\left[(R_+^0 - R_-^0) + \nu(R_+^0 + R_-^0)\right] + 2A\overset{o}{\nu} = \\ &= \left((R_+^0)^2 + (R_-^0)^2\right)(R_+^0 - R_-^0) + \nu(R_+^0 + R_-^0)\left(3\left((R_+^0)^2 + (R_-^0)^2\right) - 4A\right) + \\ &+ A\cdot\left[(R_+^0 - R_-^0) + \nu(R_+^0 + R_-^0)\right] + 2A\overset{o}{\nu}.\end{aligned} \tag{18}$$

Now let us rewrite the left side of equation (15), substituting the resulting expressions (16), (17), (18) for the factors at $\overset{oo}{\varepsilon}_{he}$, $\overset{o}{\varepsilon}_{he}$ and ε_{he} and substituting $\varepsilon_{he} = \varepsilon_{he}^0 + \mu$. Neglecting the terms containing $\overset{oo}{\mu}\cdot\nu$ and $\overset{oo}{\mu}\cdot\overset{o}{\nu}$ as being of a higher order of smallness, we obtain the following on the left side of (15):

$$\begin{aligned}&(R_+^0 - R_-^0)\overset{oo}{\mu} + (R_+^0 - R_-^0)^2\overset{o}{\mu} + \left[\left((R_+^0)^2 + (R_-^0)^2\right)(R_+^0 - R_-^0) + A(R_+^0 - R_-^0)\right]\mu + \\ &+ \varepsilon_{he}^0\left[\left((R_+^0)^2 + (R_-^0)^2\right)(R_+^0 - R_-^0) + A(R_+^0 - R_-^0)\right] + \\ &+ \varepsilon_{he}^0\left[\nu(R_+^0 + R_-^0)\left(3\left((R_+^0)^2 + (R_-^0)^2\right) - 4A\right) + A(R_+^0 + R_-^0)\nu + 2A\overset{o}{\nu}\right].\end{aligned} \tag{19}$$

Let us transform the right side of (15):

 https://www.doi.org/10.33910/2687-153X-2023-4-4-161-175

$$\begin{aligned}
&\delta m_0(2R_+^2+A)(R_+-R_-)-\Delta_0(R_+^2+R_-^2+A)(R_+-R_-)-\\
&-2\delta m_0\alpha A(R_+-R_-)+2A\alpha\Delta_0=\delta m_0\left[2(R_+^0)^2(1+\nu)^2+A\right]\cdot\left[(R_+^0-R_-^0)+\nu(R_+^0+R_-^0)\right]-\\
&-\Delta_0\left[(R_+^0)^2(1+\nu)^2+(R_-^0)^2(1-\nu)^2+A\right]\cdot\left[(R_+^0-R_-^0)+\nu(R_+^0+R_-^0)\right]-\\
&-2\delta m_0A\overset{o}{\nu}(R_+^0-R_-^0)+2A\Delta_0\overset{o}{\nu}=\\
&=\delta m_0\left[2(R_+^0)^2+A\right]\cdot(R_+^0-R_-^0)-\Delta_0\left[(R_+^0)^2+(R_-^0)^2+A\right](R_+^0-R_-^0)+\\
&+\delta m_0\left\{4(R_+^0)^2(R_+^0-R_-^0)+(2(R_+^0)^2+A)(R_+^0+R_-^0)\right\}\nu-\\
&-\Delta_0\left\{\left(2(R_+^0)^2-2(R_-^0)^2\right)(R_+^0-R_-^0)+\left((R_+^0)^2+(R_-^0)^2+A\right)(R_+^0+R_-^0)\right\}\nu+\\
&+\Delta_0\cdot2A\overset{o}{\nu}-2\delta m_0A(R_+^0-R_-^0)\overset{o}{\nu}.
\end{aligned}\tag{20}$$

Let us consider equation (15), which contains only the dynamic part (we equate the left (19) and the right (20) parts, leaving only the terms with factors in the form μ and ν, as well as their derivatives). In addition, we take into account that the terms with the multiplier Δ_0 (initial deformation) will also disappear in the dynamics (this is the damping part). Then we obtain:

$$\begin{aligned}
&(R_+^0-R_-^0)\overset{oo}{\mu}+(R_+^0-R_-^0)^2\overset{o}{\mu}+(R_+^0-R_-^0)\left[(R_+^0)^2+(R_-^0)^2+A\right]\mu+\\
&+\varepsilon_{he}^0\left[(R_+^0+R_-^0)\left(3\left((R_+^0)^2+(R_-^0)^2\right)-4A\right)\nu+A(R_+^0+R_-^0)\nu+2A\overset{o}{\nu}\right]=\\
&=\delta m_0\left\{4(R_+^0)^2(R_+^0-R_-^0)+(2(R_+^0)^2+A)(R_+^0+R_-^0)\right\}\nu-2\delta m_0A(R_+^0-R_-^0)\overset{o}{\nu}.
\end{aligned}\tag{21}$$

Study of low-amplitude longitudinal vibrations for highly oriented polymer threads

Let us consider low-amplitude oscillations in the following system: a load of mass m is suspended on a thread from the polymer sample under study. Initial thread length is denoted as L, S_0 stands for the cross-sectional area, σ_0 stress value at equilibrium is designated as σ_0 and σ during vibrations, E_0 is elastic modulus, Z is vertical coordinate Z (Fig. 5).

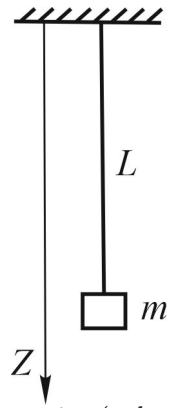

Fig. 5. Load of mass on a suspension (polymer thread) of initial length L

In equilibrium position: $mg=\sigma_0S_0$.

In oscillation mode: $mg-\sigma_0S_0-\delta\sigma S_0=m\ddot{Z}$; $Z=L\cdot\theta$,

where θ is the relative deformation.

The value of elastic deformation:

$$x = \frac{\sigma}{E_0} = \frac{\sigma_0}{E_0} + \frac{\delta\sigma}{E_0};\ x = x^0 + y.$$

Then for the oscillation mode we obtain the following equation:

$$mL\ddot{\theta} + yE_0S_0 = 0.$$

Dividing the latter by mL, we bring it to the form:

$$\ddot{\theta} + \Omega_0^2 \cdot y = 0,$$

where the following designation is introduced

$$\Omega_0^2 = \frac{E_0 S}{mL}. \tag{22}$$

Thus, a differential equation of harmonic oscillations is obtained, where Ω_0 is their frequency.

Here, just as before, we will introduce dimensionless variables, ensuring the universality of the curves characterizing various polymer samples. For this purpose, we use the notation:

$$\tilde{\Omega}_0 = \Omega_0 \cdot \tau_{\eth}. \tag{23}$$

Here, as before, $\tau = t/\tau_{\eth}$, where $\tau_{\eth}$ is the relaxation time. Then the vibration equation takes the following form:

$$\overset{oo}{\theta} + \tilde{\Omega}_0^2 \cdot y = 0. \tag{24}$$

Now, just as in Section 3, we apply the following notation:

$$\theta = \mu + y;\ \nu = 2\gamma x^0 y = Ky;\ \overset{o}{\nu} = K\overset{o}{y}.$$

Then equation (24) takes the following form:

$$\overset{oo}{\mu} + \overset{oo}{y} + \tilde{\Omega}_0^2 \cdot y = 0$$

Let us substitute and obtain:

$$\overset{oo}{\mu} + \frac{1}{K}\overset{oo}{\nu} + \frac{\tilde{\Omega}_0^2}{K} \cdot \nu = 0. \tag{25}$$

Analysis of the solution for low-amplitude longitudinal vibrations

Next, we will consider the obtained differential equations: the dynamic part of constitutive equation (21) and equation of small-amplitude oscillations (25). We will look for solutions of these equations in the following form:

$$\mu = \mu_0 \cdot \exp(\lambda\tau),$$

$$\nu = \nu_0 \cdot \exp(\lambda\tau).$$

Then equation (21) after substituting these expressions and simplification takes the form:

$$\lambda^2(R_+^0 - R_-^0)\mu_0 + \lambda(R_+^0 - R_-^0)^2\mu_0 + (R_+^0 - R_-^0)\left[(R_+^0)^2 + (R_-^0)^2 + A\right]\mu_0 +$$
$$+\varepsilon_{he}^0\left[(R_+^0 + R_-^0)\left(3\left((R_+^0)^2 + (R_-^0)^2\right) - 4A\right) + (R_+^0 + R_-^0)A + 2A\lambda\right]\nu_0 = .$$
$$= M_0\nu_0\left\{4(R_+^0)^2(R_+^0 - R_-^0) + (2(R_+^0)^2 + A)(R_+^0 + R_-^0) - 2A\lambda(R_+^0 - R_-^0)\right\}$$

 https://www.doi.org/10.33910/2687-153X-2023-4-4-161-175

Here and further below the notation $M_0 = \delta m_0$ is used.

To obtain a more compact representation, we use temporary notation for the coefficients at μ_0 and ν_0. Then the last equation takes the form:

$$\left[(R_+^0 - R_-^0)\lambda^2 + (R_+^0 - R_-^0)^2\lambda + G\right]\mu_0 + L\nu_0 + N\lambda\nu_0 = 0, \tag{26}$$

where $G = (R_+^0 - R_-^0)\left[(R_+^0)^2 + (R_-^0)^2 + A\right]$

$$L = \varepsilon_{he}^0\left[(R_+^0 + R_-^0)\left(3\left((R_+^0)^2 + (R_-^0)^2\right) - 4A\right) + (R_+^0 + R_-^0)A\right] -$$
$$-M_0\left[4(R_+^0)^2(R_+^0 - R_-^0) + (2(R_+^0)^2 + A)(R_+^0 + R_-^0)\right] =$$
$$= \varepsilon_{he}^0\left[3(R_+^0 + R_-^0)\left[(R_+^0)^2 + (R_-^0)^2 - A\right]\right] - M_0\left[R_+^0\left[6(R_+^0)^2 + (R_-^0)^2 - A\right]\right]$$

$$N = 2A\varepsilon_{he}^0 + 2A(R_+^0 - R_-^0)M_0.$$

Now consider equation (25), which after substituting solutions and simplification takes the form:

$$K\lambda^2\mu_0 + \left(\lambda^2 + \tilde{\Omega}_0^2\right)\cdot\nu_0 = 0. \tag{27}$$

Now we, therefore, have a system of algebraic equations (26) and (27) with respect to λ.

We will take into account that in practice we are dealing with polymeric materials for which:

$$R_+^0 = \exp\left[\gamma(x^0)^2\right] \gg 1;\ R_-^0 = A\cdot\exp\left[-\gamma(x^0)^2\right] \ll 1;\ A < 1.$$

Then the coefficients *L*, *G* and *N* in the equation take the form:

$$L = \varepsilon_{he}^0\left[3(R_+^0 + R_-^0)\left[(R_+^0)^2 + (R_-^0)^2 - A\right]\right] - M_0\left[R_+^0\left[6(R_+^0)^2 + (R_-^0)^2 - A\right]\right] =$$
$$= \varepsilon_{he}^0\cdot 3(R_+^0)^3 - M_0\cdot 6(R_+^0)^3 = 3(R_+^0)^3(\varepsilon_{he}^0 - 2M_0)$$

$$G = (R_+^0 - R_-^0)\left[(R_+^0)^2 + (R_-^0)^2 + A\right] \simeq (R_+^0)^3$$

$$N = 2A\varepsilon_{he}^0 + 2A(R_+^0 - R_-^0)M_0 = 2A\varepsilon_{he}^0 + 2AM_0R_+^0.$$

Let us rewrite equation (26):

$$\left[R_+^0\lambda^2 + (R_+^0)^2\lambda + (R_+^0)^3\right]\mu_0 + 3(R_+^0)^3(\varepsilon_{he}^0 - 2M_0)\nu_0 + 2A(\varepsilon_{he}^0 + M_0R_+^0)\lambda\nu_0 = 0$$

Let us divide everything into $(R_+^0)^3$:

$$\left[\frac{\lambda^2}{(R_+^0)^2} + \frac{\lambda}{R_+^0} + 1\right]\mu_0 + 3(\varepsilon_{he}^0 - 2M_0)\nu_0 + 2A\nu_0\frac{\lambda}{(R_+^0)^2}\left(M_0 + \frac{\varepsilon_{he}^0}{R_+^0}\right) = 0.$$

Let us introduce the notation: $\eta = \frac{\lambda}{(R_+^0)^2}$. Then we obtain:

$$\left[(R_+^0)^2\eta^2 + R_+^0\eta + 1\right]\mu_0 + 3(\varepsilon_{he}^0 - 2M_0)\nu_0 + 2A\nu_0\eta\left(M_0 + \frac{\varepsilon_{he}^0}{R_+^0}\right) = 0. \tag{28}$$

Let us consider equation (27). Let us divide it by $(R_+^0)^4$ and also use the notation $\eta = \frac{\lambda}{(R_+^0)^2}$. Then we obtain:

$$K\eta^2\mu_0 + \left(\eta^2 + \frac{\tilde{\Omega}_0^2}{(R_+^0)^4}\right)\cdot\nu_0 = 0. \tag{29}$$

Divide equation (28) by equation (29) and obtain:

$$\frac{(R_+^0)^2\eta^2 + R_+^0\eta + 1}{K\eta^2} = \frac{3(\varepsilon_{he}^0 - 2M_0) + 2A\eta\left(M_0 + \frac{\varepsilon_{he}^0}{R_+^0}\right)}{\eta^2 + \frac{\tilde{\Omega}_0^2}{(R_+^0)^4}}. \tag{30}$$

Let us introduce the notation:

$$3(\varepsilon_{he}^0 - 2M_0) = \psi;\ 2A\left(M_0 + \frac{\varepsilon_{he}^0}{R_+^0}\right) = \varphi;\ \frac{\tilde{\Omega}_0^2}{(R_+^0)^4} = \pi. \tag{31}$$

Then equation (30) takes the form:

$$\left((R_+^0)^2\eta^2 + R_+^0\eta + 1\right)\cdot\left(\eta^2 + \pi\right) = K\eta^2\left(\psi + \varphi\eta\right).$$

After that, applying algebraic transformations, we obtain:

$$(R_+^0)^2\eta^4 + \left(R_+^0 - K\varphi\right)\eta^3 + \left(1 + \pi(R_+^0)^2 - K\psi\right)\eta^2 + R_+^0\pi\eta + \pi = 0.$$

Dividing everything by $(R_+^0)^2$, we obtain:

$$\eta^4 + \frac{1}{(R_+^0)^2}\left(R_+^0 - K\varphi\right)\eta^3 + \frac{1}{(R_+^0)^2}\left(1 + \pi(R_+^0)^2 - K\psi\right)\eta^2 + \frac{\pi}{R_+^0}\eta + \frac{\pi}{(R_+^0)^2} = 0. \tag{32}$$

At this stage, the equation has been obtained, which should have four roots basing on algebraic reasons. We want to find out the conditions for beats occurring in the system under consideration. Beats occur when the system and an external influence have close oscillation frequencies. In this case, the imaginary parts of the roots of the equation are also close in value (we will assume they are equal to simplify the transformations). Then we assume that it is possible to represent equation (32) as the product of two polynomials of the following form:

$$\left(\eta^2 + 2\beta\eta + \omega^2\right)\left(\eta^2 + 2\alpha\eta + \omega^2\right) = 0.$$

Opening the brackets and performing algebraic transformations, we obtain:

$$\eta^4 + 2(\alpha + \beta)\eta^3 + (2\omega^2 + 4\alpha\beta)\eta^2 + 2\omega^2(\alpha + \beta)\eta + \omega^4 = 0. \tag{33}$$

Comparing the corresponding coefficients of the same powers in equations (32) and (33), we obtain a number of relations. For coefficients of free term, we obtain:

$$\omega^4 = \frac{\pi}{(R_+^0)^2}. \tag{34}$$

Also, it should be noted that when substituting the previously introduced notation (31) for $\pi = \frac{\tilde{\Omega}_0^2}{(R_+^0)^4}$ into (34), we obtain the expression for ω^2:

$$\omega^2 = \frac{\tilde{\Omega}_0}{(R_+^0)^3}. \tag{35}$$

Next, let us equate the coefficients at the first degree of η:

 https://www.doi.org/10.33910/2687-153X-2023-4-4-161-175

$$2\omega^2(\alpha+\beta)=\frac{\pi}{R_+^0}. \tag{36}$$

Let us divide (34) by (36) and express the sum of the attenuation coefficients $(\alpha+\beta)$:

$$\alpha+\beta=\frac{1}{2}\omega^2 R_+^0=\frac{1}{2}\cdot\frac{\tilde{\Omega}_0}{(R_+^0)^3}\cdot R_+^0=\frac{1}{2}\cdot\frac{\tilde{\Omega}_0}{(R_+^0)^2}. \tag{37}$$

Let us equate the coefficients at η^2:

$$2\omega^2+4\alpha\beta=\frac{1}{(R_+^0)^2}\left(1+\pi(R_+^0)^2-K\psi\right).$$

Now using algebraic transformations and substituting expressions for π (31) and ω^2 (35) and then for $K=2\gamma x^0$ and ψ (31), we obtain:

$$4\alpha\beta=\frac{1}{(R_+^0)^2}\left(1-\frac{2\tilde{\Omega}_0}{R_+^0}+\frac{\tilde{\Omega}_0^2}{(R_+^0)^2}\right)-\frac{K\psi}{(R_+^0)^2}=\frac{1}{(R_+^0)^2}\left(1-\frac{\tilde{\Omega}_0}{R_+^0}\right)^2-\frac{K\psi}{(R_+^0)^2}=$$

$$=\frac{1}{(R_+^0)^2}\left(1-\frac{\tilde{\Omega}_0}{R_+^0}\right)^2-\frac{6\gamma x^0(\varepsilon_{he}^0-2M_0)}{(R_+^0)^2}.$$

Then multiplication of coefficients α and β is equal to

$$\alpha\beta=\frac{1}{4(R_+^0)^2}\left(1-\frac{\tilde{\Omega}_0}{R_+^0}\right)^2-\frac{6\gamma x^0(\varepsilon_{he}^0-2M_0)}{4(R_+^0)^2}. \tag{38}$$

Now we have expressions for sum (37) and product (38) of α and β. The coefficients α and β can be easily determined using this system. In (Romanova 1990), a program was proposed for calculating these values.

Let us equate the coefficients at η^3:

$$\frac{1}{(R_+^0)^2}\left(R_+^0-K\varphi\right)=2(\alpha+\beta).$$

Taking into account the expression $(\alpha+\beta)$ (37) we obtain:

$$\frac{1}{(R_+^0)^2}\left(R_+^0-K\varphi\right)=2(\alpha+\beta)=\frac{\tilde{\Omega}_0}{(R_+^0)^2}$$

Then after dividing by $(R_+^0)^2$ we obtain:

$$\tilde{\Omega}_0=R_+^0-K\varphi.$$

Taking into account (31) and $K=2\gamma x^0$ we have:

$$\tilde{\Omega}_0=R_+^0-K\varphi=R_+^0-2\gamma x^0\cdot 2A\left(M_0+\frac{\varepsilon_{he}^0}{R_+^0}\right)=R_+^0-4A\gamma x^0\left(M_0+\frac{\varepsilon_{he}^0}{R_+^0}\right). \tag{39}$$

It can be shown graphically that this equation may have one solution (corresponding to one type of beating), two solutions in some cases (corresponding to two possible loads at which beating occurs), and may also have no solutions (no beating occurs).

Physical explanation for the presence of beats in a mechanical system "with one degree of freedom"

On the one hand, elastic oscillations occur in the system, on the other hand, according to the barrier model, oscillations of the occupation numbers of energy levels take place. Thus, another vibration mode arises, associated with highly elastic deformation, since highly elastic deformation is determined by the occupation numbers of the corresponding states, which obeys to vibrational relaxation. It means that the system tends to be "Boltzmann distributed", while under the influence of an external mode this process occurs in an oscillatory mode. At close frequencies the beat effect is observed.

Conclusions

1) The difference between highly oriented polymer materials and low molecular weight compounds is that they have highly elastic deformation associated with the nature of the supramolecular structure. The accepted model is the barrier theory, i. e. the presence of stable states depending on the spatial orientation of clusters of macromolecules. During the transition from one state to another a deformation quantum is released or absorbed.
2) Under the influence of an external load, the occupation numbers m_N begin to change periodically with a certain natural frequency.
3) When the frequencies of the external load and the natural frequency coincide, the beating effect is observed.
4) Thus, the hidden degree of freedom (see rheological model) is the occupation number of energy states.

Conflict of Interest

The authors declare that there is no conflict of interest, either existing or potential.

Author Contributions

All the authors discussed the final work and took part in writing the article.

References

Belousov, B. P. (1982) Periodicheski dejstvuyushchaya reaktsiya i ee mekhanizm [Intermittent reaction and its mechanism]. *Khimiya i zhizn'*, 7, 65–70. (In Russian)

Golovina, V. V., Rymkevich, P. P., Rymkevich, O. V. (2022) Effekt bienij v odnoosnoorientirovannykh polimernykh materialakh [The beating effect in uniaxial oriented polymer materials]. *Nauchno-tekhnicheskij vestnik informatsionnykh tekhnologij, mekhaniki i optiki – Scientific and Technical Journal of Information Technologies, Mechanics and Optics*, 22 (5), 999–1006. https://doi.org/10.17586/2226-1494-2022-22-5-999-1006 (In Russian)

Gorshkov, A. S. (2004) *Dinamicheskaya vyazkouprugost' sinteticheskikh nitej v nachal'noj stadii deformirovaniya [Dynamic viscoelasticity of synthetic threads in the initial stage of deformation]. PhD dissertation (Technical Sciences)*. Saint Petersburg, State University of Industrial Technologies and Design, 178 p. (In Russian)

Gorshkov, A. S., Makarov, A. G., Romanova, A. A., Rymkevich, P. P. (2013) Modelirovanie deformatsionnykh protsessov orientirovannykh polimerov na osnove opisaniya kinetiki nadmolekulyarnykh struktur, razdelennykh energeticheskimi bar'erami [Modelling of directed polymers deformation processes based on the description of the kinetics of supramolecular structures separated by energy barriers]. *Inzhenerno-stroitel'nyj zhurnal — Magazine of Civil Engineering*, 9 (44), 75–83. https://doi.org/10.5862/MCE.44.10 (In Russian)

Gorshkov, A. S., Makarov, A. G., Romanova, A. A., Rymkevich, P. P. (2015) Reologicheskiye mekhanizmy deformirovaniya oriyentirovannykh polimerov [Rheological deformation mechanisms of oriented polymers]. *Stroitel'nye materialy, oborudovanie, tekhnologii XXI veka — Construction materials, the equipment, technologies of XXI century*, 5-6 (196-197), 37–39. (In Russian)

Gorshkov, A. S., Pereborova, N. V., Vavilov, D. S. et al. (2023) Strukturno-reologicheskaya model' sinteticheskoj niti so spiral'nym uprugo-vyazkim elementom [Structural-rheological model of a synthetic thread with a spiral elastic-viscous element]. *Izvestiya vysshikh uchebnykh zavedenij. Tekhnologiya tekstil'noj promyshlennosti — The News of Higher Educational Institutions. Technology of Light Industry*, 59 (1), 60–66. (In Russian)

Gorshkov, A. S., Romanova, A. A., Rymkevich, P. P., Stalevich, A. M. (2004) Amplitudnaya modulyatsiya oriyentirovannykh polimerov v nachal'noj stadii deformirovaniya [Amplitude modulation of oriented polymers in the initial stage of deformation]. *Fiziko-khimiya polimerov: sintez, svojstva i primeneniye*, 10, 111–112. (In Russian)

Gunn, J. B. (1963) Microwave oscillations of current III-V semiconductors. *Solid State Communications*, 1 (4), 88–91. https://doi.org/10.1016/0038-1098(63)90041-3 (In English)

Makarov, A. G., Pereborova, N. V., Vagner, V. I., Vasil'eva, E. K. (2015) Computer modeling and prediction of the deformation properties of polymeric marine cables. *Fibre Chemistry*, 47(1), 51–57. https://doi.org/10.1007/s10692-015-9637-6 (In English)

Rabotnov, Yu. N. (1988) *Mekhanika deformiruemogo tverdogo tela [Mechanics of deformable solid]*. Moscow: Nauka Publ., 712 p. (In Russian)

Romanova, A. A. (1990) *Matematicheskoe modelirovanie deformatsionnykh svojstv sinteticheskikh nitej pri dinamicheskom nagruzhenii [Mathematical modeling of the deformation properties of synthetic threads under dynamic loading]. PhD dissertation (Technical Sciences)*. Saint Petersburg, Leningrad Institute of Textile and Light Industry, 231 p. (In Russian)

Romanova, A. A., Rymkevich, P. P., Gorshkov, A. S., Stalevich, A. M. (2005) Dynamic relaxation of synthetic fibres. *Fibre Chemistry*. 37 (4), 289–292. https://doi.org/10.1007/s10692-005-0097-2 (In English)

Romanova, A. A., Rymkevich, P. P., Gorshkov, A. S., Stalevich, A. M. (2007a) Relaksiruyushchij modul' Yunga sinteticheskikh nitej [Young relaxing modulus of synthetic threads]. *Izvestiya vysshikh uchebnykh zavedenij. Tekhnologiya tekstil'noj promyshlennosti — Proceedings of the Higher Educational Institutions. Textile Industry Technology*, 4 (299), 3–5. (In Russian)

Romanova, A. A., Rymkevich, P. P., Gorshkov, A. S. et al. (2007b) A new phenomenon—amplitude-modulated free oscillations (beatings) in loaded, highly oriented fibers from semicrystalline polymers. *Journal of Macromolecular Science. Part B: Physics*, 46 (3), 467–474. http://dx.doi.org/10.1080/00222340701257703 (In English)

Romanova, A. A., Rymkevich, P. P., Stalevich, A. M. (2000) Kineticheskoe opisanie relaksatsii mekhanicheskikh napryazhenij v sinteticheskikh nityakh [Kinetic description of relaxation of mechanical stresses in synthetic threads]. *Izvestiya vysshikh uchebnykh zavedenij. Tekhnologiya tekstil'noj promyshlennosti — Proceedings of the Higher Educational Institutions. Textile Industry Technology*, 1 (253), 3–7. (In Russian)

Rymkevich, P. P. (2018) *Razrabotka nauchnykh osnov i metodov prognozirovaniya termovyazkouprugikh svojstv polimernykh materialov tekstil'noj i legkoj promyshlennosti [Development of scientific foundations and methods for predicting thermoviscoelastic properties of polymer materials for textile and light industry]. PhD dissertation (Technical Sciences)*. Saint Petersburg, Saint Petersburg State University of Industrial Technologies and Design, 299 p. (In Russian)

Rymkevich, P. P., Gorshkov, A. S., Makarov, A. G., Romanova, A. A. (2014) Main constitutive equation of the viscoelastic behavior of unixially co-oriented polymers. *Fibre Chemistry*, 46 (1), 28–32. https://doi.org/10.1007/s10692-014-9555-z (In English)

Rymkevich, P. P., Gorshkov, A. S., Maksimov, V. V., Prishchepenok, O. B. (2021) Nelinejnaya reologicheskaya model' polimernykh nitej [Nonlinear rheological model of polymer filaments]. *Izvestiya vysshikh uchebnykh zavedenij. Tekhnologiya tekstil'noj promyshlennosti — Proceedings of the Higher Educational Institutions. Textile Industry Technology*, 54 (4), 15–19. (In Russian)

Stalevich, A. M., Gorshkov, A. S., Romanova, A. A., Rymkevich, P. P. (2005) *Ustrojstvo dlya opredeleniya dinamicheskikh kharakteristik polimernykh nitej metodom svobodnykh prodol'nykh kolebanij [Device for determining the dynamic characteristics of polymer threads using the method of free longitudinal vibrations]. Patent No. RU 2249195 C2*. [Online]. Available at: https://rusneb.ru/catalog/000224_000128_0002249195_20050327_C2_RU/ (accessed 10.08.2023). (In Russian)

Zhabotinskii, A. M. (1974) *Kontsentratsionnye kolebaniya [Concentration oscillations]*. Moscow: Nauka Publ., 179 p. (In Russian)

Theoretical physics.
Theory of condensed matter

UDC 538.9

EDN ZLXASG
https://www.doi.org/10.33910/2687-153X-2023-4-4-176-194

Calculations of Lyapunov exponents and characterizations of nonlinear dynamics in bulk antiferroelectrics

S.-Ch. Lim✉[1]

[1] Universiti Sains Malaysia, 11800 USM Penang, Malaysia

Author

Siew-Choo Lim, ORCID: 0000-0001-8397-0886, e-mail: sclim@usm.my

For citation: Lim, S.-Ch. (2023) Calculations of Lyapunov exponents and characterizations of nonlinear dynamics in bulk antiferroelectrics. *Physics of Complex Systems*, 4 (4), 176–194. https://www.doi.org/10.33910/2687-153X-2023-4-4-176-194 EDN ZLXASG

Received 15 July 2023; reviewed 21 September 2023; accepted 21 September 2023.

Funding: The study did not receive any external funding.

Abstract. This paper investigates the influence of the amplitude, frequency, and damping of the applied field on the maximal Lyapunov exponents and chaotic dynamics in the bulk antiferroelectric (AFE) system. Numerical simulations are conducted in three parts. First, Wolf's algorithm calculates the Lyapunov exponents with varying frequencies and a constant amplitude. The second part varies the amplitude while keeping the frequency constant. Two sets of data are generated for small ($g = 0.01$) and large ($g = 0.3$) damping values. In the third part, selected parameters produce phase portraits based on the positive and negative Lyapunov exponents using the fourth-order Runge–Kutta method. The results show that the Lyapunov exponent identifies chaotic and periodic regimes with small damping, but this becomes less evident with large damping. The study also demonstrates that manipulating the applied field parameters enables control over chaotic and periodic responses in the bulk AFE system.

Keywords: Lyapunov exponents, antiferroelectrics, ammonium dihydrogen phosphate, chaos, nonlinear, periodic response

Introduction

There are various methods to characterize the nonlinear and chaotic dynamics of physical systems. For example, one method involves plotting the power spectrum versus finite applied frequencies, where the nonlinear properties are revealed through the structures, positions, and intensities of the spectrum peaks (Dykman et al. 1988). The other methods include plotting phase portraits, Poincaré sections, and calculating the Lyapunov exponents (Baker, Gollub 1996; Goldstein et al. 2002; Marion, Thornton 1995; Strogatz 2015). In the phase portraits method, the shape of the curves and their overlap indicates the periodic responses of dynamical systems to external driving forces. Poincaré sections, on the other hand, are periodic snapshots of phase portraits, providing further insight into the behavior of nonlinear systems through the distributions and overlap of points in the 2D plots generated by these sections. The Lyapunov exponents method involves calculating the rate of exponential divergence of neighboring phase trajectories. The Lyapunov exponents greater or less than zero serve as hallmarks of chaotic or periodic responses, respectively, of the system states with respect to driving forces. Among these methods, the Lyapunov exponent is an important indicator for understanding the chaotic dynamics of physical systems. By combining these methods, a clearer picture of the dynamical responses of the system can be obtained. In this paper, we adopt a combination of methods by calculating the Lyapunov exponent and utilizing phase portraits to analyze selected parameters.

There are numerous methods available to determine the Lyapunov exponents. Some of these methods include the fast Lyapunov indicator, which computes the average of the largest Lyapunov exponent obtained from orthonormal basis tangent vectors in the phase space of the dynamical system (Lega et al. 2016). Ulam's method is used to calculate the maximal Lyapunov exponent for one-dimensional systems under small perturbations (Benettin et al. 2018). Another method involves calculating the finite size Lyapunov exponent based on averaging the finite amplitude growth rate of the dynamical physical system (Meunier, LaCasce 2021). Wolf's algorithm is employed to estimate the Lyapunov exponents for analytically defined time series model systems (Wolf et al. 1985). In this paper, we adopt Wolf's algorithm to calculate the Lyapunov exponents of bulk antiferroelectrics (AFE) (Wolf et al. 1985).

The research presented in this paper is an extension of (Lim 2022), focusing on investigating the effects of frequency, amplitude of the driving field, and damping in antiferroelectrics on the maximal Lyapunov exponents and nonlinear chaotic dynamics observed in the bulk antiferroelectric (AFE) system during its first ordered phase. The numerical simulations conducted in this study are divided into three parts. In the first two parts, Wolf's algorithm is utilized to calculate the Lyapunov exponents of the bulk AFE system. The first part involves varying the frequency of the applied field while keeping the amplitude constant. The second part focuses on varying the amplitude of the applied field while keeping the frequency constant. For each set of the selected amplitude and frequency of the applied field, two sets of numerical data are generated to account for different damping conditions. Specifically, one set corresponds to a small damping value of $g = 0.01$, and the other set corresponds to a large damping value of $g = 0.3$.

In the third part, a few sets of parameters are selected from the first two parts, corresponding to positive and negative values of the Lyapunov exponents, which are then used to generate the corresponding phase portraits. The method employed in the third part closely resembles that of (Lim 2022), where numerical simulations are conducted using the fourth-order Runge-Kutta method for a specific material, such as ammonium dihydrogen phosphate (ADP). In contrast to the approach in (Lim 2022), where the chaotic dynamics are explored through the generation of numerous phase portraits, we utilize the Lyapunov exponent as an indicator to distinguish between chaotic (positive) and periodic (negative) regimes.

Formalism for nonlinear dynamics

The details of the formalism can be found in (Lim 2022). The focus of the studies here is an extension of (Lim 2022), where we adopt Lim's dimensionless AFE oscillatory equations of motion, as shown in equations (1):

$$\frac{d^2q}{dt^2} + g\frac{dq}{dt} = -2(\psi+\tau)q + 4\left(q^3 + 3qr^2\right) - 6\left(q^5 + 10q^3r^2 + 5qr^4\right) + e_0\sin(2\pi ft), \tag{1a}$$

$$\frac{d^2r}{dt^2} + g\frac{dr}{dt} = -2\tau r + 4\left(3q^2r + r^3\right) - 6\left(5q^4r + 10q^2r^3 + r^5\right). \tag{1b}$$

The symbols τ, e ($\equiv e_0\sin(2\pi ft)$), q, r, ψ, t, and g represent the reduced or dimensionless temperature, applied Maxwell field, normal displacement, staggered displacement, interaction constant of sublattices, time, and damping, respectively. From equations (1), we choose e and g as the control parameters of the system for numerical simulations. In this paper, we fix the values of τ to be approximately -3.346457×10^{-3} and ψ to be approximately 1.2332677×10^{-2} as in (Lim 2022). The selected damping constants are 0.01 and 0.3.

Equations (1) are nonautonomous differential equations due to the explicit time dependence. In order to perform numerical simulations using Wolf's algorithm, these equations are transformed into autonomous differential equations (Baker, Gollub 1996; Boyce, DiPrima 2001) by introducing the following substitutions:

$$x_1 = q, \quad x_2 = r, \quad x_3 = 2\pi ft, \quad x_4 = \frac{dx_1}{dt} = \frac{dq}{dt}, \quad x_5 = \frac{dx_2}{dt} = \frac{dr}{dt}, \tag{2a}$$

$$x_6 = \frac{dx_3}{dt} = 2\pi f.$$

This yields six coupled first-order differential equations:

$$\frac{dx_1}{dt} = \frac{dq}{dt} = x_4, \tag{2b}$$

$$\frac{dx_2}{dt} = \frac{dr}{dt} = x_5, \tag{2c}$$

$$\frac{dx_3}{dt} = x_6 = 2\pi f, \tag{2d}$$

$$\begin{aligned}\frac{dx_4}{dt} &= -gx_4 - 2(\psi + \tau)x_1 + 4\left(x_1^3 + 3x_1x_2^2\right) \\ &\quad - 6\left(x_1^5 + 10x_1^3x_2^2 + 5x_1x_2^4\right) + e_0 \sin(x_3),\end{aligned} \tag{2e}$$

$$\begin{aligned}\frac{dx_5}{dt} &= -gx_5 - 2\tau x_2 + 4\left(3x_1^2x_2 + x_2^3\right) \\ &\quad - 6\left(5x_1^4x_2 + 10x_1^2x_2^3 + x_2^5\right),\end{aligned} \tag{2f}$$

$$\frac{dx_6}{dt} = 0. \tag{2g}$$

Numerical simulations

In the numerical simulations, we adopt the AFE's natural frequency, f_0, to be approximately 0.021336524, and the coercive field of the system, e_C, to be approximately 0.41658, as stated in (Lim 2022). The numerical simulations are divided into three parts. The first part is the Lyapunov exponents, λ_q, versus the frequency, f, of the applied field. The second part is the Lyapunov exponents, λ_q, versus the amplitude of the applied field, e_0. In the third part, we investigate the relations between the Lyapunov exponents and the AFE order parameter responses based on a few selected sets of parameters. The selections of these parameters are mainly based on the results obtained in the first and second parts. To eliminate transient effects, the first 30 cycles are excluded when generating the numerical data. The Lyapunov exponents in the first and second parts are obtained from the 31st to the 200th cycles.

Lyapunov exponents versus frequency of the applied field

The first part involves calculating the Lyapunov exponents, λ_q, of the AFE by varying the frequency f, while keeping the amplitude, e_0, and damping constant, g, fixed at certain values. Wolf's algorithm is utilized to compute the four Lyapunov exponents for q, dq/dt, r, and dr/dt, corresponding to x_1, x_4, x_2, and x_5 in equations (2). Only the largest Lyapunov exponents, λ_q, corresponding to q or x_1 are plotted in 2D graphs. In the calculations, for each selected fixed e_0 value, two curves are generated: one with a small damping constant, g = 0.01, and another with a large damping constant, g = 0.3. The numerical curves for λ_q versus f, with e_0 fixed at $0.01e_C$ and $0.9e_C$, are plotted in Figure 1, while the curves e_0 fixed at $2.0e_C$ are plotted in Figure 2. Furthermore, the curves with e_0 fixed at $249e_C$ are plotted in Figure 3. In Figures 1 and 2, the frequency, f, varies from $0.025\,f_0$ to $10.0\,f_0$, while in Figure 3, the frequency, f, varies from $0.25\,f_0$ to $100.0\,f_0$.

 https://www.doi.org/10.33910/2687-153X-2023-4-4-176-194

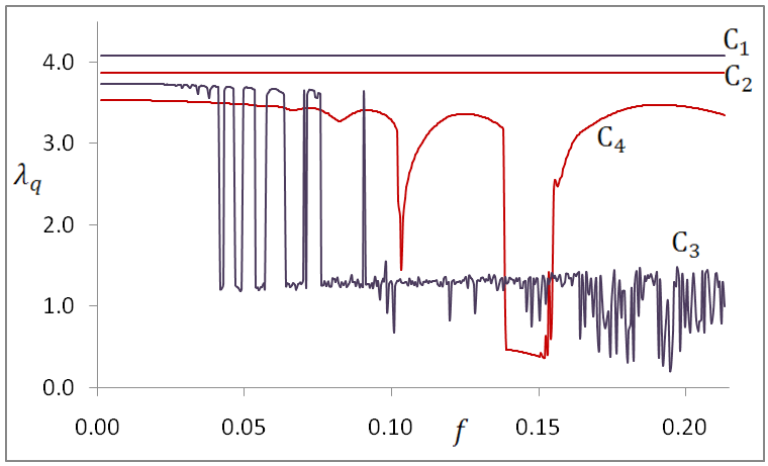

Fig. 1. λ_q versus f for $e_0 < e_C$. C_1 ($e_0 = 0.01e_C$, $g = 0.01$), C_2 ($e_0 = 0.01e_C$, $g = 0.3$); C_3 ($e_0 = 0.9e_C$, $g = 0.01$), C_4 ($e_0 = 0.9e_C$, $g = 0.3$)

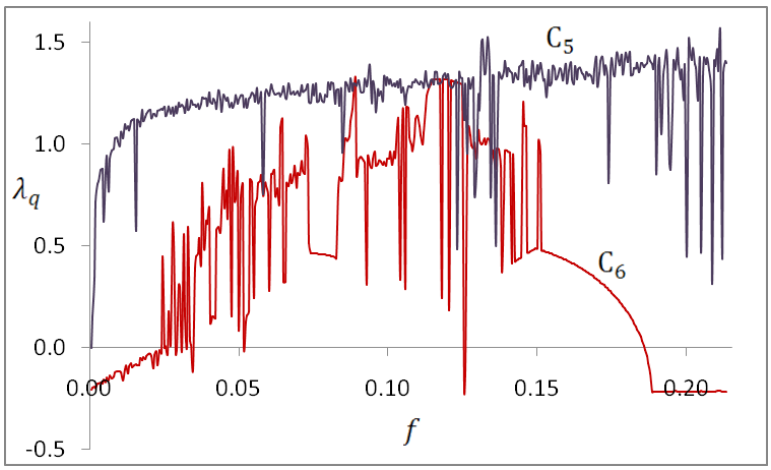

Fig. 2. λ_q versus frequency f for $e_0 > e_C$. C_5 ($e_0 = 2.0e_C$, $g = 0.01$), C_6 ($e_0 = 2.0e_C$, $g = 0.3$)

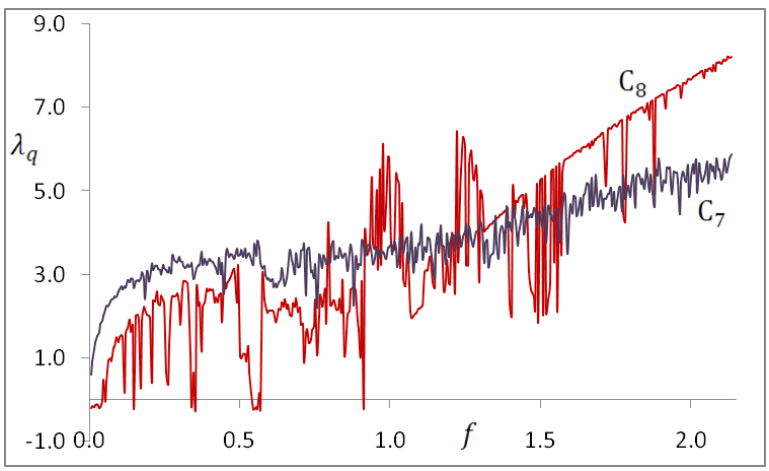

Fig. 3. λ_q versus f for $e_0 = 249e_C$. C_7 ($g = 0.01$), C_8 ($g = 0.3$)

The Lyapunov exponents, λ_q, versus frequency f with the amplitude fixed at $e_0 = 0.01e_C$, are represented by curves C_1 for $g = 0.01$ and C_2 for $g = 0.3$, as shown in Figure 1. The frequency, f, varies from $0.025\,f_0$ to $10.0\,f_0$. The curves C_1 and C_2 remain relatively at around 4.074 and 3.87, respectively, as the frequency varies. However, the numerical data for C_1 and C_2 exhibit slight fluctuations within the ranges [4.073846, 4.074086] and [3.870382, 3.870610], respectively. These small fluctuations disappear when C_1 and C_2 are plotted in the same graph. Generally, C_1 is approximately 0.204 higher than C_2.

The Lyapunov exponents, λ_q, versus frequency, f, with the amplitude fixed at $e_0 = 0.9e_C$, are represented by curves C_3 for $g = 0.01$ and C_4 for $g = 0.3$, as shown in Figure 1. In the frequency range $f \in [0.025f_0, 1.925f_0]$, curve C_3 is greater than C_4, and both curves have small fluctuations. For frequencies in the range $f \in [1.925f_0, 3.55f_0]$, curve C_3 demonstrates larger fluctuations within the range [3.6960336,1.2019837]. For frequencies greater than $3.55f_0$, curve C_4 exceeds C_3, except for the range $f \in [6.5f_0, 7.25f_0]$.

The Lyapunov exponents, λ_q, versus frequency f with the amplitude fixed at $e_0 = 2.0e_C$, are represented by curves C_5 for $g = 0.01$ and C_6 for $g = 0.3$, as shown in Figure 2. The frequency, f, varies from $0.025\,f_0$ to $10.0\,f_0$. In general, curve C_5 is greater than C_6, and both curves exhibit fluctuations throughout the entire range of the graph, i. e., $f \in [0.025f_0, 10.0f_0]$. For curve C_5, the first data point of λ_q is negative at $f = 0.025f_0$, while the remaining points are positive. Curve C_6, on the other hand, exhibits periodic windows, with notable ones occurring at $f \in [0.025f_0, 1.125f_0]$, $f \in [5.875f_0, 5.9f_0]$, and $f \in [8.725f_0, 10.0f_0]$.

The Lyapunov exponents, λ_q, versus frequency, f, with amplitude fixed at a large value, i. e., $e_0 = 249.0e_C$, are represented by curves C_7 for $g = 0.01$ and C_8 for $g = 0.3$, as shown in Figure 3. The frequency, f, varies from $0.25\,f_0$ to $100.0\,f_0$. In general, curve C_7 is higher than C_8 within the range $f \in [0.25f_0, 43.5f_0]$. Curve C_8 exhibits prominent fluctuation features in the range $f \in [43.5f_0, 7.375f_0]$. For frequencies greater than $7.375f_0$, curve C_8 tends to be higher than C_7, and demonstrates a trend of linear increment with respect to e_0. Curve C_7 does not exhibit periodic windows, while curve C_8 exhibits periodic windows.

By comparing curves C_1 to C_8 in Figures 1 to 3, we observe that the Lyapunov exponents, λ_q, for $g = 0.01$ are generally greater than those for $g = 0.3$, particularly for small e_0 and f values. Most of the periodic windows, where $\lambda_q < 0$, are present in the curves associated with the larger damping constant, $g = 0.3$, namely C_6 and C_8.

Lyapunov exponents versus amplitude of the applied field

In the second part, we use the same Wolf's algorithm as in the first part to compute the Lyapunov exponents for the AFE system by varying the amplitude of the applied field, e_0, while keeping its frequency, f, fixed at several values. The calculated values of λ_q are shown in Figures 4 and 5. For each selected fixed f value, two curves are generated: one with a small damping constant, $g = 0.01$, and another one with a large damping constant, $g = 0.3$.

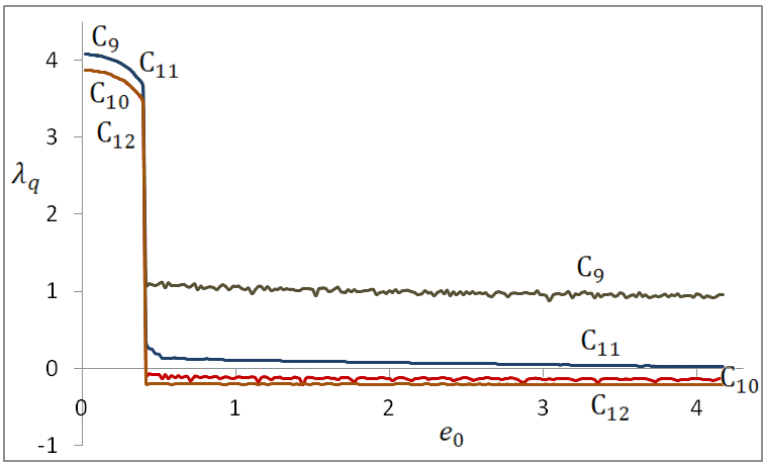

Fig. 4. λ_q versus e_0 for $f < f_0$. C_9 ($f = 0.5f_0$, $g = 0.01$), C_{10} ($f = 0.5f_0$, $g = 0.3$), C_{11} ($f = 0.04f_0$, $g = 0.01$), C_{12} ($f = 0.04f_0$, $g = 0.3$)

 https://www.doi.org/10.33910/2687-153X-2023-4-4-176-194

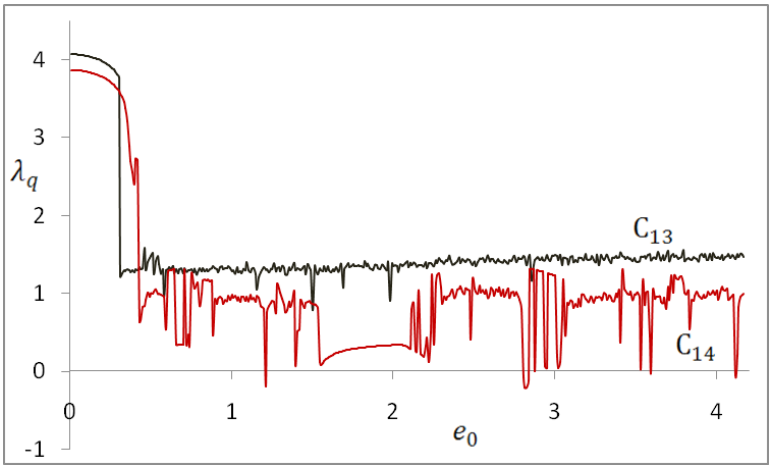

Fig. 5. λ_q versus e_0 for $f > f_0$. C_{13} ($f = 5.0\,f_0$, $g = 0.01$), C_{14} ($f = 5.0\,f_0$, $g = 0.3$)

The Lyapunov exponents, λ_q, versus amplitude, e_0, with the frequency fixed at $f = 0.5\,f_0$, are represented by curves C_9 for $g = 0.01$ and C_{10} for $g = 0.3$ in Figure 4. Additionally, the λ_q values with the frequency fixed at $f = 0.04f_0$ are represented by curves C_{11} for $g = 0.01$ and C_{12} for $g = 0.3$, as shown in Figure 4. The amplitude, e_0, varies from $0.025e_C$ to $10.0e_C$. In Figure 4, all curves exhibit discontinuities near the value of e_C, approximately 0.41658. At this point, λ_q decreases discontinuously from higher to lower values as e_0 transitions through e_C from low to high values. The curves associated with smaller damping constants are generally higher than those with larger damping. Specifically, curve C_9 is greater than C_{10}, and C_{11} is greater than C_{12}. When $e_0 > e_C$, all curves exhibit small fluctuations around nearly horizontal lines, and C_{10} and C_{12} showing negative values.

The Lyapunov exponents, λ_q, versus amplitude, e_0, with the frequency fixed at $f = 5.0f_0$, are represented by curves C_{13} for $g = 0.01$ and C_{14} for $g = 0.3$, as shown in Figure 5. The amplitude, e_0, varies from $0.025e_C$ to $10.0e_C$. In Figure 5, both C_{13} and C_{14} exhibit a discontinuity near the value of e_C, approximately 0.41658. However, the discontinuity in C_{14} is less severe and exhibits a rounded structure as e_0 transitions through e_C from low to high values. The curves associated with smaller damping constants are generally higher than those with larger damping constants. Specifically, curve C_{13} is greater than C_{14}. When $e_0 > e_C$, curve C_{13} exhibits small fluctuations around nearly horizontal lines. In contrast, curve C_{14} exhibits larger fluctuations, including a few periodic windows corresponding to the parts of C_{14} located below the horizontal axis.

Order parameter responses in bulk AFE

The third part is based on the results obtained from the first two parts. A few sets of values for f and e_0 are chosen to generate the phase portraits of the AFE system using the fourth-order Runge-Kutta method, following the approach outlined in (Lim 2022). The selection of f and e_0 values is made with the aim of observing the relations between λ_q and the responses of the AFE to the applied electric field. For the purpose of comparison, two sets of numerical data are generated for each selected f and e_0 combination: one set corresponds to a small damping value of $g = 0.01$, and the other set corresponds to a large damping value of $g = 0.3$.

The calculated data for each set of f, e_0, and g values are plotted in four figures. (a) shows the plot of the dimensionless applied sinusoidal electric field, e, and the dimensionless normal displacement, q, as functions of dimensionless time, t. (b) shows hysteresis features, i. e., the dimensionless normal displacement, q, versus the dimensionless applied electric field, e. (c) shows the phase portrait of the system, namely, the time derivative of the dimensionless normal displacement, dq/dt, versus the dimensionless normal displacement, q. Lastly, (d) exhibits the states of the AFE system in the dimensionless phase space plotted against dimensionless time, t, in a three-dimensional curve. The duration for the numerical results shown in (a) to (d) is four cycles, specifically from the 31st to the 34th cycles.

For $e_0 = 1.0 \times 10^{-12}$ $e_C = 4.1658 \times 10^{-13}$ and $f = 4.0 \times 10^{-3}$ $f_0 \approx 8.5346 \times 10^{-5}$, the AFE responses are shown in Figure 6(a) to 6(d). The curves corresponding to the damping constant g, equalling 0.01 and 0.3, overlap with a difference of approximately 2% between the two sets of numerical data. The maximal

Lyapunov exponent for the g = 0.3 case is positive, approximately 3.58144. However, the computation of λ_q for the g = 0.01 case encounters numerical simulation overflow, preventing its generation. The responses of the AFE exhibit characteristics close to periodic responses. This can be observed in Figure 6(a), where the curves resemble sinusoidal curves and are in phase with e. Furthermore, the curves in the four cycles overlap, resulting in a linear line through the origin in Figure 6(b) and an elliptical shape in the phase portrait shown in Figure 6(c). For a particular set of e_0 and f values, the magnitude of the order parameter response is proportional to the area occupied by the corresponding phase portrait, or the volume V_q in (dq/dt, q) in phase space. The area occupied by the ellipse in Figure 6(c) is estimated as $V_q \approx 1.025 \times 10^{-29}$, which is extremely small due to the smallness of the applied e_0 and f values. The smooth curve in Figure 6(d) further elaborates the elliptical phase portrait shown in Figure 6(c).

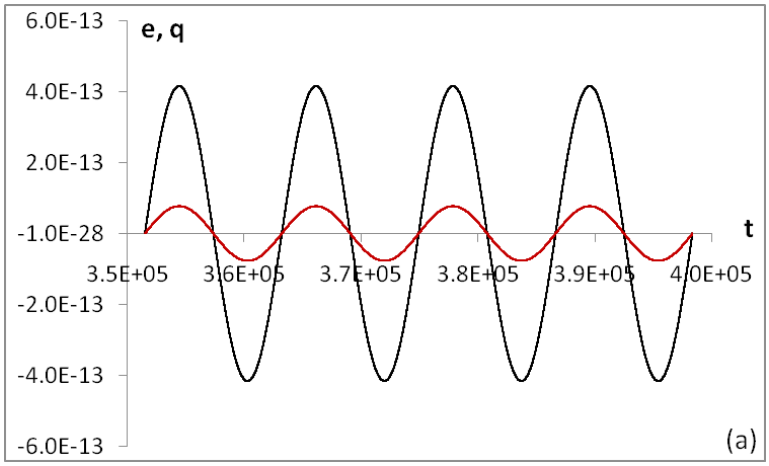

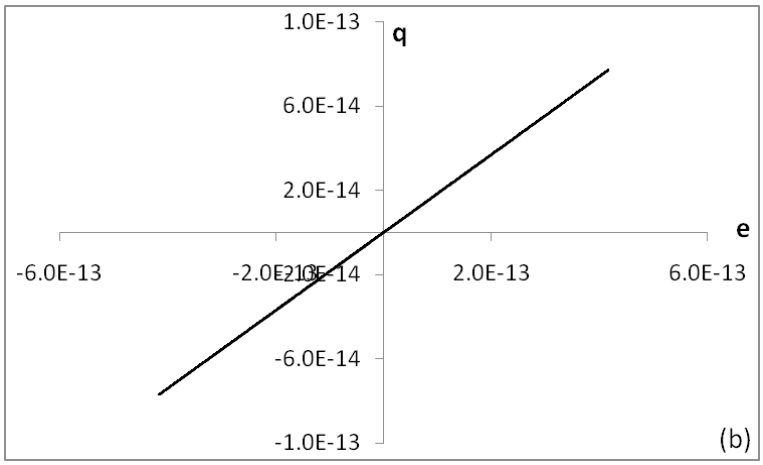

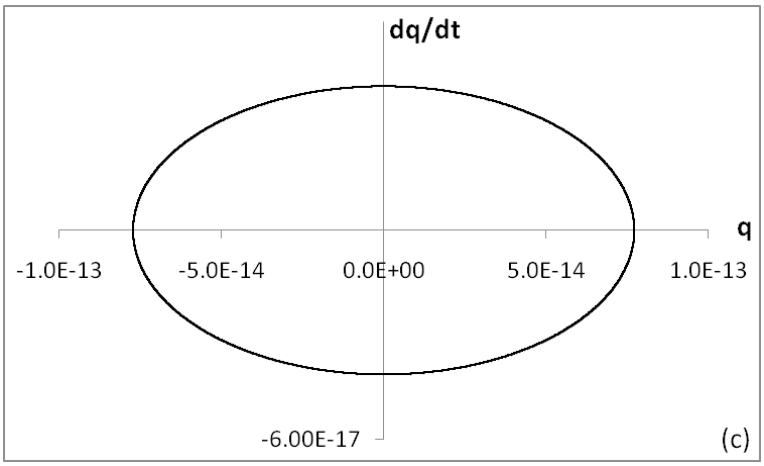

 https://www.doi.org/10.33910/2687-153X-2023-4-4-176-194

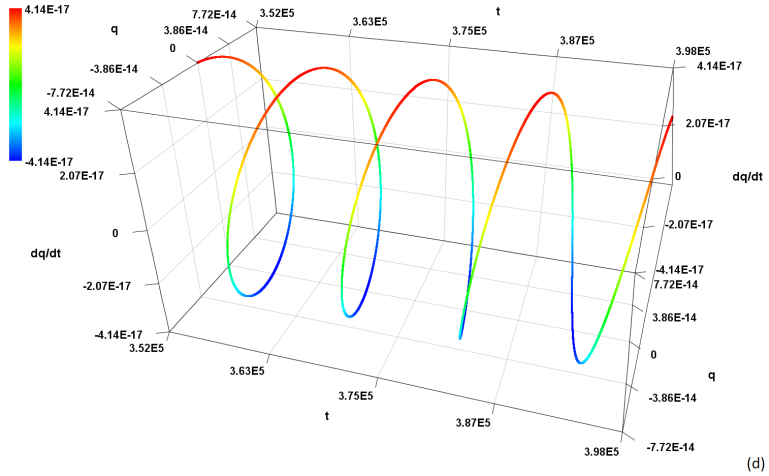

Fig. 6. AFE response for $f = 4.0 \times 10^{-3} f_0$, $e_0 = 1.0 \times 10^{-12} e_C$, $g = 0.3$ and 0.01. (a) e and q versus t, where e is represented by the black curve and q is represented by the red curve. (b) q versus e. (c) dq/dt versus q. (d) dq/dt versus q versus t.

For $e_0 = 0.9 e_C \approx 0.374922$, $f = 2.275\, f_0 \approx 0.048541$, and $g = 0.3$, the AFE responses are shown in Figure 7(a) to 7(d). The maximal Lyapunov exponent is positive and approximately 3.477528. In Figure 7(a), the curves of e and q exhibit a slight phase difference. The q curve shows wavy deviation on triangular waves. The hysteresis loops and corresponding phase portraits for four cycles of e overlap, as depicted in Figures 7(b) and 7(c). Figure 7(c) shows that the AFE responses occupy a small volume in phase space, estimated at $V_q \approx 0.0105$. The wavy pattern observed in each cycle of the curve in Figure 7(d) further elaborates the non-elliptic irregular wavy cloud shape of the phase portrait shown in Figure 7(c).

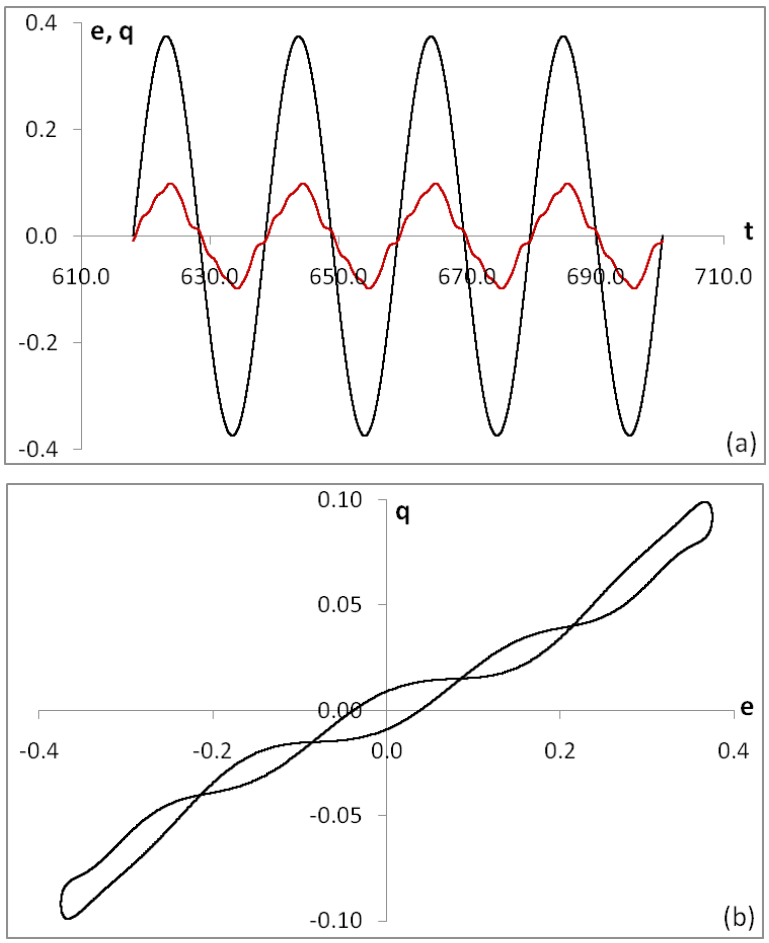

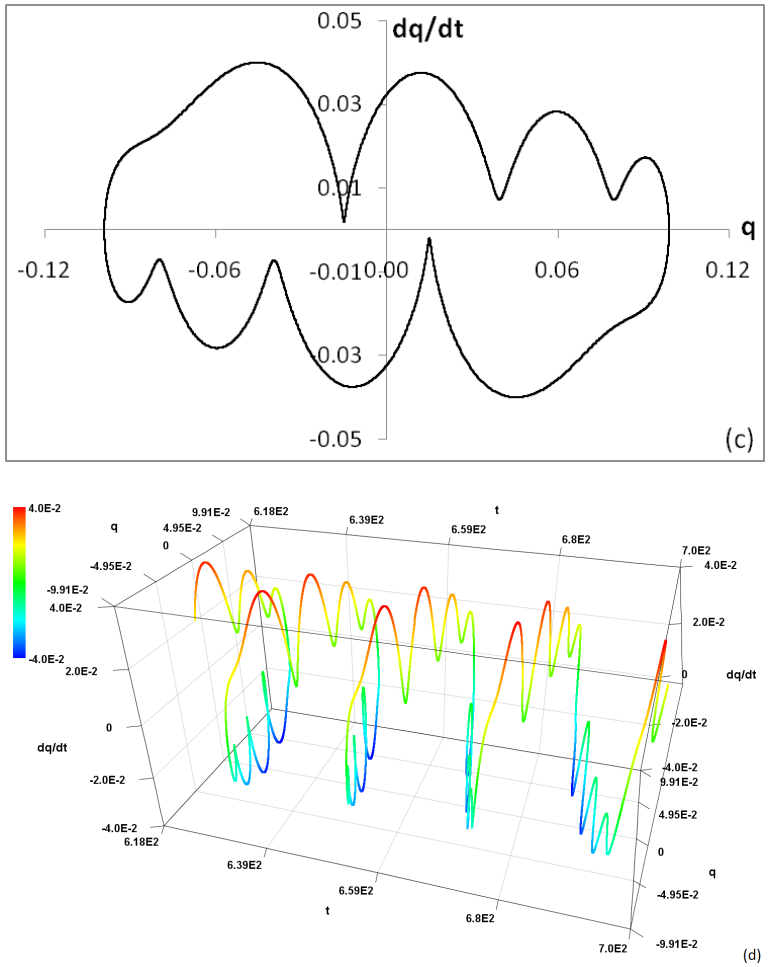

Fig. 7. AFE response for $f = 2.275f_0$, $e_0 = 0.9e_C$, $g = 0.3$. $\lambda_q = 3.4775278$. (a) e and q versus t, where e is represented by the black curve and q is represented by the red curve. (b) q versus e. (c) dq/dt versus q. (d) dq/dt versus q versus t.

For $e_0 = 0.9e_C \approx 0.374922$, $f = 2.275f_0 \approx 0.048541$, and $g = 0.01$, the AFE responses are shown in Figure 8(a) to 8(d). The maximal Lyapunov exponent is positive and approximately 1.185748. In Figure 8(a), e and q exhibit a slight phase difference. The pattern of the q curve shows an irregular wavy pattern on each cycle, indicating non-periodic behaviour. The hysteresis loops and corresponding phase portraits for four cycles of e do not overlap, as shown in Figures 8(b) and 8(c). Figure 8(c) shows that the responses of AFE occupy a volume $V_q \approx 2.44$ in phase space, which is about 232 times larger compared to the volume in Figure 7(c). The presence of additional irregular loops winding around the attractors on both sides in each cycle depicted in Figure 8(d) further elaborates the irregular and non-overlap dumbbell shapes of the phase portrait displayed in Figure 8(c).

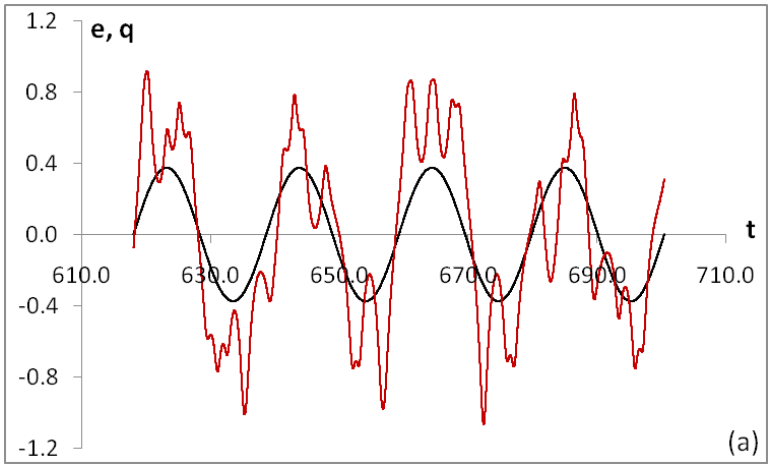

 https://www.doi.org/10.33910/2687-153X-2023-4-4-176-194

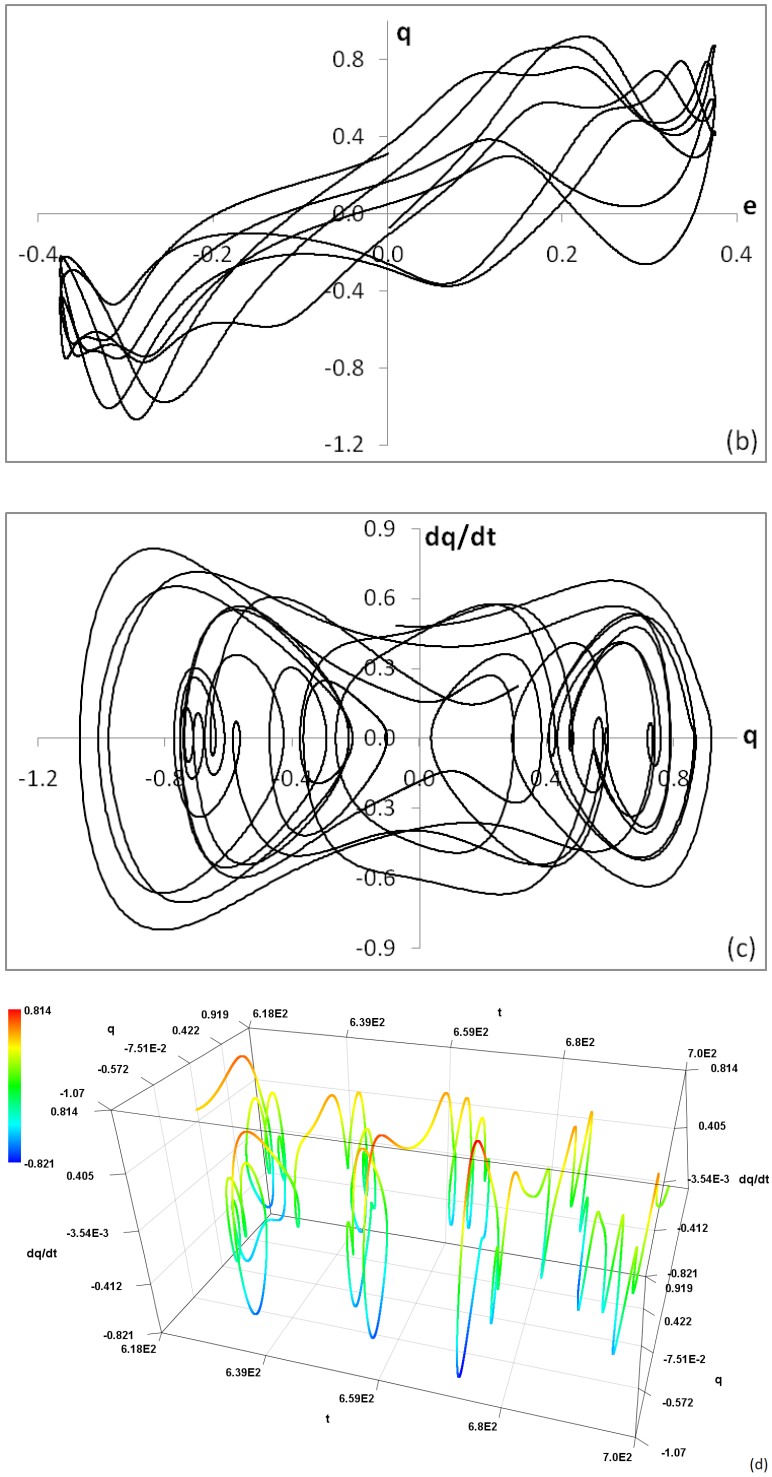

Fig. 8. AFE response for $f = 2.275 f_0$, $e_0 = 0.9 e_C$, $g = 0.01$, and $\lambda_q = 1.185748$. (a) e and q versus t, where e is represented by the black curve and q is represented by the red curve. (b) q versus e. (c) dq/dt versus q. (d) dq/dt versus q versus t.

For $e_0 = 0.9 e_C \approx 0.374922$, $f = 7.05\, f_0 \approx 0.150422$, and $g = 0.3$, the AFE responses are shown in Figure 9(a) to 9(d). The maximal Lyapunov exponent is positive and approximately 0.380776. In Figure 9(a), e and q are out of phase, with q leading e nearly $\pi/4$. The pattern of the q curve exhibits slightly distorted triangular waves. The hysteresis loops and corresponding portraits for four cycles of e overlap, as shown in Figures 9(b) and 9(c). Figure 9(c) demonstrates that the responses of the AFE occupy a volume $V_q \approx 3.22$ in phase space. The pattern observed in each cycle of the curve in Figure 9(d) further elaborates the dumbbell shape of the phase portrait displayed in Figure 9(c).

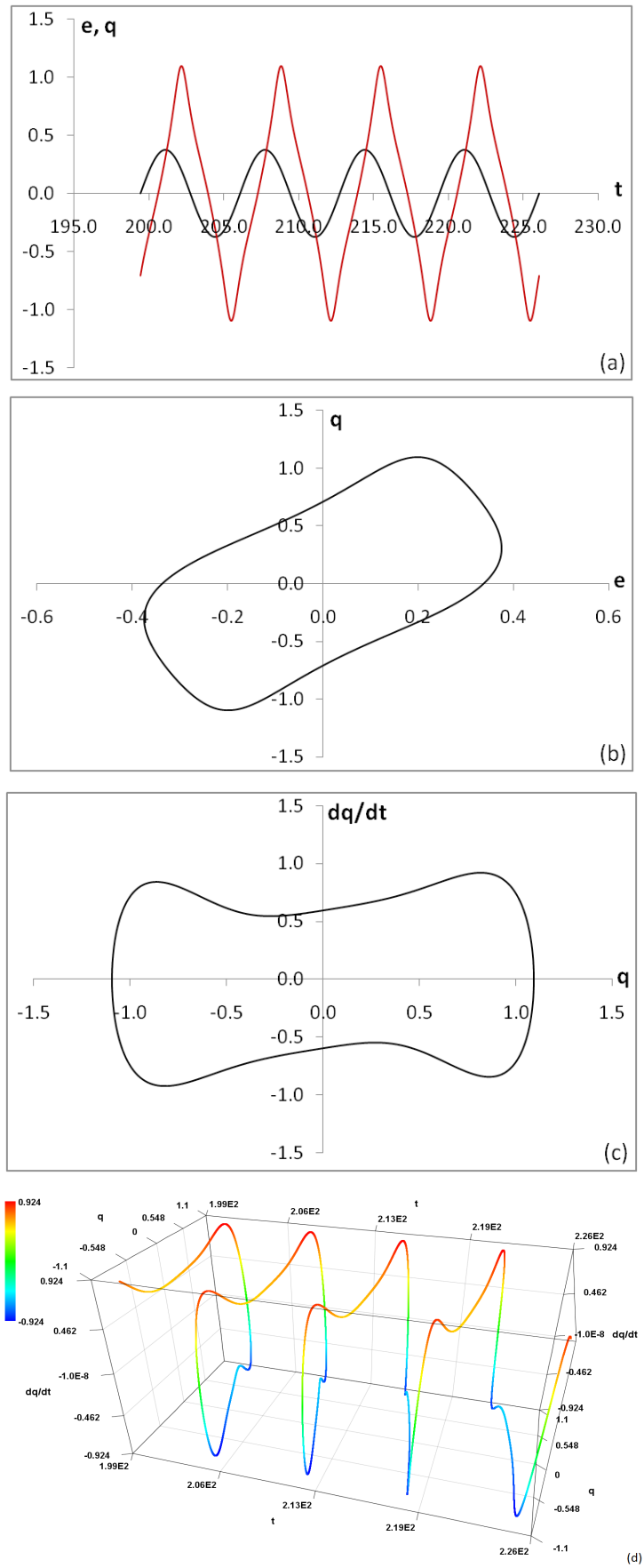

Fig. 9. AFE response for $f = 7.05f_0$, $e_0 = 0.9e_C$, $g = 0.3$, and $\lambda_q = 0.3807764$. (a) e and q versus t, where e is represented by the black curve and q is represented by the red curve. (b) q versus e. (c) dq/dt versus q. (d) dq/dt versus q versus t.

 https://www.doi.org/10.33910/2687-153X-2023-4-4-176-194

For $e_0 = 0.9e_C \approx 0.374922$, $f = 7.05f_0 \approx 0.150422$, and $g = 0.01$, the AFE responses are shown in Figure 10(a) to 10(d). The maximal Lyapunov exponent is positive and approximately 0.826725. In Figure 10(a), e and q are out of phase. The pattern of the q curve shows an irregular wavy pattern on each cycle, indicating non-periodic behaviour. The hysteresis loops and corresponding phase portraits for four cycles of e do not overlap as shown in Figures 10(b) and 10(c). Figure 10(c) shows that the responses of AFE occupy a volume $V_q \approx 2.92$ in phase space, which is slightly smaller than the one shown in Figure 9(c). The irregular wavy curve in Figure 10(d) further elaborates the irregular shape of the phase portrait displayed in Figure 10(c).

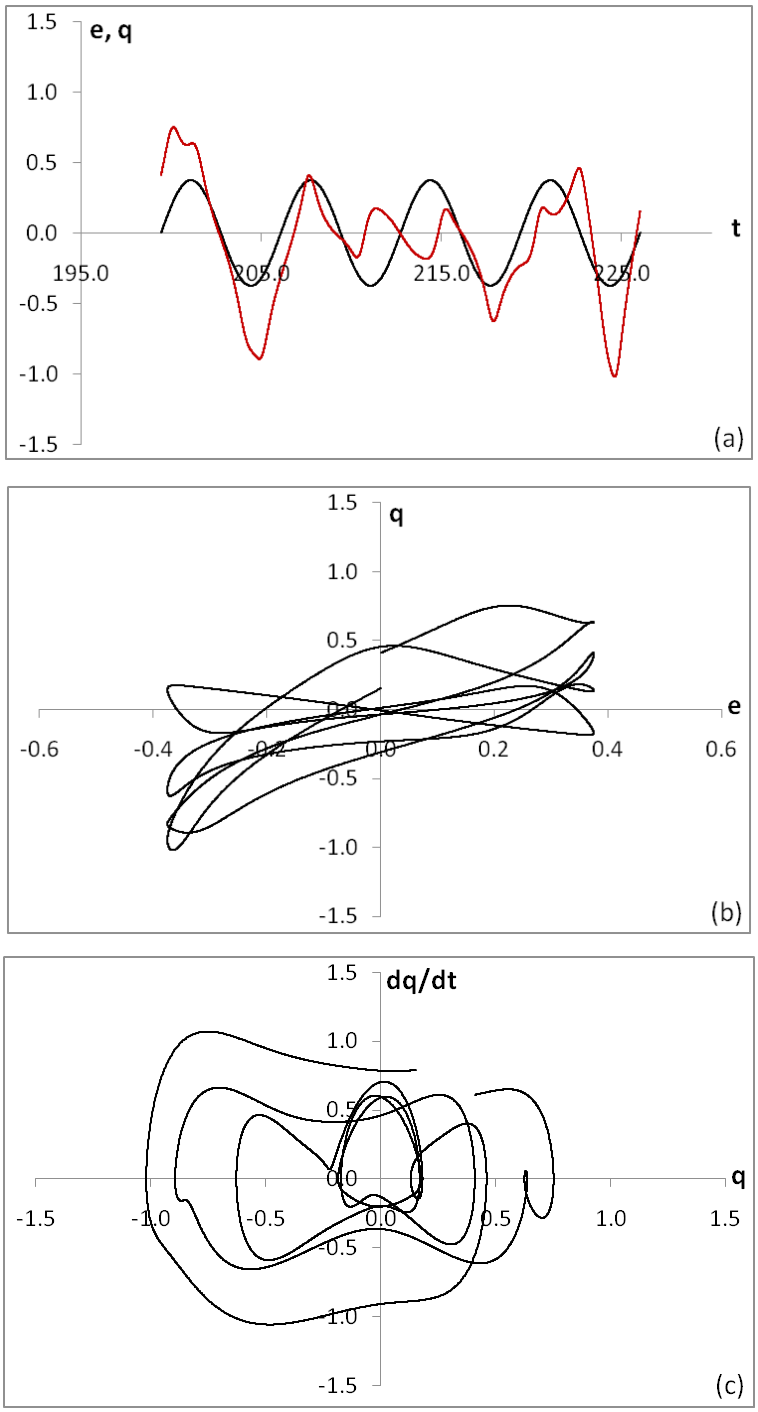

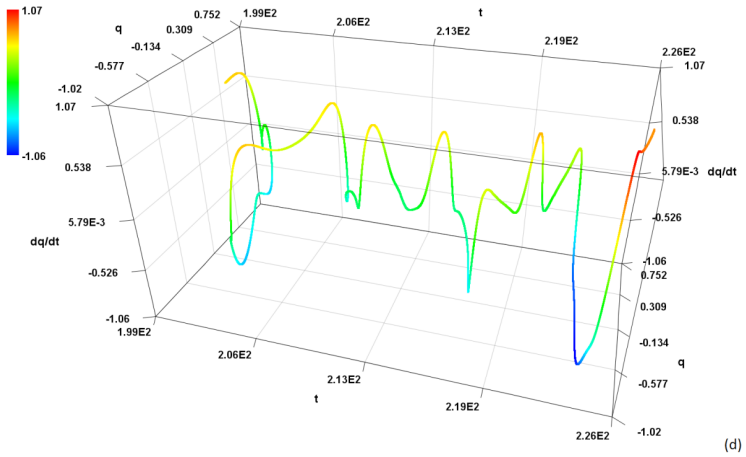

Fig. 10. AFE response for $f = 7.05f_0$, $e_0 = 0.9e_C$, $g = 0.01$, and $\lambda_q = 0.82672474$. (a) e and q versus t, where e is represented by the black curve and q is represented by the red curve. (b) q versus e. (c) dq/dt versus q. (d) dq/dt versus q versus t.

For $e_0 = 2.0e_C \approx 0.83316$, $f = 0.025\, f_0 \approx 5.334131 \times 10^{-4}$, and $g = 0.3$, the AFE responses are shown in Figures 11(a) to 11(d). The maximal Lyapunov exponent is negative and approximately –0.207926. In Figure 11(a), e and q are out of phase. The q wave exhibits branching spikes on the first and third quadrant edges of every cycle, indicating periodic behaviour. The hysteresis loops and corresponding phase portraits for four cycles of e overlap, as shown in Figures 11(b) and 11(c). Figure 11(c) exhibits inward spiral curves towards the attractors located at both sides, corresponding to $q \approx \pm 0.89$. The responses of the AFE occupy a volume $V_q \approx 2.71$ in phase space. The anti-symmetric dumbbell-shaped 4-cycle curve spiraling towards the attractors on both sides for each cycle depicted in Figure 11(d) further elaborates on the pattern observed in the phase portrait displayed in Figure 11(c).

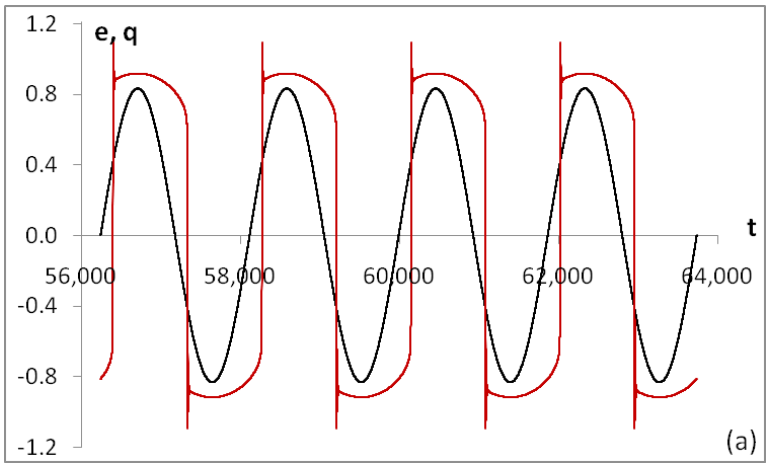

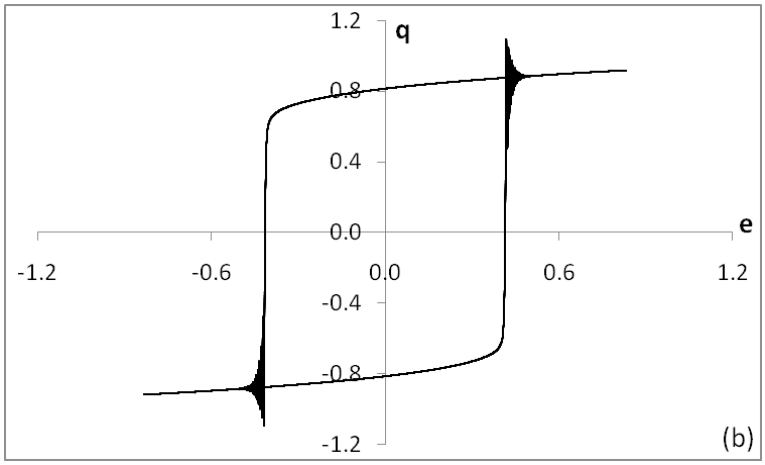

https://www.doi.org/10.33910/2687-153X-2023-4-4-176-194

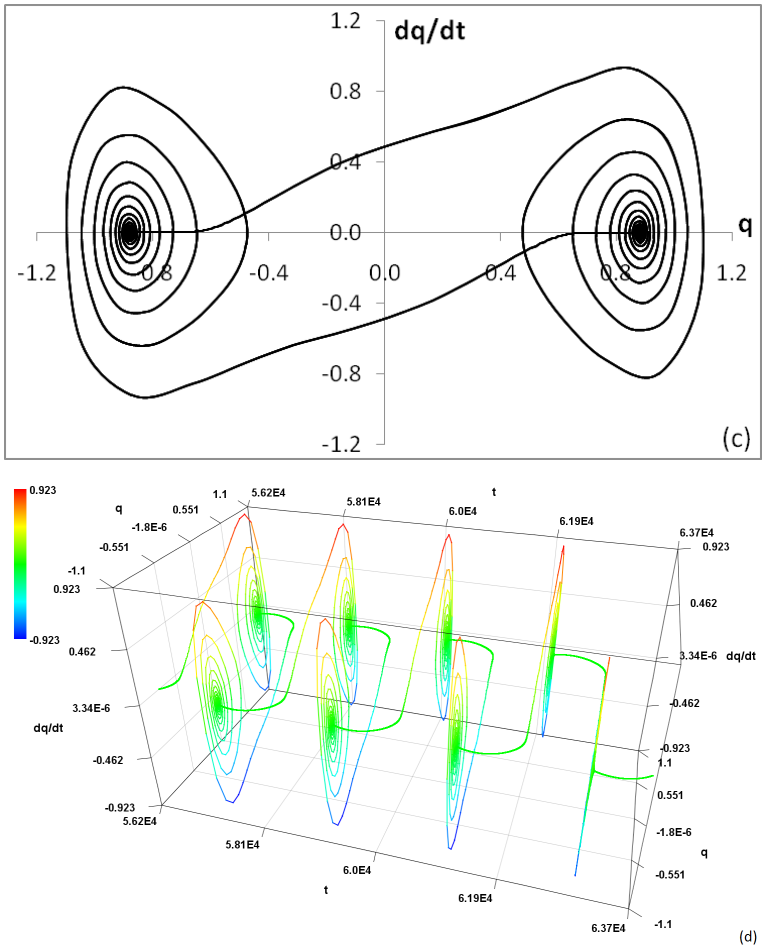

Fig. 11. AFE response for $f = 0.025 f_0$, $e_0 = 2.0e_C$, $g = 0.3$, and $\lambda_q = -0.20792619$. (a) e and q versus t, where e is represented by the black curve and q is represented by the red curve. (b) q versus e. (c) dq/dt versus q. (d) dq/dt versus q versus t.

For $e_0 = 2.0e_C \approx 0.83316$, $f = 0.025 f_0 \approx 5.334131 \times 10^{-4}$, and $g = 0.01$, the AFE responses are shown in Figure 12(a) to 12(d). The maximal Lyapunov exponent is negative and approximately −0.00414195. In Figure 12(a), e and q are out of phase. The q wave exhibits intense branching oscillations damped towards the peaks of the first and third quadrant of every cycle, indicating periodic behaviour. The hysteresis loops and corresponding phase portraits for four cycles of e overlap, as shown in Figures 12(b) and 12(c). Figure 12(c) illustrates intense inward spiral curves towards the attractors located at both sides, corresponding to $q \approx \pm 0.89$, The responses of the AFE occupy a volume $V_q \approx 4.12$ in phase space, which is approximately 1.52 times larger than the one shown in Figure 11(c). The anti-symmetric dumbbell-shape 4-cycles curve, spiraling towards the attractors on both sides for each cycle in Figure 12(d), further elaborates on the pattern observed in the phase portrait displayed in Figure 12(c).

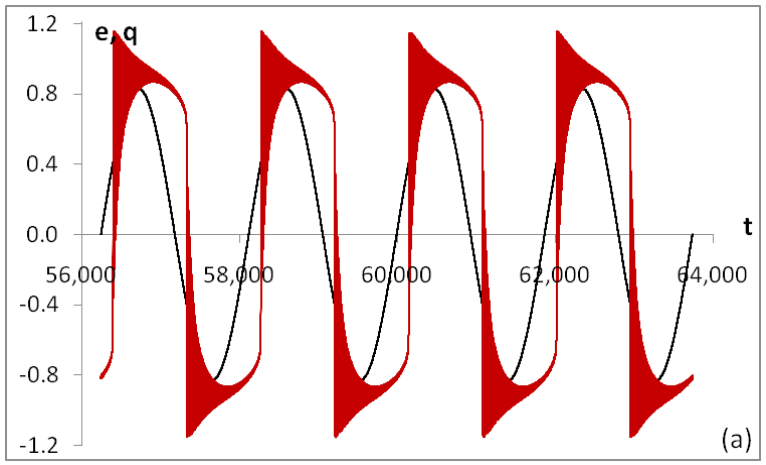

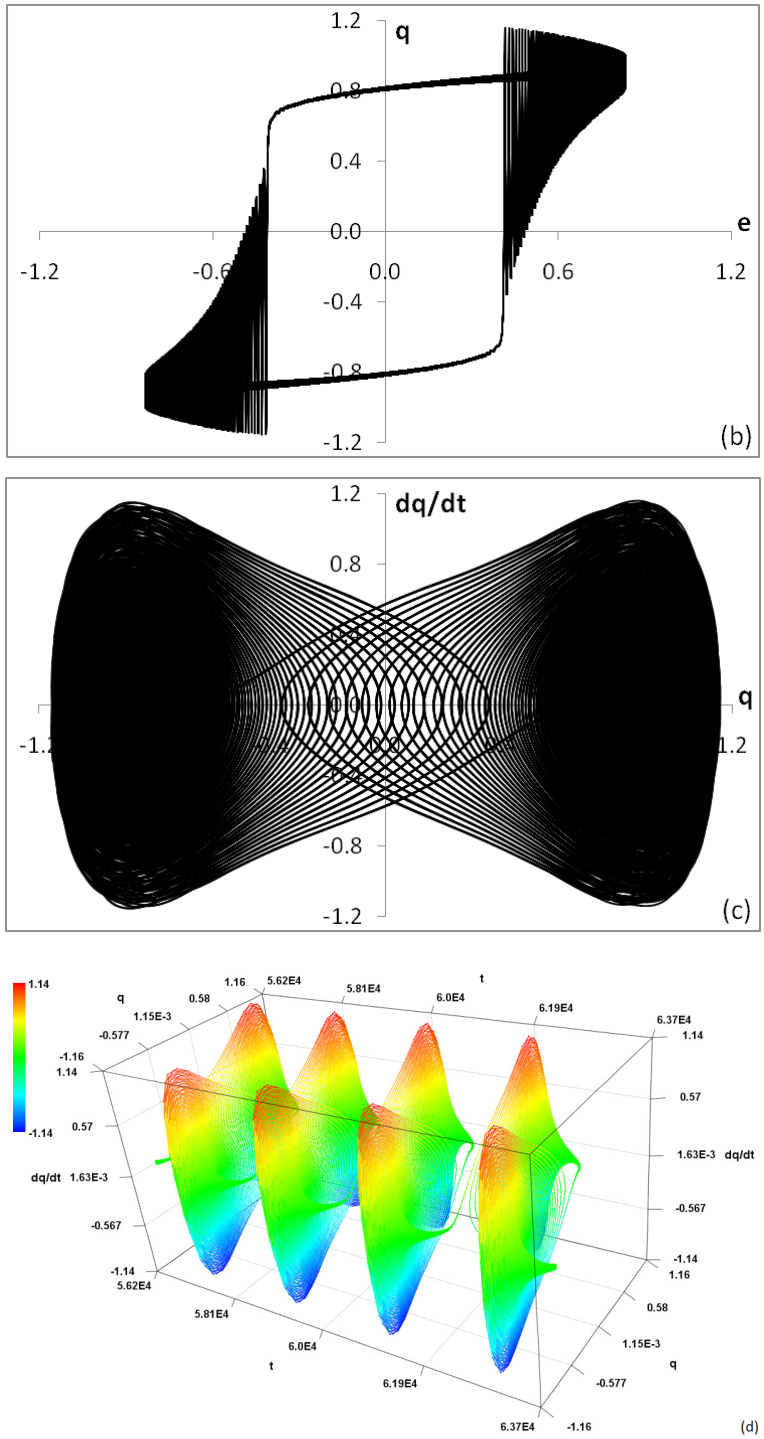

Fig. 12. AFE response for $f = 0.025\,f_0$, $e_0 = 2.0e_C$, $g = 0.01$, and $\lambda_q = -0.0041419531$. (a) e and q versus t, where e is represented by the black curve and q is represented by the red curve. (b) q versus e. (c) dq/dt versus q. (d) dq/dt versus q versus t.

For $e_0 = 249.0e_C \approx 103.7284$, $f = 25.5\,f_0 \approx 0.544081$, and $g = 0.3$, the AFE responses are shown in Figures 13(a) to 13(d). The maximal Lyapunov exponent is negative, approximately −0.218945. In Figure 13(a), e and q are slightly out of phase. The pattern of the q curve exhibits slightly distorted triangular waves with two branching peaks and troughs. It is periodic, as indicated by the overlap of the hysteresis loops and corresponding phase portraits for four cycles of e shown in Figures 13(b) and 13(c). Figure 13(c) shows that the responses of the AFE occupy a volume $V_q \approx 95.54$ in phase space. In Figure 13(d), the curve exhibits two windings around each attractor in each cycle, further elaborating on the dumbbell-shaped loops with extra windings on both sides of the phase portrait shown in Figure 13(c).

 https://www.doi.org/10.33910/2687-153X-2023-4-4-176-194

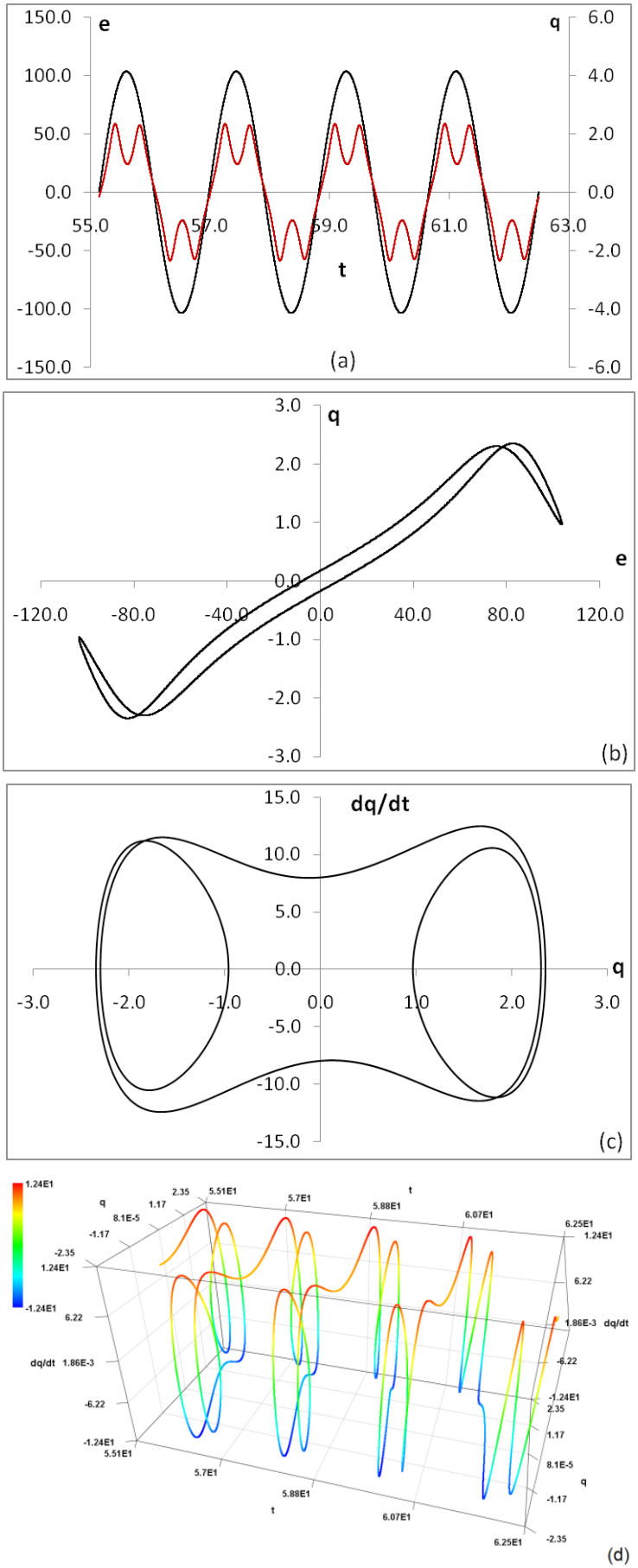

Fig. 13. AFE response for $f = 25.5f_0$, $e_0 = 249e_C$, $g = 0.3$, and $\lambda_q = -0.218945$. (a) e and q versus t, where e is represented by the black curve and q is represented by the red curve. (b) q versus e. (c) dq/dt versus q. (d) dq/dt versus q versus t.

For $e_0 = 249.0 e_C \approx 103.7284$, $f = 25.5 f_0 \approx 0.544081$, and $g = 0.01$, the AFE responses are shown in Figures 14(a) to 14(d). The maximal Lyapunov exponent is positive, approximately 3.230842. Figures 14(a) to 14(d) exhibit similar characteristics to Figures 8(a) to 8(d) and Figures 10(a) to 10(d), with the exception that the responses of the AFE occupied a large volume, $V_q \approx 197.24$, in phase space, which is approximately double compared to the one shown in Figure 13(c).

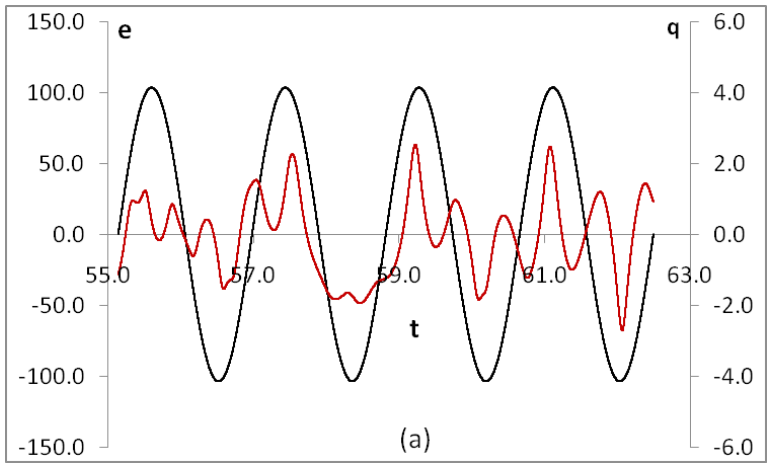

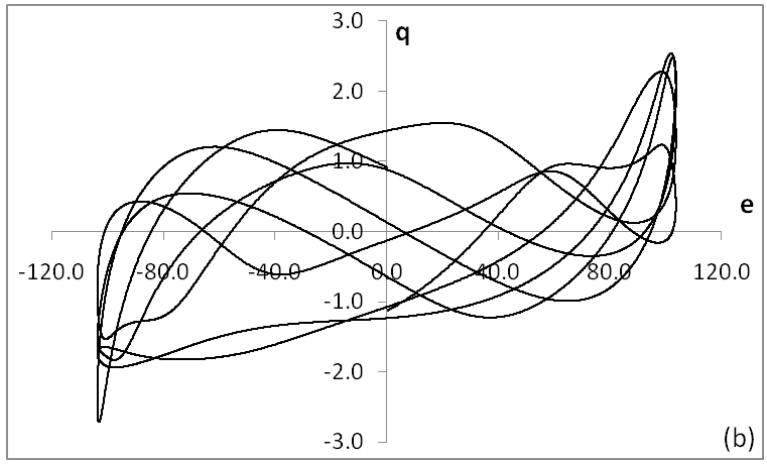

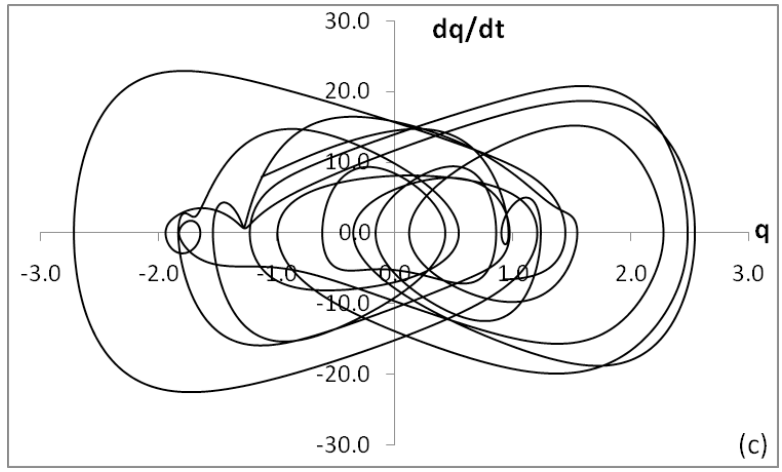

 https://www.doi.org/10.33910/2687-153X-2023-4-4-176-194

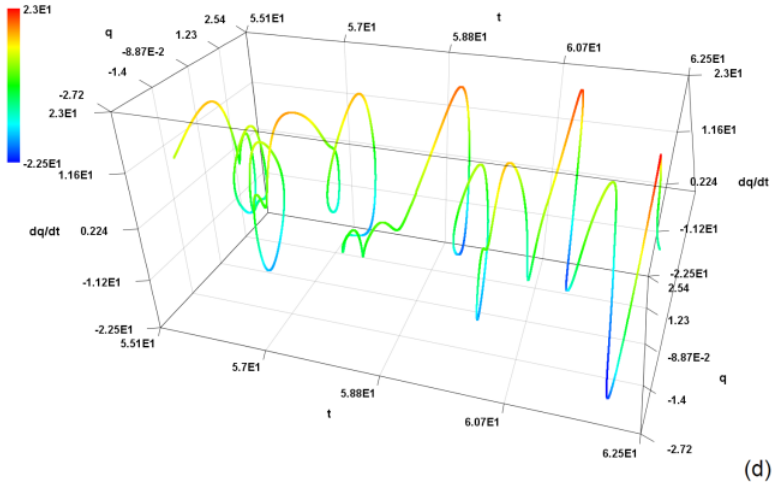

Fig. 14. AFE response for $f = 25.5f_0$, $e_0 = 249e_C$, $g = 0.01$, and $\lambda_q = 3.230842$. (a) e and q versus t, where e is represented by the black curve and q is represented by the red curve. (b) q versus e. (c) dq/dt versus q. (d) dq/dt versus q versus t.

Conclusions

The results of the first part indicate that, for small amplitudes (e_0) and frequencies (f) of the applied field, the Lyapunov exponents (λ_q) for $g = 0.01$ are greater than those for $g = 0.3$. Additionally, most of the periodic windows, corresponding to $\lambda_q < 0$, are observed in curves with a large damping constant ($g = 0.3$).

In the second part, it is observed that as the amplitude of the applied field (e_0) varies from low values and sweeps through e_C to high values, the Lyapunov exponents (λ_q) decrease discontinuously at $e_0 \approx e_C$, regardless of the frequency. Furthermore, for applied fields with low frequencies ($f \le 0.5f_0$) and amplitudes greater than the cohesive field ($e_0 > e_C$), in a system with large damping ($g = 0.3$), the Lyapunov exponents (λ_q) are negative.

The results from the third part demonstrate that the time-varying dimensionless normal displacements (q) are distorted compared to the sinusoidal applied field (e). It is observed that, for the negative Lyapunov exponents, the trajectories in phase space spiral towards attractors regardless of damping. The magnitude of the system's responses is proportional to the volume in phase space (V_q) occupied by the trajectories.

In most cases, V_q is smaller for large damping and larger for small damping, as shown in Figures 6(c) to 8(c) and 11(c) to 14(c). For cases near e_C, the relative responses exhibit large fluctuations with respect to frequency. For example, when $e_0 = 0.9e_C$ and $f = 2.275f_0$, V_q for large damping ($g = 0.3$) in Figure 7(c) is approximately 232 times smaller than V_q for small damping ($g = 0.01$) in Figure 8(c). Conversely, when $e_0 = 0.9e_C$ and $f = 7.05f_0$, V_q for large damping in Figure 9(c) is approximately 1.1 times larger than V_q for small damping in Figure 10(c). In general, large damping tends to suppress chaos when e_0 is not close to e_C.

For cases with large damping and positive λ_q, the orbits of trajectories exhibit significant overlap across consecutive cycles of the driving field, as shown in Figures 6(c), 7(c), and 9(c). When λ_q is negative, the responses are periodic, and the orbits of trajectories spiral towards attractors, particularly for moderate values of amplitude values (e. g., $e_0 = 2.0e_C$) and low frequencies (e. g., $f = 0.025f_0$). However, this effect is less obvious for large value of amplitude values (e. g., $e_0 = 249.0e_C$) and high frequencies (e. g., $f = 25.5f_0$).

As a summary, the numerical results demonstrate that periodic responses occur when $\lambda_q < 0$, as shown in Figures 11 to 13. When e_0 and f are very small, irrespective of the damping, λ_q is positive, leading to quasi-periodic responses. For moderate values of e_0 and f, when $\lambda_q > 0$, the responses with damping $g = 0.01$ exhibit chaotic behaviour, as shown in Figures 8, 10, and 14, while the responses with damping $g = 0.3$ appear quasi-periodic, as indicated by the overlapping hysteresis loops and phase portraits in Figures 7 and 9. Larger damping in the AFE system reduces the chaotic response and the density of chaos. Consequently, large damping can regulate response to the driving field, even though the system is chaotic.

Based on the comprehensive numerical results, we conclude that, for the antiferroelectric system in its first-order phase, the method of calculating the Lyapunov exponent and plotting phase portraits proves to be an efficient approach for identifying the regimes of amplitude and frequency of the applied field that lead to periodic and chaotic responses, particularly in the case of small damping. This approach offers an alternative to studying chaotic dynamics through multiple phase portraits (Lim 2022). The numerical simulations confirm that by manipulating the amplitude, frequency, and damping parameters of the AFE system, it is possible to control and regulate the occurrence of chaotic and periodic responses in the bulk AFE system. Utilizing the largest Lyapunov exponent as an informative indicator for characterizing the system's nonlinear behaviors proves to be an effective approach.

Conflict of Interest

The author declares that there is no conflict of interest, either existing or potential.

References

Baker, G. L., Gollub, J. P. (1996) *Chaotic dynamics: An introduction*. 2nd ed. Cambridge: Cambridge University Press, 268 p. (In English)

Benettin, G., Pasquali, S., Ponno, A. (2018) The Fermi-Pasta-Ulam problem and its underlying integrable dynamics: An approach through Lyapunov Exponents. *Journal of Statistical Physics*, 171 (4), 521–542. https://doi.org/10.1007/s10955-018-2017-x (In English)

Boyce, W. E., DiPrima, R. C. (2001) *Elementary differential equations and boundary values problems*. 7th ed. Singapore: John Wiley & Sons Publ., 745 p. (In English)

Dykman, M. I., Mannella, R., McClintock, P. V. E. et al. (1988) Spectral density of fluctuation of a double-well Duffing oscillator driven by white noise. *Physical Review A*, 37 (4), 1303–1312. https://doi.org/10.1103/PhysRevA.37.1303 (In English)

Goldstein, H., Poole, C., Safko, J. (2002) *Classical mechanics*. 3rd ed. Boston: Addison–Wesley Publ., 665 p. (In English)

Lega, E., Guzzo, M., Froeschlé, C. (2016) Theory and applications of the fast Lyapunov indicator (FLI) method. In: C. Skokos, G. Gottwald, J. Laskar (eds.). *Chaos Detection and Predictability*. Berlin; Heidelberg: Springer Publ., pp. 35–54. http://dx.doi.org/10.1007/978-3-662-48410-4_2 (In English)

Lim, S.-Ch. (2022) Numerical simulations of nonlinear and chaotic order parameter responses in bulk antiferroelectrics using ammonium dihydrogen phosphate parameter. *Physics of Complex Systems*, 3 (3), 122–136. https://www.doi.org/10.33910/2687-153X-2022-3-3-122-136 (In English)

Marion, J. B., Thornton, S. T. (1995) *Classical dynamics of particles and systems*. 4th ed. New York: Harcourt College Publ., 672 p. (In English)

Meunier, T., LaCasce, J. H. (2021) The finite size lyapunov exponent and the finite amplitude growth rate. *Fluids*, 6 (10), article 348. https://doi.org/10.3390/fluids6100348 (In English)

Strogatz, S. H. (2015) *Nonlinear dynamics and chaos with applications to Physics, Biology, Chemistry, and Engineering*. 2nd ed. New York: CRC Press, 532 p. https://doi.org/10.1201/9780429492563 (In English)

Wolf, A., Swift, J. B., Swinney, H. L., Vastano, J. A. (1985) Determining lyapunov exponents from a time series. *Physica D: Nonlinear Phenomena*, 16 (3), 285–317. https://doi.org/10.1016/0167-2789(85)90011-9 (In English)

Semiconductor Physics.
Physics of nanostructures

UDC 538.9 + 539.8

EDN RRDAEF
https://www.doi.org/10.33910/2687-153X-2023-4-4-195-202

Peculiarities of the structure and optical properties of amorphous semiconductor plasmon nanocomposites TiO_2<Ag>, prepared by ion plasma co-sputtering

K. Dauithan[1], O. Yu. Prikhodko[1], S. L. Peshaya✉[1], Y. S. Mukhametkarimov[1], S. A. Kozyukhin[2], S. Ya. Maksimova[1], G. A. Ismaylova[1]

[1] NAO al-Farabi Kazakh National University, 71 al-Farabi Ave., Almaty 050040, Kazakhstan
[2] N.S. Kurnakov Institute of General and Inorganic Chemistry of RAS, 31 Leninsky Ave., Moscow 119991, Russia

Authors

Kuanyshbek Dauithan, e-mail: dkuansh@mail.ru

Oleg Yu. Prikhodko, ORCID: 0000-0002-7506-2762, e-mail: prikhodko_o@mail.ru

Svetlana L. Peshaya, ORCID: 0000-0002-1814-7567, e-mail: skysvetik91@mail.ru

Yerzhan S. Mukhametkarimov, ORCID: 0000-0003-1381-4532, e-mail: m.c.erzhan@mail.ru

Sergey A. Kozyukhin, ORCID: 0000-0002-7405-551X, e-mail: kozyukhin59@bk.ru

Suyumbika Ya. Maksimova, ORCID: 0000-0001-7759-0326, e-mail: mak.son.21@mail.ru

Guzal A. Ismaylova, ORCID: 0000-0002-1813-2031, e-mail: guzal_a81@mail.ru

For citation: Dauithan, K., Prikhodko, O. Yu., Peshaya, S. L., Mukhametkarimov, Y. S., Kozyukhin, S. A., Maksimova, S. Ya., Ismaylova, G. A. (2023) Peculiarities of the structure and optical properties of amorphous semiconductor plasmon nanocomposites TiO_2<Ag>, prepared by ion plasma co-sputtering. *Physics of Complex Systems*, 4 (4), 195–202. https://www.doi.org/10.33910/2687-153X-2023-4-4-195-202 EDN RRDAEF

Received 28 June 2023; reviewed 20 September 2023; accepted 20 September 2023.

Funding: This study was supported by the Science Committee of the Ministry of Science and Higher Education of the Republic of Kazakhstan (Grant No. AP09258922).

Abstract. Structure and optical properties of amorphous semiconductor nanocomposite TiO_2<Ag> films prepared by ion-plasma RF magnetron co-sputtering of a TiO_2 and Ag target only in the argon atmosphere are studied. Matrix of TiO_2<Ag> films is amorphous with inclusions of isolated 3–4 nm sized silver nanoparticles. The optical transmission spectra have a sharp edge of fundamental absorption band at ~ 300 nm, which is formed by direct and indirect allowed optical transitions. The band gap of the TiO_2<Ag> films increases with the Ag concentration due to some ordering of the matrix. The absorption band is observed in the visible region of the spectrum due to the effect of local surface plasmon resonance absorption (LSPR) on silver nanoparticles. The LSPR intensity increases with the silver concentration, and the maximum of the absorption band, depending on the Ag concentration, is located in the region from 455 to 488 nm.

Keywords: ion-plasma sputtering, amorphous plasmon semiconductor nanocomposites TiO_2<Ag>, silver nanoparticles, structure, optical properties, surface plasmon resonance absorption

Introduction

Titanium dioxide films (TiO_2), a polymorphic wide-gap semiconductor material (anatase, rutile, brookite), are widely used in various fields: from biomedicine to solar energy (Banerjee et al. 2015; Cao et al. 2016; Ghann et al. 2016; Kulkarni et al. 2015; Pakdel et al. 2013). This is due to the generation of high-energy electrons in TiO_2 under the action of near-UV radiation. In recent years, many studies have been aimed to expand of the functional properties of these films by embedding elements of different chemical nature and creating composites on their basis. Special attention is paid to composite films based

on TiO_2 with inclusions of isolated nanoparticles of noble metals such as Ag and Au (Prakash et al. 2016; Wodka et al. 2010; Yu et al. 2017; Zhao et al. 1996). In such wide-gap semiconductor nanocomposite TiO_2<Ag> and TiO_2<Au> films, an absorption band is observed in the visible region of the spectrum due to local surface plasmon resonance (LSPR) on metal nanoparticles. Such films are of significant interest for the physics of plasmon phenomena and have important applied significance, in particular, for improving the photocatalytic and optical properties of TiO_2 films (Bueno-Alejo et al. 2017).

The semiconductor composite TiO_2 films with inclusions of Ag and Au nanoparticles are obtained by various chemical and physical methods. For example, the sol-gel method, PLD, photoreduction treatment, ion doping and magnetron ion-plasma DC/RF co-sputtering (Ghidelli et al. 2020; Navabpour et al. 2014; Ozimek et al. 2016; Pan, Heagy 2019; Usha et al. 2016; Yuan et al. 2017; Zada et al. 2017). Ion-plasma RF magnetron co-sputtering has a number of advantages over other methods. This is due to the possibility of obtaining continuous and homogeneous composite films and the possibility to be well integrated into the planar technology of electronic device manufacturing (Prikhodko et al. 2014). However, in the technology of obtaining TiO_2 films with isolated Ag and Au nanoparticles and with the LSPR effect, the sputtering is carried out in the atmosphere of a mixture of inert gas argon with oxygen and with the obligatory subsequent thermal treatment of the films in air or in the argon and hydrogen mixture (Rodrigues et al. 2018; Torrell et al. 2011), which ultimately complicates the technology of their production.

In this work, we show the possibility of obtaining amorphous semiconductor nanocomposite films TiO_2<Ag> with a brightly pronounced LSPR effect, i. e. plasmon nanocomposites, synthesized by ion-plasma radio-frequency (RF) magnetron co-sputtering only in argon atmosphere, and the peculiarities of their structure and optical properties are studied.

Experimental Technique

Thin nanocomposite TiO_2<Ag> films were obtained by ion-plasma RF (13.56 MHz) magnetron sputtering of a combined TiO_2 and Ag target in an argon atmosphere (99.998%) at a pressure ~ 0.5 Pa. A preliminary high vacuum (~ 10^{-4} Pa) was created by oil-free forevacuum (BocEdwards XDS10) and turbomolecular (BB-150) pumps. The films were deposited on KU-1 fused silica substrates, fresh cleavages of NaCl and KBr crystals, and single-crystal silicon (c-Si) plates that were kept at room temperature. The technological parameters of the sputtering were selected so as to obtain an amorphous TiO_2 matrix with inclusions of isolated silver nanoparticles.

The elemental composition and morphology of the films were monitored by energy dispersive analysis (EDX) using a Quanta 3D 200i SEM with an EDAX. The thickness of the films was measured by scanning a cleavage of the c-Si/TiO_2 and c-Si/TiO_2<Ag> sandwich structures on SEM and ranged from 40 to 50 nm. For these measurements, the films were deposited on c-Si substrates cleaned from the SiO_2 oxide layer. It was found that the composition of TiO_2 films is close to stoichiometric, and the Ag concentration in TiO_2<Ag> films reaches 9.0 at. %.

The structure of TiO_2 and TiO_2<Ag> films was studied by transmission electron microscopy (TEM JEM 2100 JEOL). The optical properties (transmission $T = f(\lambda)$ and reflection spectra $R = f(\lambda)$) of films deposited on quartz substrates were studied on a Shimadzu UV2000 spectrophotometer in the spectral range from 250 to 1100 nm with the recording step—1 nm.

Results and discussion

The structure of TiO_2 and TiO_2<Ag> films

Fig. 1 a-e shows typical TEM images and selected area electron diffraction (SAED) patterns of TiO_2 and TiO_2<Ag> films with silver concentration 9.0 at. %. Figs. 1 b and d show typical SAED patterns of TiO_2 films and the matrix of the TiO_2<Ag> film. The SAED of TiO_2 film (Fig. 1 b) and matrix of the film TiO_2<Ag> (Fig. 1 d) are characterized by a diffuse halo, which is indicative of their amorphous structure. However, in the matrix of TiO_2<Ag> films, the diffuse halo is less blurred, so its structure is more ordered. The decoding of SAED ring reflections (Figs. 1 d and e) is performed using the CrysTBox program (Klinger, Jäger 2015).

 https://www.doi.org/10.33910/2687-153X-2023-4-4-195-202

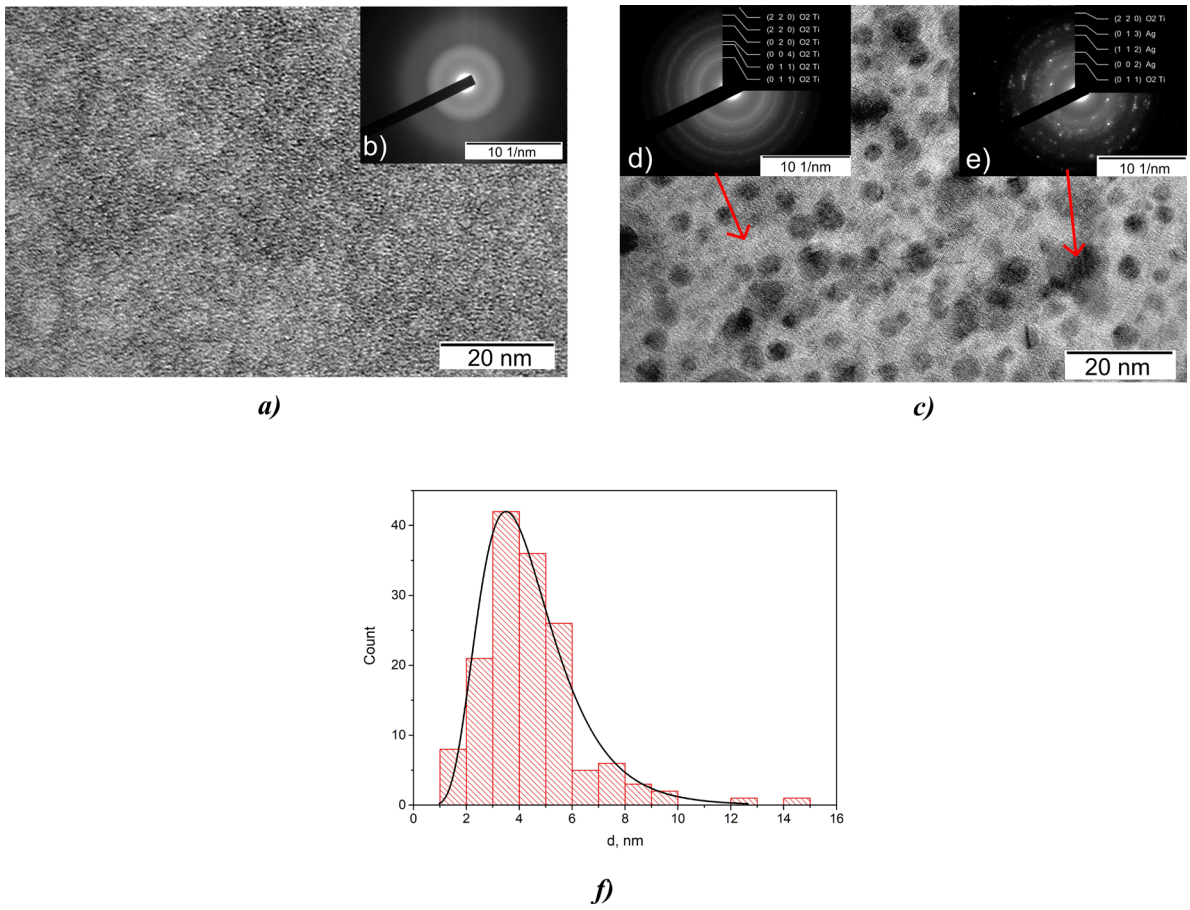

Fig. 1. TEM images (a, c) and SAED patterns (d, e) of TiO_2 (a, b) and TiO_2<9.0 at. % Ag> (c, d, e) films, as well as the size distribution of Ag nanoparticles in TiO_2<9.0 at.% Ag> film (f)

The TiO_2<Ag> film matrix contains isolated nanoparticles (Fig. 1 c). SAED of the nanoparticle (Fig. 1 e) shows clearly pronounced point reflections characteristic of a single-crystal structure. It follows from the interpretation of the SAED that this nanoparticle is silver.

Fig. 1 f shows a histogram of the size distribution of Ag nanoparticles in TiO_2<9.0 at.% Ag> films, obtained as a result of the TEM image processing. We can see that most silver nanoparticles have a diameter ~ 3–4 nm, and the distribution itself is lognormal. The same sizes for silver nanoparticles were obtained for TiO_2<Ag> films with other Ag concentrations. Similar results were obtained for wide-gap semiconductor nanocomposite a-C:H<Ag> films with the LSPR effect, also prepared by ion-plasma co-sputtering (Prikhodko et al. 2016; 2017).

Thus, the nanocomposite TiO_2<Ag> films, obtained by ion-plasma RF magnetron co-sputtering of TiO_2 and Ag in only argon atmosphere, consist of amorphous TiO_2 matrix and isolated crystalline silver nanoparticles.

Optical properties of TiO_2 and TiO_2<Ag> films

Fig. 2 shows the optical transmission spectra of the TiO_2 and TiO_2<Ag> films with different silver concentrations. It can be seen that the spectra of the films are characterized by the sharp transmission band edge (fundamental absorption band edge) in the near UV range from 280 to 320 nm. The slope of the passband edge changes with an increase in the silver concentration in the TiO_2<Ag> films: it increases significantly with the Ag concentration from 0 to 4.9 at. %, and then decreases slightly. The TiO_2 films in the visible and near IR regions (from 400 to 1100 nm) have a sufficiently high transmittance. In contrast, a pronounced absorption band with a maximum in the visible region of the spectrum is observed in TiO_2<Ag> films.

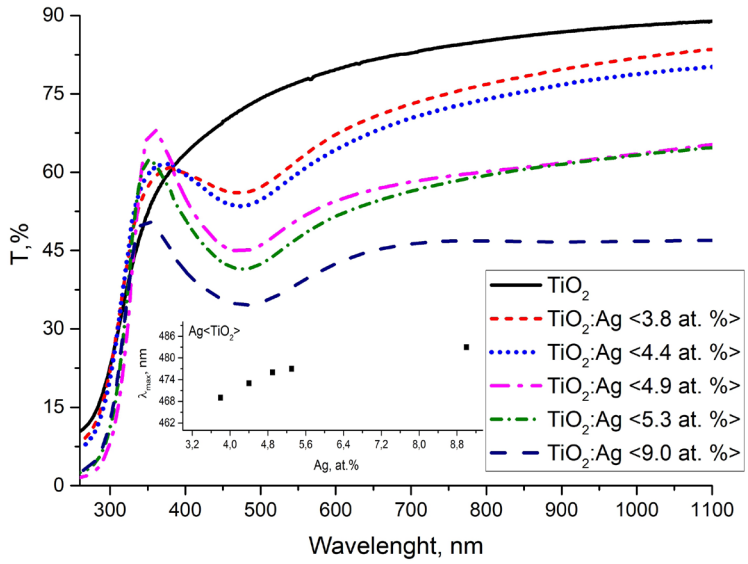

Fig. 2. Transmission spectra of TiO_2 and TiO_2<Ag> films with different concentration of silver

Fig. 2 shows that an increase in the Ag concentration (the volume fraction of Ag nanoparticles) leads to a significant increase in the intensity of this absorption band. The maximum of the absorption band, depending on the Ag concentration, is located in the range from 455 to 488 nm. As the concentration increases, the resonance peak shifts towards longer wavelengths. The main shift of the maximum is observed in the region up to 4.9 at. % Ag.

According to (Manikandan et al. 2003), the observed absorption band in TiO_2<Ag> films is due to the effect of surface plasmon resonance (LSPR) in consequence of resonant absorption of electromagnetic radiation by free surface electrons of isolated silver nanoparticles.

In (Ievlev et al. 2014), it was shown for polycrystalline semiconductor nanosized anatase films that the edge of the fundamental absorption band is formed by both indirect and direct allowed transitions. In this connection, we analyze the features of the fundamental absorption of the studied amorphous semiconductor nanosized TiO_2 and TiO_2<Ag> films.

The optical band gap (E_g) of the films was estimated using the Tauc method (Tauc et al. 1966). According the method, in the fundamental absorption region when the absorption coefficient $\alpha \geq 10^4$ cm^{-1}, the relationship between the light photon energies $h\nu$, α, and E_g is described by the relation

$$\alpha h\nu \sim (h\nu - E_g)^{1/n}, \quad (1)$$

where $n = 1/2$ corresponds to allowed direct-gap optical transitions, $n = 2$—to allowed indirect-gap transitions (quadratic absorption law) (Tauc et al. 1966).

The optical band gap of TiO_2 and TiO_2<Ag> films was determined for both allowed direct-gap and indirect-gap optical transitions. The error in E_g did not exceed ± 0.01 eV. Fig. 3 shows the spectral dependences $(\alpha h\nu)^{1/2}$ and $(\alpha h\nu)^2$ for nanosized TiO_2 and TiO_2<Ag> films with an Ag concentration of 4.9, 5.3, and 9.0 at. %.

 https://www.doi.org/10.33910/2687-153X-2023-4-4-195-202

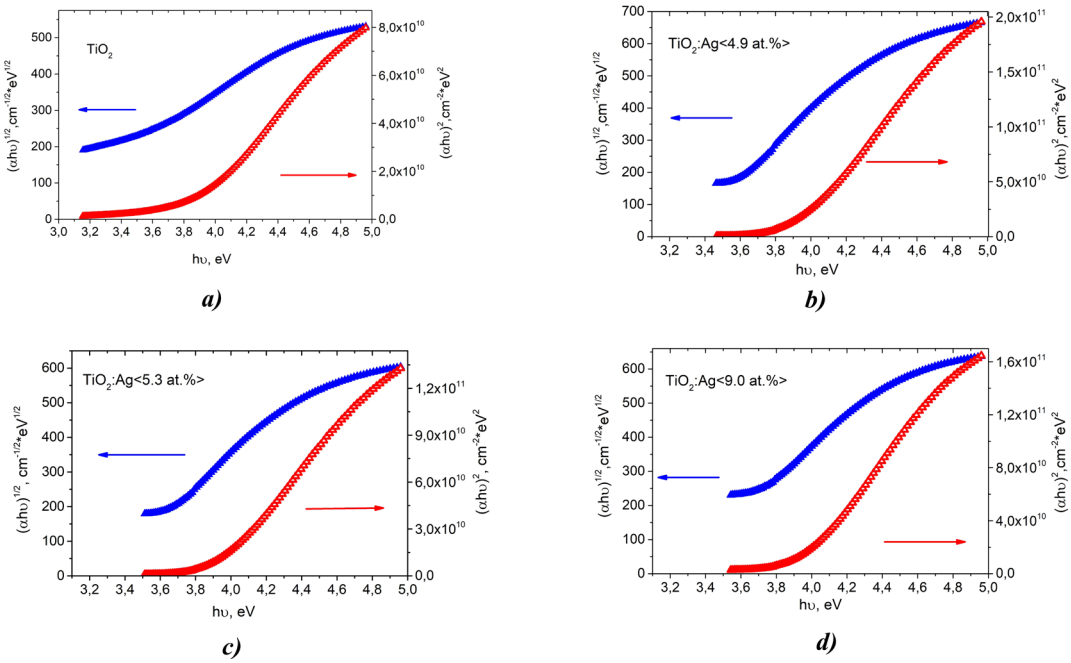

Fig. 3. Spectral dependences $(\alpha h\nu)^{1/2}$ and $(\alpha h\nu)^2$ for TiO_2 (a) and TiO_2<Ag> (b-d) films

It can be seen that in the TiO_2 and TiO_2<Ag> films spectra there are rather extended characteristic rectilinear sections, and extrapolation of them to the energy axis $h\nu$ gives the values of E_g. However, the detailed analysis shows that the most extended characteristic rectilinear sections are that when n = 2 (quadratic absorption law). It follows that the edge of the fundamental absorption band in the TiO_2 and TiO_2<Ag> films is mainly formed by indirect allowed optical transitions.

Fig. 4 (curves 1 and 2) shows the concentration dependences of TiO_2<Ag> films optical band gap. The E_g values of the films correspond to semiconductor wide-gap materials. Optical band gap for TiO_2 and TiO_2<Ag> films in the case of n = 2 (the quadratic absorption law) are significantly lower than that of n = 1/2. When n = ½, the insignificant rise of E_g with Ag concentration occurs, but when n = 2, the significant increase of E_g takes place in the region of Ag concentration from 0 to 4.9 %, and later on E_g practically is invariable. Note, that the E_g for TiO_2<Ag> films considering both absorption laws with Ag concentration exceeding 3.8 at.% practically coincide with the data (Zhang et al. 2006) for polycrystalline anatase films.

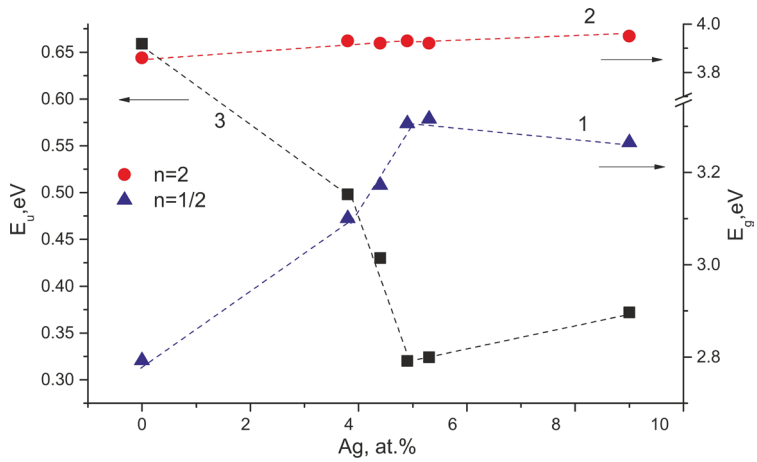

n = 1/2 (curve 2), n=2 (curve 1)

Fig. 4. Concentration dependences of TiO_2<Ag> films E_g for different laws of absorption (curves 1 and 2) and Urbach energy E_u (curve 3)

To explain the increase in the optical band gap in nanocomposite TiO_2<Ag> films, let us consider the variation with the Ag concentration of the Urbach energy (E_u) (Fig. 4, curve 3). According to (Akshay et al. 2019; Urbach et al. 1953), E_u characterizes the degree of semiconductor structure disorder, which determines the tail extension of the density of states at the boundaries of the allowed energy bands E_c and E_v. The relationship between the absorption coefficient α, the energy of the incident photon $h\nu$, and the Urbach energy E_u is given by the following relation (the empirical Urbach's rule)

$$\alpha \sim \exp(h\nu/E_u). \quad (2)$$

The Urbach energy was estimated from the low-energy region of the absorption spectrum. It is seen from Fig. 4 that the Urbach energy significantly decreases in the region from 0 to 4.9 at. % with Ag concentration increase, but the optical band gap of TiO_2<Ag> films significantly rises, in the case of a quadratic absorption mechanism. A further increase in the silver concentration to 9.0 at. % leads to an insignificant increase in the Urbach energy and an insignificant decrease in E_g, i. e., there is a correlation between changes in E_u and E_g when a quadratic absorption law take place. It follows that the increase in the Ag concentration in the TiO_2<Ag> films leads to the decrease of the density of localized states tails extension in the band gap, which is indicative of the ordering of the amorphous TiO_2<Ag> films structure. This is in good agreement with the change in the steepness of the transmission (absorption) band edge founded in this work.

Considering our data on TEM (Peshaya et al. 2022) the ordering of the amorphous structure of TiO_2<Ag> films with an increase in the concentration of Ag from 0 to 4.9 at. %, apparently, is due to a decrease in the porosity of the films because of the filling of pores in them with silver nanoparticles. This, in turn, leads to an increase in the refractive index of the matrix and, as a consequence, to a shift of the resonant peak towards longer wavelengths.

A further increase in the concentration of silver in the films to 9.0 at. % leads to some disordering of the structure as a result of an increase in the amount of silver nanoparticles in the matrix of the films.

It should be noted that an increase in silver volume fraction in the TiO_2<Ag> nanocomposite can also lead, as the theory (Gibson et al. 1982) shows, to a shift of the resonance peak maximum towards longer wavelengths. Apparently, this is the reason for the further shift of the maximum to the red region.

Thus, the optical properties of amorphous semiconductor nanocomposite TiO_2<Ag> films are characterized by a sharp edge of the fundamental absorption band in the near UV region, which is formed mainly by indirect allowed optical transitions. The slope of the absorption band edge and the optical band gap depend on the silver concentration in the films. There is a pronounced LSPR effect in the visible region of the spectrum, the intensity of which increases significantly with the rise of Ag concentration.

Conclusions

Using the ion-plasma RF magnetron sputtering of a combined TiO_2 and Ag target in an atmosphere of only argon without subsequent heat treatment, amorphous semiconductor nanocomposite TiO_2<Ag> films with a thickness from 40 to 50 nm and with a silver concentration of up to 9.0 at. % were obtained.

It was found by TEM that the structure of the films consists of practically amorphous TiO_2 matrix and isolated silver nanoparticles with the diameter ~ 3–4 nm.

The resulting TiO_2<Ag> films are wide-gap semiconductor materials. The optical band gap of the films increases significantly with the silver concentration. The optical properties of TiO_2 and TiO_2<Ag> films are characterized by a sharp fundamental absorption edge at ~ 300 nm, which is due to direct and indirect allowed optical transitions. In the visible region of the spectra of TiO_2<Ag> films, a pronounced surface plasmon resonance absorption is manifested. The LSPR intensity significantly increases with an increase in the silver concentration in the films, and the absorption maximum, depending on the Ag concentration, is located in the region from 455 to 488 nm. The presence of isolated silver nanoparticles and their concentration influences on the degree of the structure order of the amorphous matrix of the TiO_2<Ag> film and, thus, the optical band gap of the films. Amorphous TiO_2<Ag> films, in comparison with TiO_2 films, have a more ordered structure of the amorphous TiO_2 matrix and, as a consequence, higher E_g.

The shown possibility of obtaining amorphous plasmon nanocomposite TiO_2<Ag> films using simpler technology is of significant interest for their application in structures fabricated in a continuous cycle of planar technology.

 https://www.doi.org/10.33910/2687-153X-2023-4-4-195-202

Conflict of Interest

The authors declare that there is no conflict of interest, either existing or potential.

Author Contributions

The authors have made an equal contribution to the paper.

References

Akshay, V. R., Arun, B., Mandal, G. et al. (2019) Visible range optical absorption, Urbach energy estimation and paramagnetic response in Cr-doped TiO_2 nanocrystals derived by a sol-gel method. *Physical Chemistry Chemical Physics*, 21 (24), 12991–13004. https://doi.org/10.1039/c9cp01351b (In English)

Banerjee, S., Dionysiou, D. D., Pillai, S. C. (2015) Self-cleaning applications of TiO_2 by photo-induced hydrophilicity and photocatalysis. *Applied Catalysis B: Environmental*, 176–177, 396–428. https://doi.org/10.1016/j.apcatb.2015.03.058 (In English)

Bueno-Alejo, C. J., Arca-Ramos, A., Hueso, J. L. (2017) Plasmonics devoted to photocatalytic applications in liquid, gas, and biological environments. In: G. Barbillon (ed.). *Nanoplasmonics—Fundamentals and Applications*. [S. l.]: InTech Publ. [Online]. Available at: https://doi.org/10.5772/intechopen.68812 (15.05.2023). (In English)

Cao, C., Yan, J., Zhang, Y., Zhao, L. (2016) Stability of titania nanotube arrays in aqueous environment and the related factors. *Scientific Reports*, 6 (1), article 23065. https://doi.org/10.1038/srep23065 (In English)

Ghann, W., Rahman, A., Rahman, A., Uddin, J. (2016) Interaction of sensitizing dyes with nanostructured TiO_2 film in dye-sensitized solar cells using terahertz spectroscopy. *Scientific Reports*, 6 (1), article 30140. https://doi.org/10.1038/srep30140 (In English)

Ghidelli, M., Mascaretti, L., Bricchi, B. R. et al. (2020) Light management in TiO_2 thin films integrated with Au plasmonic nanoparticles. *Semiconductor Science and Technology*, 35 (3), article 035016. https://doi.org/10.1088/1361-6641/ab6cea (In English)

Gibson, U. J., Craighead, H. G., Buhrman, R. A. (1982) Topological considerations in the optical properties of granular composite films. *Physical Review B*, 25 (2), 1449–1452. https://doi.org/10.1103/physrevb.25.1449 (In English)

Ievlev, V. M., Kushchev, S. B., Latyshev, A. N., Leonova, L. Yu. (2014) Absorption spectra of TiO_2 thin films synthesized by the reactive radio-frequency magnetron sputtering of titanium. *Semiconductors*, 48 (7), 848–858. https://doi.org/10.1134/S1063782614070094 (In English)

Klinger, M., Jäger, A. (2015) Crystallographic Tool Box (CrysTBox): Automated tools for transmission electron microscopists and crystallographers. *Journal of Applied Crystallography*, 48, 2012–2018. https://doi.org/10.1107/S1600576715017252 (In English)

Kulkarni, M., Mazare, A., Gongadze, E. et al. (2015) Titanium nanostructures for biomedical applications. *Nanotechnology*, 26 (6), article 062002. https://doi.org/10.1088/0957-4484/26/6/062002 (In English)

Manikandan, D., Mohan, S., Nair, K. G. M. (2003) Absorption and luminescence of silver nanocomposite soda-lime glass formed by Ag^+-Na^+ ion-exchange. *Materials Research Bulletin*, 38 (9–10), 1545–1550. https://doi.org/10.1016/S0025-5408(03)00165-X (In English)

Navabpour, P., Ostovarpour, S., Hampshire, J. et al. (2014) The effect of process parameters on the structure, photocatalytic and self-cleaning properties of TiO_2 and Ag-TiO_2 coatings deposited using reactive magnetron sputtering. *Thin Solid Films*, 571-1, 75–83. https://doi.org/10.1016/j.tsf.2014.10.040 (In English)

Ozimek, M., Palewicz, M., Hreniak, A. (2016) Optical properties of TiO_2 nanopowder doped by silver (copper) during synthesis or PVD method. *Acta Physica Polonica A*, 129 (6), 1214–1219. https://doi.org/10.12693/APhysPolA.129.1214 (In English)

Pakdel, E., Daoud, W. A., Wang, X. (2013) Self-cleaning and superhydrophilic wool by TiO_2/SiO_2 nanocomposite. *Applied Surface Science*, 275, 397–402. https://doi.org/10.1016/j.apsusc.2012.10.141 (In English)

Pan, H., Heagy, M. D. (2019) Plasmon-enhanced photocatalysis: Ag/TiO_2 nanocomposite for the photochemical reduction of bicarbonate to formic acid. *MRS Advances*, 4 (7), 425–433. https://doi.org/10.1557/adv.2018.677 (In English)

Peshaya, S. L., Prikhodko, O. Yu., Mukhametkarimov, Ye. S. et al. (2022) Osobennosti opredeleniya opticheskoj shiriny zapreshchennoj zony amorfnykh nanorazmernykh kompozitnykh plenok TiO_2:Ag [Peculiarities of determining the optical band gap of amorphous nanosized TiO_2:Ag composite films]. *Opticheskij zhurnal — Journal of Optical Technology*, 89 (1), 74–81. (In Russian)

Prakash, J., Kumar, P., Harris, R. A. et al. (2016) Synthesis, characterization and multifunctional properties of plasmonic Ag-TiO_2 nanocomposites. *Nanotechnology*, 27 (35), article 355707. https://doi.org/10.1088/0957-4484/27/35/355707 (In English)

Prikhodko, O., Manabayev, N., Guseinov, N. (2014) Plasmon resonance in a-C:H films modified with platinum nanoclusters. *Journal of Nano- and Electronic Physics*, 6 (3), article 03067. (In English)

Prikhodko, O. Yu., Mikhailova, S. L., Mukhametkarimov, E. C. et al. (2016) Optical properties of a-C:H thin films modified by Ti and Ag. *Proceedings of SPIE*, 9929, article 99291G. https://doi.org/10.1117/12.2238455 (In English)

Prikhodko, O. Yu., Mikhailova, S. L., Mukhametkarimov, Ye. S. et al. (2017) Structure and phase composition of thin a-C:H films modified by Ag and Ti. *Optics and Spectroscopy*, 123 (3), 383–387. https://doi.org/10.1134/S0030400X17090260 (In English)

Rodrigues, M. S., Costa, D., Domingues, R. P. et al. (2018) Optimization of nanocomposite Au/TiO_2 thin films towards LSPR optical-sensing. *Applied Surface Science*, 438, 74–83. https://doi.org/10.1016/j.apsusc.2017.09.162 (In English)

Tauc, J., Grigorovici, R., Vancu, A. (1966) Optical Properties and electronic structure of Ge optical properties and electronic structure of amorphous germanium. *Physica Status Solidi b*, 15 (2), 627–637. https://doi.org/10.1002/pssb.19660150224 (In English)

Torrell, M., Kabir, R., Cunha, L. et al. (2011) Tuning of the surface plasmon resonance in TiO_2/Au thin films grown by magnetron sputtering: The effect of thermal annealing. *Journal of Applied Physics*, 109 (7), article 074310. https://doi.org/10.1063/1.3565066 (In English)

Urbach, F. (1953) The long-wavelength edge of photographic sensitivity and of the electronic absorytion of solids. *Physical Review*, 92 (5), 1324–1324. https://doi.org/10.1103/PhysRev.92.1324 (In English)

Usha, K., Kumbhakar, P., Mondal, B. (2016) Effect of Ag-doped TiO_2 thin film passive layers on the performance of photo-anodes for dye-sensitized solar cells. *Materials Science in Semiconductor Processing*, 43, 17–24. https://doi.org/10.1016/j.mssp.2015.11.015 (In English)

Wodka, D., Bielaníska, E., Socha, R. P. et al. (2010) Photocatalytic activity of titanium dioxide modified by silver nanoparticles. *ACS Applied Materials and Interfaces*, 2 (7), 1945–1953. https://doi.org/10.1021/am1002684 (In English)

Yu, Y., Wen, W., Qian, X.-Y. et al. (2017) UV and visible light photocatalytic activity of Au/TiO_2 nanoforests with Anatase/Rutile phase junctions and controlled Au locations. *Scientific Reports*, 7 (1), article 41253. https://doi.org/10.1038/srep41253 (In English)

Yuan, X., Xu, W., Huang, F. et al. (2017) Structural colors of fabric from Ag/TiO_2 composite films prepared by magnetron sputtering deposition. *International Journal of Clothing Science and Technology*, 29 (3), 427–435. https://doi.org/10.1108/IJCST-04-2016-0038 (In English)

Zada, I., Zhang, W., Zheng, W. et al. (2017) The highly efficient photocatalytic and light harvesting property of Ag-TiO_2 with negative nano-holes structure inspired from cicada wings. *Scientific Reports*, 7 (1), article 17277. https://doi.org/10.1038/s41598-017-17479-8 (In English)

Zhang, J., Li, M., Feng, Z. et al. (2006) UV Raman spectroscopic study on TiO_2-I. phase transformation at the surface and in the bulk. *Journal of Physical Chemistry B*, 110 (2), 927–935. https://doi.org/10.1021/jp0552473 (In English)

Zhao, G., Kozuka, H., Yoko, T. (1996) Sol—gel preparation and photoelectrochemical properties of TiO_2 films containing Au and Ag metal particles. *Thin Solid Films*, 277 (1–2), 147–154. https://doi.org/10.1016/0040-6090(95)08006-6 (In English)

Semiconductor Physics. Semiconductors

UDC 538.9

EDN WRDYMW
https://www.doi.org/10.33910/2687-153X-2023-4-4-203-209

Energy spectrum of holes in highly alloyed PbTe

S. A. Nemov[✉1,2], Z. M. Dashevsky[3], V. Yu. Proklova[4], N. A. Mikhailov[2]

[1] Peter the Great Saint Petersburg Polytechnic University, 29 Politekhnicheskaya Str., Saint Petersburg 195251, Russia
[2] Saint Petersburg Electrotechnical University "LETI", 5 Professora Popova Str., Saint Petersburg 197022, Russia
[3] Ben-Gurion University of the Negev, 1 David Ben Gurion Blvd, Beer Sheva 653 8410501, Israel
[4] Transbaikal State University, 30 Alexandro-Zavodskaya Str., Chita 672039, Russia

Authors

Sergei A. Nemov, ORCID: 0000-0001-7673-6899, e-mail: nemov_s@mail.ru

Zinovi M. Dashevsky, ORCID: 0000-0001-9268-4873, e-mail: zdashev@bgu.ac.il

Victoria Yu. Proklova, e-mail: pvictoria78@mail.ru

Nikita A. Mikhailov, e-mail: nmikhaylov@stud.etu.ru

For citation: Nemov, S. A., Dashevsky, Z. M., Proklova, V. Yu., Mikhailov, N. A. (2023) Energy spectrum of holes in highly alloyed PbTe. *Physics of Complex Systems*, 4 (4), 203–209. https://www.doi.org/10.33910/2687-153X-2023-4-4-203-209 EDN WRDYMW

Received 21 September 2023; reviewed 13 October 2023; accepted 13 October 2023.

Funding: The study did not receive any external funding.

Abstract. The electrophysical properties of a series of PbTe samples doped with Tl and an additional admixture of Na are investigated. Observed features of temperature dependences of electrical conductivity and Hall's coefficient are explained within the framework of the model of resonant states of thallium, taking into account the complex structure of the valence band. It is shown that the idea of an ideal crystal and a band structure in the framework of the one-electron approximation is insufficient to explain the experimental data on the Hall effect. It is necessary to take into account the modification of the energy spectrum taking into account the statistical distribution of impurities and defects and the additional interaction of particles.

Keywords: PbTe, energy spectrum of holes, TI and Na impurities, Fermi level stabilization, modification of the band spectrum

Introduction

Chalcogenides of elements of groups IV and V of the periodic table are widely used in thermoelectricity. They are the main materials for the manufacture of low-temperature and medium-temperature energy converters. The most studied are the tellurides of lead (PbTe), tin (SnTe) and bismuth (Bi_2Te_3).

From the point of view of the band theory, these materials occupy an intermediate position between classical metals and semiconductors. Like semiconductors, they have a band gap (E_g). At the same time, they are characterized by metallic-type conductivity up to the lowest temperatures. They have electron and hole conductivity due to their own electroactive point defects that do not have levels in the band gap. So the concentration of free carriers in the permitted zones is maintained at low temperatures ($T \to 0$ K) like ordinary metals.

Due to the wide area of homogeneity, these materials are not pure (having only their own conductivity). Typical concentrations of electrons (n) and holes (p) in native unalloyed materials are of the order of 1×10^{18} cm^{-3} in lead chalcogenides, 1×10^{19} cm^{-3} in bismuth telluride and 1×10^{20} cm^{-3} in SnTe and Sb_2Te_3 (Abrikosov et al. 1975; Gol'tsman et al. 1972; Ravich et al. 1968).

Despite numerous studies, the band structure of thermoelectric materials has not been studied sufficiently and is controversial, especially in the field of high Fermi energies (E_F).

According to the results of calculations (Nemov, Ravich 1998; Volkov et al. 1983; 1984), the energy spectrum of the density of electronic states of the valence band *g(E)* of lead and tin chalcogenides has the following form (see Fig. 1).

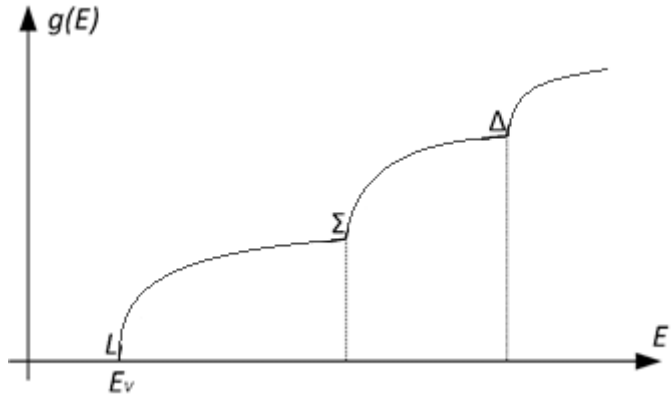

Fig. 1. Qualitative view of the energy spectrum of holes in PbTe and SnTe

The main extremes of the valence band of cubic PbTe and SnTe crystals are located at the L-points of the Brillouin zone. The dependence of the energy E on the quasi-pulse p of charge carriers at these extremes is non-parabolic and, in agreement with experimental data, is well described by the Kane model (Ravich et al. 1968) up to approximately the values of the Fermi energy $E_F \approx 0.15$ eV.

In the monograph (Ravich et al. 1968), the energy spectrum of holes in PbTe is considered in detail experimentally and theoretically in the region of low Fermi energies (up to a hole concentration less than 5×10^{19} cm^{-3}). The experimental data clearly show the contribution to the phenomena of carrier transfer of one kind (light holes) with a small effective mass $m_d \sim 0.1m_0$ (where m_0 is the mass of a free electron).

At high Fermi energies, charge carriers from an additional extremum contribute to the transfer phenomena. The Hall coefficients (R) and Seebeck coefficients (α) grow with temperature. The experimental data are described qualitatively by a two-band model (light and heavy holes with an effective mass of the order of the mass of a free electron). The authors (Nemov, Ravich 1998; Volkov et al. 1984) believe that the second extremum of the valence band is located at the Σ-points of the Brillouin zone and, possibly, is the saddle point.

At even higher hole energies, there is another extremum of the valence band, at Δ-points. It was experimentally observed in solid solutions of $Sn_{0.62}Pb_{0.33}Ge_{0.05}Te$ doped in (Nemov et al. 2000).

Note that high concentrations of holes (Fermi energy) in PbTe are achieved by doping with an acceptor impurity, traditionally with Na, which is the main dopant of the acceptor type in lead chalcogenides. With the help of Na, it is possible to obtain crystals with a concentration of holes up to 1.5×10^{20} cm^{-3} when samples are introduced into the charge about 1–2 at.% Na.

Note that small concentrations of holes in IV-VI materials are achieved due to a deviation from the stoichiometric composition towards an excess of chalcogen. It is significant that despite the change in the doping method (the transition from an excess of chalcogen to an admixture of sodium), the kinetic coefficients monotonically and smoothly change with increasing hole concentration.

An essential feature of lead and tin chalcogenides is the absence of defect levels and major alloying impurities (Na—acceptor, Cl—donor) in the forbidden zone (Ravich et al. 1968).

In the samples of PbTe doped with Na, characteristic features of temperature and concentration dependences of kinetic coefficients are observed, indicating the participation in the transfer phenomena of at least two types of current carriers—light holes from the main L-extremum and heavy holes from the additional L-extremum. Such features are qualitatively interpreted by a two-zone model.

However, it is not possible to describe the experimental data quantitatively in a two-zone model with a single set of additional extremum parameters. There is a significant variation in the parameters of the two-zone model, especially the parameters of the additional extremum (second zone). So we must admit

 https://www.doi.org/10.33910/2687-153X-2023-4-4-203-209

that the model of hard zones applied to doped PbTe does not work when trying to quantify the transfer phenomena. The strong sensitivity of the energy position of the additional extremum and the effective mass of holes to the calculated parameters of the model was also noted in (Volkov et al. 1983; 1984). Therefore, it can be assumed that the appearance of the second zone in the energy spectrum of p-PbTe may be due to the presence of crystal lattice defects, given their large number.

An admixture of thallium in lead telluride (PbTe) behaves in an unusual way. Thallium doping of lead telluride leads to a radical change in the electrophysical properties of PbTe. The following properties are manifested to the greatest extent: stabilization of the hole concentration (pinning of the Fermi level), a change in the type of temperature dependences of the Hall coefficients, a threshold decrease in the mobility of holes and the appearance of a superconducting transition with a critical temperature near 1 K (Shamshur et al. 2008). Moreover, the band of resonant states according to (Volkov et al. 1984) is located near the edge of the assumed extremum at the Σ-points of the Brillouin zone.

Pinning of the Fermi level and stabilization of the hole concentration (p) are due to the presence of partial filling of the density band of resonant states associated with thallium.

The threshold drop in mobility and the increase in the scattering cross section of holes on thallium impurities is explained by the resonant scattering of holes into the Tl band. The occurrence of superconductivity of PbTe samples is observed: Tl when the Fermi level degenerates into a band of resonant states (Kaidanov et al. 1982; Shamshur et al. 2008).

In this paper, in order to experimentally verify the currently used model concepts of the alloying effect of Na and Tl impurities, PbTe samples doped with Na and Tl simultaneously were made, kinetic coefficients were measured and a comparative analysis of the temperature dependences of kinetic coefficients with data for lead telluride samples doped with a single impurity was carried out. Information was obtained on the features of the energy spectrum of the PbTe valence band at Fermi energies greater than 0.15 eV.

Objects of research

The studies were carried out on polycrystalline PbTe samples manufactured using conventional metal-ceramic technology used in industry. They were annealed at a temperature of 650 °C for 120 hours. The synthesis of ingots was carried out from the initial chemical elements of semiconductor purity in evacuated quartz ampoules.

The choice of sample compositions was due to the following considerations. Na doping allows a wide range of changes in the concentration of holes in PbTe. However, in the quantitative analysis of data on transfer phenomena in PbTe:Na samples there is a large variation in the parameters of the two-band model, in particular, the effective mass of holes in the additional extremum. It should be noted that thallium doping does not allow to achieve such high concentrations of holes as in the case of using a sodium impurity. However, there is a stabilization of the concentration of holes in relation to the introduction of excess components and additional dopant Na. In this case, the Fermi level moves within the additional peak of the density function of states (associated with thallium doping) and exits it at high concentrations of additional acceptor impurity (Na).

Thus, the double doping of PbTe with thallium and sodium makes it possible to study the spectrum of electronic states in the valence band.

Since the solubility of impurities in PbTe reaches 1–2 at.%, we introduced a small amount of Tl, sufficient to stabilize the Fermi level, and varied the Na impurity content within wide limits in order to shift the Fermi level deep into the valence band.

Experiment

Measurements of kinetic coefficients were carried out by the probe method on direct current using copper-constantane thermocouples in the temperature range of 77–450 K in a constant magnetic field of 1.6 T.

The temperature dependences of the main kinetic coefficients—specific electrical conductivity (σ) and Hall (R) were investigated. On a series of PbTe:(Tl, Na) polycrystals with a fixed thallium (N_{Tl}) content of 0.3, 0.5 and 2 at.%. The sodium content varied from 0 to 2.5 at.%.

Results and discussions

The Hall coefficient in p-PbTe samples obtained by deviation from the stoichiometric composition towards an excess of tellurium or the introduction of an impurity of Na monotonically increases with increasing temperature. However, from helium temperatures (4.2 K) to about 150 K, the Hall coefficient retains a constant value. Therefore, the concentration of holes p in lead chalcogenides is determined from the value of the Hall coefficient at a temperature of 77 K by the formula:

$$P = \left(eR\right)^{-1}$$

Then, with a further increase in temperature, the Hall coefficient gradually increases and reaches a maximum in highly doped samples at approximately 430 K (Ravich et al. 1968). The position of the maximum is almost independent of the concentration of holes. A decrease in the Hall coefficient is observed long before the onset of intrinsic conductivity and cannot be explained by the latter. The observed behavior of the Hall coefficient is traditionally associated in semiconductor physics and in PbTe with the complex structure of the valence band and explained in the framework of a two-band model (Ravich et al. 1968).

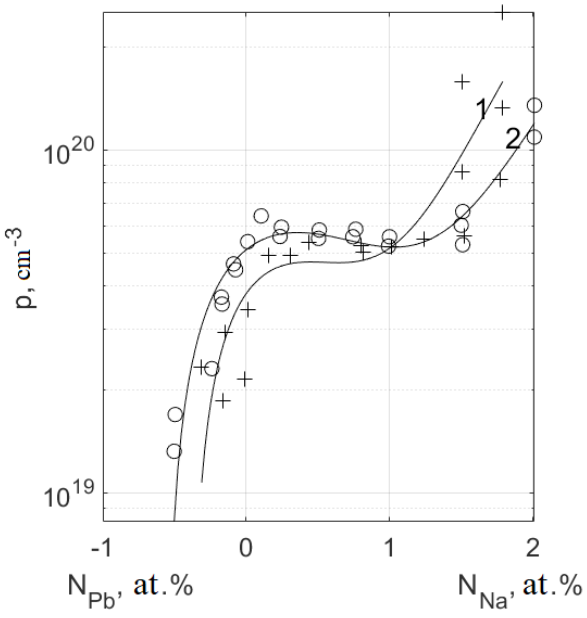

Fig. 2. Dependence of the hole concentration on the amount of additional impurities introduced into PbTe:Tl

Consider the experimental data we have obtained, shown in Figs. 2–4. As can be seen from Fig. 2, in a series of images with relatively small (0.3 and 0.5 at.%) with thallium content, there is indeed a fairly wide area of stabilization of the concentration of holes. When an additional dopant—excess Pb (donor)—is added to the charge of PbTe:Tl samples, the concentration of holes in the valence band decreases. The Fermi level shifts to the ceiling of the valence band. When Na acceptor impurity in the amount of $N_{Na} \geq 2N_{Tl}$ is added to the charge, the hole concentration begins to grow and the Fermi level leaves the band of resonant states. This result correlates with the electrical conductivity data.

The temperature dependence of the specific electrical conductivity of the studied PbTe:(Tl, Na) samples has a metallic character, and is characterized by lower values compared to PbTe:Na crystals. Estimates show that the cross-section of the scattering of holes on Tl impurities is about an order of magnitude higher and has a threshold character depending on the concentration of holes. This is due to the strong resonant scattering of holes (Kaidanov, Nemov 1981; Shamshur et al. 2008) in the band of resonant states arising against the background of the resolved states of the PbTe valence band when doped with its admixture of thallium (Kaidanov, Nemov 1981). The dependences of the resistivity on the amount of additional impurities in all series of samples with a fixed thallium content are similar and have

 https://www.doi.org/10.33910/2687-153X-2023-4-4-203-209

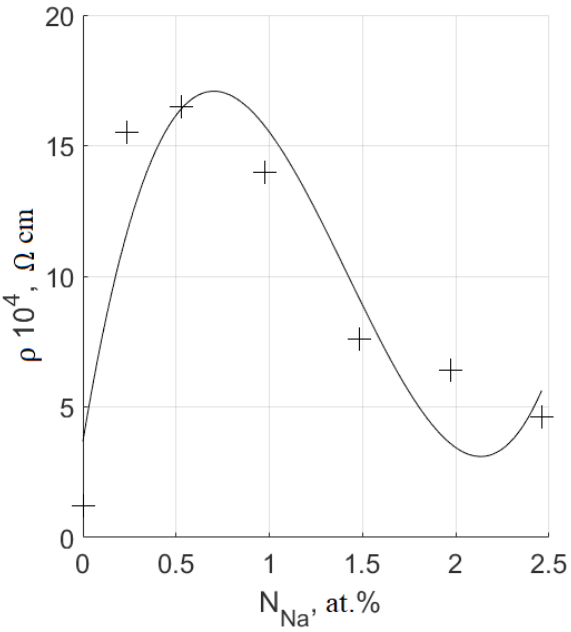

Fig. 3. Dependence of the specific electrical conductivity on the concentration of sodium impurity

the form of a curve with a maximum, which is consistent with the ideas of resonant scattering of holes into the thallium band. Fig. 3 shows data for a series of samples with 2 at.% thallium content, since a large amount of impurities compared to the concentration of intrinsic defects using the neutrality equation allows us to estimate the degree of filling of impurity states with electrons with holes (or electrons) according to the formula:

$$k = 0.5 + \frac{(N_{\mathrm{Na}} - p)}{2N_{\mathrm{Tl}}}.$$

The two in the formula takes into account the presence of two electronic states per thallium atom. It turns out that the maximum resistance corresponds to approximately half the filling of the resonance state band, and the initial points correspond to crystals doped with a single admixture of thallium grown by the Bridgman-Stockbarger method. They have a value of $k \approx 0.3$, that is, in samples with a high thallium content of 1–2 at.%, the thallium strip is about 2/3 filled with electrons and 1/3 with holes. For large N_{Na}, the coefficient $k \approx 0$, which is consistent with the concepts of resonant scattering and the passage of the peak of resonant states by the Fermi level.

Consider the Hall effect data. As can be seen from Fig. 4, in PbTe:(Tl, Na) samples, the character of the temperature dependence of the Hall coefficient radically changes. From the Hall coefficient $R(T)$ growing with temperature to PbTe:Na it changes the sign of the $\mathrm{d}R/\mathrm{d}T$ derivative in the low temperature region and becomes decreasing over the entire temperature range (up to 450 K).

Moreover, what is significant, even in samples with a significantly higher (almost an order of magnitude) content of additional impurity Na (up to 2 at.%) than Tl (0.3 at.%), the temperature dependences of the coefficient $R(T)$ do not match the dependences characteristic of PbTe:Na samples with the same hole concentration and Fermi level. This means that PbTe:(Na) and PbTe:(Tl, Na) samples in the region of high Fermi energies at the same concentrations of holes have different values of the density function of states, i. e. crystals with the same crystal lattice, but with different impurities have a different energy spectrum. This conclusion is supported by the significant variation in the band parameters of the second zone of sodium-doped PbTe crystals noted in the literature.

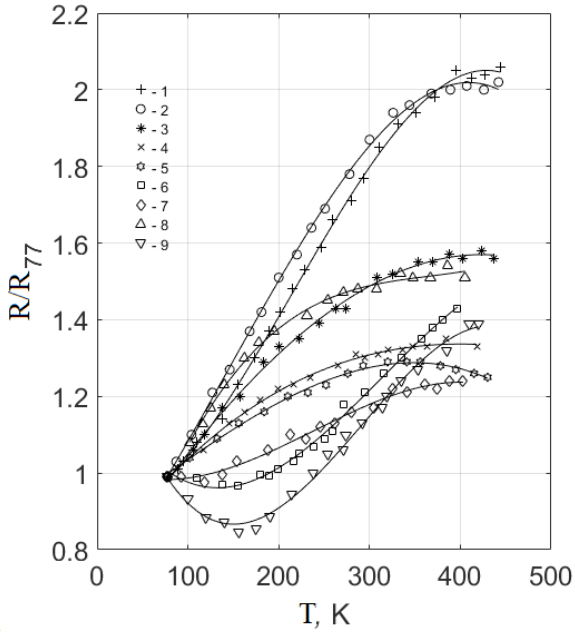

Fig. 4. Temperature dependence of the Hall coefficient in PbTe:(Tl, Na) samples

It should be noted that the presence of a peak in the density of states associated with Tl against the background of the resolved states of the valence band in PbTe:(Tl, Na) is confirmed by superconductivity data. An estimate of the density of states per spin can be made using the formulas:

$$N(0) = 4.8*10^{14}\,\frac{H_{c_2}(0)}{\rho_N T_c},$$

$$N(0) = 2.8*10^{14}\,\rho_N^{-1}\left|\frac{\partial H_{c_2}(T)}{\partial T}\right|_{T\to T_c},$$

where H_{c_2} is the second critical magnetic field, ρ_N is the resistivity of the sample in the normal state, $H_{c_2}(0)$ is an extrapolation of the dependence of $H_{c_2}(T)$ to T = 0 K. The estimates made in this way showed that the density of states in the valence band of PbTe doped with Tl and Na exceeds its value in samples of PbTe doped with Na in samples with such a concentration of holes. In this regard, the authors (Kaidanov et al. 1982) suggested that superconducting electrons are in hybridized band-impurity states.

Thus, based on the results obtained in the work and the available literature data, it must be admitted that the hard zone model does not work in PbTe doped samples with sodium and thallium. The energy spectrum of holes depends on the grade and amount of impurities. Moreover, in the one-electron approximation, it is not possible to combine the appearance of a peak of resonant states in thallium-doped PbTe with two energy compounds per thallium atom. Within the framework of the classical theory of BCS, there is no explanation for the occurrence of a superconducting transition in PbTe:Tl with a high critical temperature for semiconductors $T_c \approx 1$ K.

Conclusions

Thus, the experimental data obtained in the work on transfer phenomena in conjunction with the literature indicate that the ideas of an ideal crystal in the one-electron approximation and the band theory are insufficient to describe the electrophysical properties of PbTe and other compounds of group IV–VI.

 https://www.doi.org/10.33910/2687-153X-2023-4-4-203-209

This is understandable, since they are synthesized with a noticeable deviation from the stoichiometric composition with a large number of intrinsically electrically active defects (about 0.1–1 at.%) In addition, the materials used in thermoelectricity contain alloying impurities in an amount exceeding the concentration of intrinsic defects, distributed statistically. In such cases, using the example of III–V semiconductors, A. Yu. Zakharov showed (Zakharov 2015) that it is necessary to take into account the approximation of solid solutions and the approach with renormalization of the electron energy spectrum.

It should be noted that this problem is common for compounds $A^{IV}B^{VI}$ and $A^{V}_{2}B^{VI}_{3}$.

Conflict of Interest

The authors declare that there is no conflict of interest, either existing or potential.

Author Contributions

All the authors discussed the final work and took part in writing the article.

References

Abrikosov, N. Kh., Shelimova, L. E. (1975) *Poluprovodnikovye materialy na osnove soedinenii $A^{IV}B^{VI}$ [Semiconductor materials based on compounds $A^{IV}B^{VI}$]*. Moscow: Nauka Publ., 195 p. (In Russian)

Gol'tsman, B. M., Kudinov, V. A., Smirnov, I. A. (1972) *Poluprovodnikovye termoehlektricheskie materialy na osnove Bi_2Te_3 [Semiconductor thermoelectric materials based on Bi_2Te_3]*. Moscow: Nauka Publ., 320 p. (In Russian)

Kaidanov, V. I., Nemov, S. A. (1981) Vliyanie primesej talliya na rasseyanie dyrok v telluride svintsa [Effect of thallium impurities on hole scattering in lead telluride]. *Fizika i tekhnika poluprovodnikov — Semiconductors*, 15 (3), 542–550. (In Russian)

Kaidanov, V. I., Nemov, S. A., Parfen'ev, R. V., Shamshur, D. V. (1982) Vliyanie dopolnitel'nogo legirovaniya aktseptornoj primes'yu na sverkhprovodyashchij perekhod v PbTe<Tl> [The effect of additional doping with an acceptor impurity on the superconducting transition in PbTe<Tl>]. *Pis'ma v ZhEHTF — JETP Letters*, 35, 517–519. (In Russian)

Nemov, S. A., Osipov, P. A., Proshin, V. I. et al. (2000) Sverkhprovodimost' splavov $Sn_{0.62}Pb_{0.33}Ge_{0.05}Te$, legirovannykh In [Superconductivity of In-doped $Sn_{0.62}Pb_{0.33}Ge_{0.05}Te$ alloys]. *Fizika tverdogo tela — Physics of the Solid State*, 42 (7), 1180–1182. (In Russian)

Nemov, S. A., Ravich, Yu. I. (1998) Primes' talliya v khal'kogenidakh svintsa: metody issledovaniya i osobennosti [Thallium dopant in lead chalcogenides: Investigation methods and peculiarities]. *Physics–Uspekhi — Advances in Physical Sciences*, 168 (8), 817–842. https://doi.org/10.1070/pu1998v041n08abeh000427 (In Russian)

Ravich, Yu. I., Efimova, B. A., Smirnov, I. A. (1968) *Metody issledovaniya poluprovodnikov v primenenii k khal'kogenidam svintsa PbTe, PbSe i PbS [Methods of semiconductor research applied to lead chalcogenides PbTe, PbSe and PbS]*. Moscow: Nauka Publ., 383 p. (In Russian)

Shamshur, D. V., Nemov, S. A., Parfen'ev, R. V. et al. (2008) Nizkotemperaturnaya provodimost' i effekt Kholla v poluprovodnikovykh tverdykh rastvorakh $(Pb_zSn_{1-z})_{0.84}In_{0.16}Te$ [Low–temperature conductivity and Hall effect in Semiconductor Solid solutions $(Pb_zSn_{1-z})_{0.84}In_{0.16}Te$]. *Fizika tverdogo tela — Physics of the Solid State*, 50 (11), 1948–1952. (In Russian)

Volkov, B. A., Pankratov, O. A., Sazonov, A. V. (1983) Teoriya elektronnogo energeticheskogo spektra poluprovodnikov $A^{IV}B^{VI}$ [Theory of the electronic energy spectrum of semiconductors $A^{IV}B^{VI}$]. *Zhurnal eksperimental'noj i teoreticheskoj fiziki — Journal of Experimental and Theoretical Physics*, 85 (4), 1395–1408. (In Russian)

Volkov, B. A., Pankratov, O. A., Sazonov, A. V. (1984) Zonnaya struktura tverdykh rastvorov na osnove soedinenij $A^{IV}B^{VI}$ [Band structure of solid solutions based on compounds $A^{IV}B^{VI}$]. *Fizika tverdogo tela — Physics of the Solid State*, 26 (2), 430–435. (In Russian)

Zakharov, A. Yu. (2015) Teoriya elektronnoj struktury poluprovodnikovykh tverdykh rastvorov zameshcheniya. Analiticheskie podkhody. Obzor [Theory of the electronic structure of semiconductor solid substitution solutions. Analytical approaches. Review]. *Fizika i tekhnika poluprovodnikov — Semiconductors*, 49 (7), 865–886. (In Russian)

Summaries in Russian / Информация о статьях на русском языке

Физика конденсированного состояния

СРАВНЕНИЕ ПОТЕНЦИАЛОВ МЕЖАТОМНОГО ВЗАИМОДЕЙСТВИЯ ПРИ МОДЕЛИРОВАНИИ УПРУГИХ ХАРАКТЕРИСТИК ПСЕВДО-ГРАФЕНОВЫХ КРИСТАЛЛОВ

Рожков Михаил Александрович, Абраменко Никита Дмитриевич, Смирнов Андрей Михайлович, Колесникова Анна Львовна, Романов Алексей Евгеньевич

Аннотация. В настоящей работе проведено моделирование механических характеристик псевдо-графеновых кристаллов G5-7v1, G5-6-7v2, G4-8v1, G5-6-8v2, G5-6-8v4, G5-8v1, которые включают в себя плотные сетки разнознаковых клиновых дисклинаций. Для исследования рассматриваемых кристаллов использовался метод молекулярной динамики. Было представлено сравнение значений упругих характеристик графена и псевдо-графена, полученных с помощью потенциалов межатомного взаимодействия AIREBO, Tersoff и LCBOP. Продемонстрирована ограниченность применения данных потенциалов при моделировании псевдо-графеновых кристаллов. В результате работы сделан вывод о необходимости модернизации существующих потенциалов межатомного взаимодействия для углеродных аллотропов или создания нового.

Ключевые слова: молекулярная динамика, псевдографен, упругие свойства, дисклинация, дефектная структура

Для цитирования: Rozhkov, M. A., Abramenko, N. D., Smirnov, A. M., Kolesnikova, A. L., Romanov, A. E. (2023) A comparison of interatomic interaction potentials in modeling elastic properties of pseudo-graphene crystals. *Physics of Complex Systems*, 4 (4), 149–156. https://www.doi.org/10.33910/2687-153X-2023-4-4-149-156 EDN HRTBPL

ВЛИЯНИЕ ТЕМПЕРАТУРНЫХ РЕЖИМОВ НА ТЕРМОСТИМУЛИРОВАННУЮ ДЕПОЛЯРИЗАЦИЮ ПЛЕНОК ПОЛИВИНИЛИДЕНФТОРИДА

Волгина Елена Алексеевна, Меркулова Мария Эдуардовна, Темнов Дмитрий Эдуардович

Аннотация. В работе исследовалось влияние температуры поляризации в поле коронного разряда и режимов предварительного отжига пленок сополимера поливинилиденфторида с тетрафторэтиленом на токи термостимулированной деполяризации. Для различных температур поляризации образцов определены параметры электрически активных дефектов, ответственных за релаксационные процессы, величина высвобождаемого в процессе деполяризации заряда (Q) и значение пьезоэлектрического модуля d_{33}. Выявлены наилучшие температурные режимы создания пьезоэлектрического состояния в данном материале.

Ключевые слова: поливинилиденфторид, термоактивационная спектроскопия, термостимулированная деполяризация, коронный разряд, электрически активные дефекты

Для цитирования**:** Volgina, E. A., Merkulova, M. E., Temnov, D. E. (2023) Influence of temperature conditions on thermostimulated depolarization of polyvinylidene fluoride films. *Physics of Complex Systems*, 4 (4), 157–160. https://www.doi.org/10.33910/2687-153X-2023-4-4-157-160 EDN BQEZSV

СЛОЖНАЯ НЕЭКСПОНЕНЦИАЛЬНАЯ ФОРМА ЗАТУХАЮЩИХ КОЛЕБАНИЙ В ОДНООСНООРИЕНТИРОВАННЫХ ПОЛИМЕРНЫХ МАТЕРИАЛАХ С ОДНОЙ МЕХАНИЧЕСКОЙ СТЕПЕНЬЮ СВОБОДЫ

Вавилов Дмитрий Сергеевич, Прищепёнок Ольга Борисовна, Рымкевич Павел Павлович

Аннотация. В работе исследованы релаксационные свойства одноосно-ориентированных полимерных нитей. В данной статье анализируется колебательная релаксация в механической системе с одной степенью свободы. Система представляет собой тяжелый груз, висящий на легкой нити, выполненной из высокоориентированного полимерного материала.

Авторами экспериментально подтвержден факт существования биений для ряда полимерных материалов (поликапромид, СВМ, терлон, армос и др.) при определенном статическом уровне нагрузки ниже температуры стеклования. Дано физическое объяснение факта существования второй моды колебаний.

С одной стороны, в системе происходят упругие колебания, с другой стороны, согласно

барьерной модели, происходят колебания чисел заполнения энергетических уровней. Другими словами, возникает ещё одна мода колебаний, связанная с высокоэластичной деформацией, поскольку высокоэластичная деформация определяется числами заполнения соответствующих состояний. При близких частотах и наблюдается эффект биений.

Ключевые слова: одноосно-ориентированные полимерные материалы, продольные малоамплитудные колебания, высокоэластичная деформация, определяющее уравнение, биения

Для цитирования: Vavilov, D. S., Prishchepenok, O. B., Rymkevich, P. P. (2023) Complex non-exponential form of damped vibrations in uniaxially oriented polymeric materials with one mechanical degree of freedom. *Physics of Complex Systems*, 4 (4), 161–175. https://www.doi.org/10.33910/2687-153X-2023-4-4-161-175 EDN MYYBEC

Теоретическая физика

РАСЧЕТ ПОКАЗАТЕЛЕЙ ЛЯПУНОВА И ХАРАКТЕРИСТИКИ НЕЛИНЕЙНОЙ ДИНАМИКИ В ОБЪЕМНЫХ АНТИФЕРРОЭЛЕКТРИКАХ

Лим Сью-Чу

Аннотация. В работе исследуется влияние амплитуды, частоты и затухания приложенного поля на максимальные показатели Ляпунова и хаотическую динамику в объемных антиферроэлектрических (АФЭ) системах. Численное моделирование проводится в трех частях. В первой части, по алгоритму Вольфа вычисляются показатели Ляпунова при изменяющейся частоте и постоянной амплитуде. Во второй части амплитуда варьируется при сохранении постоянной частоты. Для малых (g = 0,01) и больших (g = 0,3) значений затухания рассчитываются два набора данных. В третьей части, с помощью ряда отобранных параметров на основе положительных и отрицательных показателей Ляпунова и с использованием метода Рунге-Кутты четвертого порядка строятся фазовые портреты. Результаты показывают, что показатели Ляпунова применимы для определения хаотических и периодических режимов при малом затухании, тогда как при большом затухании картина менее очевидна. В исследовании также показано, что изменение параметров приложенного поля позволяет контролировать хаотические и периодические отклики в объемной системе АФЭ.

Ключевые слова: показатель Ляпунова, антиферроэлектрик, дигидрогенфосфат аммония, хаос, нелинейность, периодический отклик

Для цитирования: Lim, S.-Ch. (2023) Calculations of Lyapunov exponents and characterizations of nonlinear dynamics in bulk antiferroelectrics. *Physics of Complex Systems*, 4 (4), 176–194. https://www.doi.org/10.33910/2687-153X-2023-4-4-176-194 EDN ZLXASG

Физика полупроводников

ОСОБЕННОСТИ СТРУКТУРЫ И ОПТИЧЕСКИХ СВОЙСТВ АМОРФНЫХ ПОЛУПРОВОДНИКОВЫХ ПЛАЗМОННЫХ НАНОКОМПОЗИТОВ TiO_2<Ag>, ПОЛУЧЕННЫХ МЕТОДОМ ИОННО-ПЛАЗМЕННОГО СО-РАСПЫЛЕНИЯ

Дауитхан Куанышбек, Приходько Олег Юрьевич, Пешая Светлана Леонидовна, Мухаметкаримов Ержан, Козюхин Сергей Александрович, Максимова Суюмбика Якубовна, Исмайлова Гузаль Амитовна

Аннотация. Исследованы структура и оптические свойства аморфных полупроводниковых нанокомпозитных пленок TiO_2<Ag>, полученных ионно-плазменным ВЧ-магнетронным совместным распылением мишени из TiO_2 и Ag только в атмосфере аргона. Матрица пленок TiO_2<Ag> аморфная с включениями изолированных наночастиц серебра размером 3–4 нм. Спектры оптического пропускания имеют резкий край основной полосы поглощения в области ~ 300 нм, образованный прямыми и непрямыми разрешенными оптическими переходами. Ширина запрещенной зоны пленок TiO_2<Ag> увеличивается с увеличением концентрации Ag из-за некоторого упорядочения матрицы. Полоса поглощения наблюдается в видимой области спектра из-за эффекта локального поверхностно-плазмонного резонансного поглощения (ЛППР) на наночастицах серебра. Интенсивность ЛППР увеличивается с концентрацией серебра, а максимум полосы поглощения в зависимости от концентрации Ag находится в области от 455 до 488 нм.

Ключевые слова: ионно-плазменное распыление, аморфные плазмонные полупроводниковые нанокомпозиты TiO_2<Ag>, наночастицы серебра, структура, оптические свойства, поверхностное плазмонное резонансное поглощение

Для цитирования**:** Dauithan, K., Prikhodko, O. Yu., Peshaya, S. L., Mukhametkarimov, Y. S., Kozyukhin, S. A., Maksimova, S. Ya., Ismaylova, G. A. (2023) Peculiarities of the structure and optical properties of amorphous semiconductor plasmon nanocomposites TiO_2<Ag>, prepared by ion plasma co-sputtering. *Physics of Complex Systems*, 4 (4), 195–202. https://www.doi.org/10.33910/2687-153X-2023-4-4-195-202 EDN RRDAEF

ЭНЕРГЕТИЧЕСКИЙ СПЕКТР ДЫРОК В СИЛЬНОЛЕГИРОВАННОМ PbTe

Немов Сергей Александрович, Дашевский Зиновий, Проклова Виктория Юрьевна, Михайлов Никита Александрович

Аннотация. Исследованы электрофизические свойства серии образцов PbTe, легированных Tl и дополнительной примесью Na. Наблюдаемые особенности температурных зависимостей электропроводности и коэффициента Холла объясняются в рамках модели резонансных состояний таллия с учетом сложного строения валентной зоны. Показано, что представления об идеальном кристалле и зонной структуре в рамках одноэлектронного приближения недостаточно для объяснения экспериментальных данных по эффекту Холла. Необходимо учитывать модификацию энергетического спектра с учетом статистического распределения примесей и дефектов и дополнительного взаимодействия частиц.

Ключевые слова: PbTe, энергетический спектр дырок, примеси Tl и Na, стабилизация уровня Ферми, модификация зонного спектра

Для цитирования: Nemov, S. A., Dashevsky, Z. M., Proklova, V. Yu., Mikhailov, N. A. (2023) Energy spectrum of holes in highly alloyed PbTe. *Physics of Complex Systems*, 4 (4), 203–209. https://www.doi.org/10.33910/2687-153X-2023-4-4-203-209 EDN WRDYMW